

2013

Numerical investigations of Holstein phonons on the periodic Anderson model

Peng Zhang

Louisiana State University and Agricultural and Mechanical College, zpantz@gmail.com

Follow this and additional works at: https://digitalcommons.lsu.edu/gradschool_dissertations



Part of the [Physical Sciences and Mathematics Commons](#)

Recommended Citation

Zhang, Peng, "Numerical investigations of Holstein phonons on the periodic Anderson model" (2013). *LSU Doctoral Dissertations*. 2270.

https://digitalcommons.lsu.edu/gradschool_dissertations/2270

This Dissertation is brought to you for free and open access by the Graduate School at LSU Digital Commons. It has been accepted for inclusion in LSU Doctoral Dissertations by an authorized graduate school editor of LSU Digital Commons. For more information, please contact gradetd@lsu.edu.

NUMERICAL INVESTIGATIONS OF HOLSTEIN PHONONS ON THE PERIODIC ANDERSON MODEL

A Dissertation

Submitted to the Graduate Faculty of the
Louisiana State University and
Agricultural and Mechanical College
in partial fulfillment of the
requirements for the degree of
Doctor of Philosophy

in

The Department of Physics and Astronomy

by

Peng Zhang

B.S., Zhejiang University, 2002

M.S., Zhejiang University, 2006

M.S., University of Cincinnati, 2008

Acknowledgments

Firstly, I would like to thank my advisor, Mark Jarrell, for his important and priceless support in my Ph.D research. His energetic spirit and devoteness in work and Physics really surprised me and become an idol in my research life. Then I would like to thank my co-advisor Juana Moreno. Anytime when I come to any problem, either in academic or life, she never hesitate in providing me the help. I would also like to thank Fakher Assaad in hosting my one year visit at Wuerzburg, Germany. The one year visiting at Wuerzburg helps me fully understand the idea of continuous time quantum monte carlo method and my research about the effect of phonons in PAM is accomplished during this visit. I would like to thank Pete Reis and Ka-Ming Tam, who are the co-authors of my research work on the Ce volume collapse problem. This work will not be finished without their creative ideas. I would like to give a big appreciation to Andy McMahan, who lead our attention to the experiments about the role of phonons in the Ce volume collapse. He is not only such an expert in the Ce volume collapse problem but also a very nice person, willing to answer all our question, in which some might be naive. I would like to thank Shuxiang Yang for all the important and valuable discussion with him. I would like to thank other members in our group, including Kuang Shing Chen, Chinedu Ekuma, Hanna Terletska, Valéry Rousseau, Kalani Hettiarachchilage and all others, for their important help in my research life. I also would like to thank our secretary Carol Duran, for her great support in my work. Finally I would like to thank my wife, Ying, for her constant trust, encourage and valuable advice ever since we know each other. Thanks all of you for your help.

Table of Contents

Acknowledgments	ii
Abstract	v
Introduction	1
1 Anderson impurity and the periodic Anderson model	3
1.1 Kondo effect and Kondo problem	3
1.2 Anderson impurity model and the local moment	4
1.3 Schrieffer–Wolff transformation	6
1.4 Periodic Anderson model	7
1.5 Heavy fermions	9
1.6 Introduction of my works	12
2 The numerical algorithm	14
2.1 Model Hamiltonian	14
2.2 DMFT	15
2.3 CTQMC	16
3 The Ce volume collapse	19
3.1 Experimental background	19
3.1.1 Phase diagram of Ce	19
3.1.2 Experiments	19
3.2 Theories	22
3.2.1 Scenarios proposed for Ce volume collapse	22
3.3 Phonon crisis	23
3.4 Numerical methods	24
3.5 Results	26
3.5.1 Effect of electron-phonon on c-band	26
3.5.2 Phase diagram	34
3.6 Conclusion and future directions	35
Bibliography	37
A Weak coupling expansion CTQMC	44
A.1 Partition function	44
A.2 Detailed balance	45
A.3 Determinant ratios and fast update	46
A.3.1 the update in Markov chain between the k^{th} order and the $(k + 1)^{th}$ order	46

A.3.2	the update between the k^{th} order and the $(k + 2)^{th}$ order	49
A.4	Observables	51
A.4.1	Average order	51
A.4.2	Single particle Green's function	51
A.4.3	Two-particle Green's function	52
A.5	Auxiliary fields	53
A.5.1	Minus sign and the auxiliary fields for Hubbard interaction	53
A.5.2	Update by flipping the auxiliary fields	53
A.6	Retard interaction	56
A.6.1	Electron-phonon interaction	56
A.6.2	Phonon vertex update algorithm	57
A.6.3	Choice of auxiliary fields for electron-phonon interaction	58
B	Green's function	59
B.1	One-particle Green's function	59
B.2	Two-particle Green's function	60
B.2.1	Definition	60
B.2.2	Charge, spin, and pair susceptibilities	61
B.2.3	Bethe-Salpter equation and bulk susceptibility	63
C	Numerical tricks	65
C.1	Fourier transform	65
C.2	Inverse Fourier transform	66
C.3	High frequency tails of self-energy	66
C.4	Inhomogeneous frequency grid	67
D	Minus sign problem	68
E	Analytic continuation	70
E.1	Maximum Entropy Method	70
E.1.1	Bayesian statistics	71
E.1.2	Prior Probability	71
E.1.3	Likelihood function	72
E.1.4	Choices of α	74
E.1.5	Annealing Method	75
E.1.6	Analytic continuation of $G(i\omega_n)$ and $\Sigma(i\omega_n)$	75
E.2	Stochastic Analytic Continuation	76
F	Publication List	78
Vita	79

Abstract

In condensed matter physics, the idea of localized magnetic moments and the scattering of conduction electrons by those local moments are of central importance not only for explaining the transport of electrons at low temperature region but also for developing the related models and theories to extend our understanding of novel physics like non-conventional superconductor, quantum phase transition and non-Fermi liquid behavior. In the first chapter of this work, I will look back at the discovery of Kondo scattering, the introduction of Anderson impurity scenario, the extension to lattice version of the Anderson impurities, the periodic Anderson model, and how these ideas are used to the heavy fermion materials.

In order to attack those problems and models numerically, in the second chapter, I will discuss the algorithm of dynamical mean-field theory, where interaction expansion continuous time quantum Monte Carlo is used as impurity solver. The introduction of dynamical mean-field theory and its related methods are one of the largest victory of computational condensed matter physics in the past three decades. By mapping the lattice problem to an impurity problem and solving it self-consistently, we can get the static and dynamic outputs in the thermal dynamical limit from dynamical mean-field theory simulation by solving a single site problem. In the infinite coordinate number limit, the dynamical mean-field theory results converge to the exact results. Quantum Monte Carlo is widely used in computational physics. Compared with the conventional quantum Monte Carlo, the recently introduced interaction expansion continuous time quantum Monte Carlo is free of decomposition error in imaginary time.

In the third chapter, the pressure induced volume collapse problem of Cerium is explored. It has been discovered that Cerium will experience a 15% volume collapse from a large volume γ phase to a small volume α phase as the external pressure is above a certain critical value. Such $fcc \rightarrow fcc$ iso-structure first-order phase transition has long been thought to be driven by purely electronic factors but there are recent experimental evidences indicating that lattice oscillation contribute a tremendous part (20%~50%) of the entropy change in such first-order phase transition. Using the periodic Anderson model with Holstein phonons on the conduction band, we found that only above a critical value of electron-phonon coupling such a model will experience a first-order phase transition. As the external pressure is increased, consequently the hybridization between conduction and localized electrons is increased as well, and the system will be driven from a local moment+bipolaron phase to a Kondo singlet+polaron phase. In the pressure-temperature plain, the first-order phase transition line which separates the local moment+bipolaron phase and the Kondo singlet+polaron phase terminates at a second order critical point. We hope our discovery may shed light on exploring the role of phonon degree of freedom in the long lasting Cerium volume collapse problem.

In the appendix, the numerical details of the interaction expansion continuous time quantum Monte Carlo method are covered. The measurement of singlet particle and two particle Green's function, the numerical tricks in accomplishing better Fourier transformation results

and the analytic continuation of quantum Monte Carlo data are introduced briefly in the appendix as well. We recommend reading the related references for more details.

Introduction

When the Anderson impurity model is introduced, the original purpose is to explain the scattering of valence electrons in metals by the impurity magnetic ions inside. The valence electrons can hop to the orbitals of ions and vice versa, which is called the hybridization. At large hybridization the valence electrons and localized electrons of ions will form singlet bonds, which are called Kondo singlets. Due to this process, the localized electrons are screened by the valence electrons and the effective mass of valence electrons is renormalized to a large value. Later on, the Anderson impurity model and its lattice extension have become a standard model in the research of condensed matter physics. Their implementation was not limited to the impurity problem or disorder problem, but also to materials without impurities, such as the so-called heavy fermions.

In heavy fermion materials, the $4f$ or $5f$ electrons are localized under the Fermi surface, while the valence electrons on the s , p or sometimes the d orbitals are free to be mobile. From the tight-binding point of view, the heavy fermion materials form a periodic Anderson model, where the electrons on s , p and d orbitals are treated as conduction electrons and electrons on the f orbital are treated as localized electrons. At weak hybridization, the model can be described by the Fermi-liquid theory, and the properties are closer to the free electrons. But at strong hybridization, the screening between localized f -electrons and the conduction electrons will enhance the mass of the latter by more than 100 times. As a consequence, the specific heat, the conductivity and the magnetic susceptibility of heavy fermion materials will be changed drastically. Because of the hybridization, f -electrons of neighboring sites can interact with each other, which may lead to the long range magnetic ordering. Then the model will experience a phase transition from a paramagnetic state to a magnetically ordered state (ferromagnetic state or anti-ferromagnetic state) and the Fermi-liquid theory will totally fail.

In the tight binding model, the effect of lattice oscillation on electrons is always an interesting problem. For the periodic Anderson model, the coupling between phonon and the conduction electrons will produce a retarded attractive interaction among the conduction electrons. Such an attractive interaction will compete with the bonding effect between the conduction and localized electrons. When the phonon mediated attractive interaction is large enough, the Kondo singlet will be destroyed and lead to a so-called Kondo collapse.

A typical example of heavy fermions is the rare earth materials. Because of the existence of their $4f$ and $5f$ electrons, rare earth materials have a lot of exotic properties. One of the most interesting might be the volume collapse transition as the external pressure is changed. Take cerium as an example which has one $4f$ electron. At room temperature it will experience a rather large volume decrease from a large volume phase γ to a small volume phase α . For a very long time it has been claimed that this kind of first-order phase transition is purely the consequence of electronic effect and one widely accepted theory is the Kondo volume collapse scenario. In the Kondo volume collapse scenario, it is argued that at large volume size, the system is in a non-screening state. As the external pressure is increased, the hybridization

between c and f orbitals increases as well since the distance between neighboring ions is decreased. When such hybridization is large enough, the Kondo singlet formation between c and f electrons will push the system to the Kondo screening state, which is the α phase of Ce. This Kondo volume collapse scenario is pretty successful in explaining many experimental facts like in *Ce* volume collapse the change of magnetic susceptibility, the change of specific heat and entropy. But a series of experiments from 2004 points out that phonons contribute a big portion in the entropy change of such first-order phase transition. As a response to these new experiment discoveries, we have tried to include the lattice oscillation degree of freedom into the periodic Anderson model by numerical efforts. Our numerical calculation shows that electron-phonon coupling is of critical importance to have a non-screening to Kondo screening first-order transition in the periodic Anderson model. This result supports the experimental conclusion that phonons are important in explaining the *Ce* volume collapse.

In the research of condensed matter physics and beyond, numerical simulation has become a tool as important as theoretical and experimental efforts. Quantum Monte Carlo (QMC) is one of such numerical tools being widely used. Unfortunately the success of QMC is often limited by the computer power available. In the QMC simulation, the numerical cost often scales exponentially with the system size being simulated. Clearly it is impossible to simulate a model with Avogadro's number of atoms as the real materials. Actually, in QMC simulation, the largest system size usually is order of ten at the room temperature energy scale. The introduction of Dynamical Mean Field Theory (DMFT) at least partly solved this problem. In the DMFT, the correlations of all other lattice sites on one site are treated as a mean-field bath. By omitting all the spatial correlations from other sites and preserving the dynamical correlations exactly, the hybridization between the bath and the one site is solved iteratively. So the lattice problem is mapped to an effective Anderson impurity problem and the solution of this impurity site can be treated as the solution of the lattice problem in the thermal dynamical limit. In our work, QMC is used as the impurity solver of DMFT.

This work is organized as following: in the first chapter, we will review the Kondo problem, the origin of Anderson localization and the related Anderson model; in the second chapter, the numerical tools to be used in the simulation will be introduced; in the third chapter, the effect of phonons on the conduction band of the periodic Anderson model will be discussed. The cerium volume collapse problem and how this first-order transition may be related to the PAM+Holstein phonon model are covered in this chapter as well.

Chapter 1

Anderson impurity and the periodic Anderson model

1.1 Kondo effect and Kondo problem

It has long been found that the resistivity of metals has the form $\rho(T) = \rho_0 + aT^2 + bT^5 + c \ln \frac{\mu}{T}$. The first term ρ_0 was known being the residual resistivity due to the scattering of conduction electrons by the non-magnetic defects or impurities; the aT^2 term comes from the excitation near the Fermi surface; and the bT^5 term is related with the scattering of conduction electrons by the lattice vibration. It can be easily seen that the first three terms are dominating at high temperature and will lead to a monotonic increment of resistivity when the temperature is increased. But in the low temperature region, the log term $c \ln \frac{\mu}{T}$ will incur a minimum at some relatively small but non-zero temperature, as shown in figure 1.1.

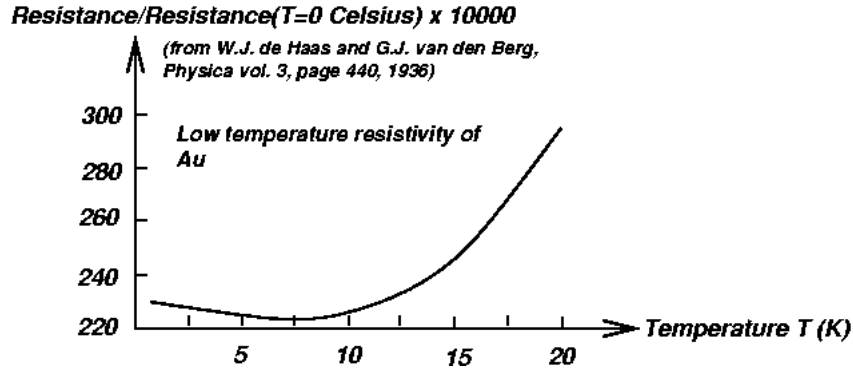


Figure 1.1: The resistivity of gold as a function of temperature at the low temperature region.

For nearly 30 years, there were confusions about the origin of this minimum in resistivity until in 1964 Jun Kondo [1] successfully pointed out the logarithm term is the consequence of the scattering process from the spin exchange between the conduction electrons and the magnetic impurity. Beyond the first order scattering, Kondo considered a second order scattering where the conduction electron with state k, σ exchanges spin with the impurity electron with spin $-\sigma$ and then exchange spins again back to its original spin state k', σ . Such scattering is called the Kondo effect. In figure 1.2, the Kondo scattering is presented in Feynman diagram. By integration of the virtual intermediate state one arrives at

$$\sum_{k''} J(k, \sigma; -\sigma \rightarrow k'' - \sigma; \sigma) \cdot J(k'', -\sigma; \sigma \rightarrow k' \sigma; -\sigma) \frac{1 - f_{k''}}{\epsilon_k - \epsilon_{k''}} =$$

$$J^2 \rho \log \left(\left| \frac{\epsilon_k - \epsilon_F}{\epsilon_k - D} \right| \right) \quad (1.1)$$

where ρ is the density of states, D is the band width, J is a constant, ϵ_k is the kinetic energy of electrons, ϵ_F is the Fermi energy and f_k is the Fermi function at ϵ_k . This gives the logarithm term when the approximation $\epsilon_k - \epsilon_F \approx k_B T$ is used.

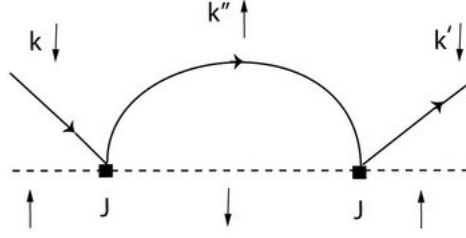


Figure 1.2: The spin exchange scattering process proposed by Kondo. A spin down conduction electron (represented by the thick line) is scattered by the spin up impurity (represented by the dotted line), where in the intermediate state their spins are exchanged.

It can be easily seen that when $T \rightarrow 0$, the logarithm term from Kondo's calculation will diverge. The consideration of even higher order scattering only makes the resistivity diverges faster. Such a clear contradiction with experiment is called the *Kondo problem*. Due to the Kondo screening effect, as $T < T_K$ the magnetic impurity forms a non-magnetic Kondo singlet with the spin of conduction electrons. This paramagnetic state is described by the Fermi liquid theory and contributes the $\sim aT^2$ term to the resistivity. The consequent non-magnetic impurity will contribute the non-temperature dependent term to the resistivity. The Kondo temperature is defined as

$$T_K \sim D e^{-\frac{1}{|J|\rho}} \quad (1.2)$$

which indicates the energy scale where the conduction and impurity electrons begin to form Kondo singlets. Fig. 1.3 is a cartoon of how such Kondo singlet is formed.

The Hamiltonian of Kondo impurity model is

$$H = \sum_{k,\sigma} \epsilon_k c_{k,\sigma}^\dagger c_{k,\sigma} + \frac{J}{N} \sum_{k,k'} c_{k,a}^\dagger \sigma_{ab} c_{k',b} \cdot S^f \quad (1.3)$$

where ϵ_k is the kinetic energy and J is the coupling constant between the spin of conduction electrons and the impurity local moment; $c_{k,a}^\dagger$ is the creation operator of an electron with moment k and spin component $a = \pm \frac{1}{2}$; S^f is the spin of magnetic impurity.

1.2 Anderson impurity model and the local moment

Another starting point about the effect of magnetic impurities in metal is the so called Anderson impurity model

High T, weak coupling Low T, strong coupling

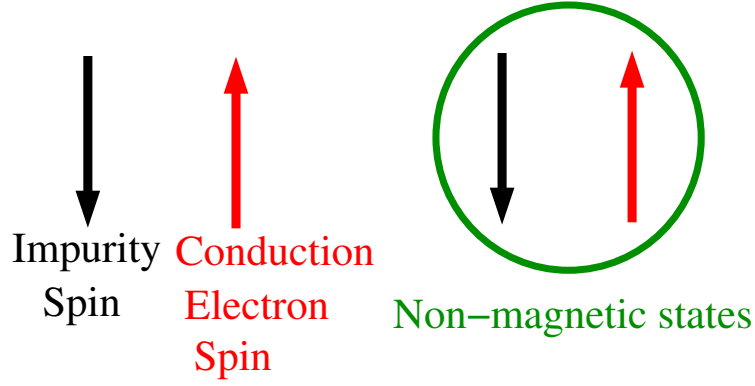


Figure 1.3: Cartoon of the Kondo singlet formation. At high temperature, the conduction electrons are moving at Fermi velocity v_F and the coupling between the conduction electron and the magnetic impurity is weak. But at low temperature, the strong interaction between the conduction electrons and the magnetic impurity binds them as a non-magnetic Kondo singlet.

$$\begin{aligned}
 H = & \sum_{k,\sigma} \epsilon_k \left(c_{k,\sigma}^\dagger c_{k,\sigma} \right) + \sum_i V(k) (c_{k,\sigma}^\dagger f_\sigma + h.c.) \rightarrow \text{valence} \\
 & + \epsilon_f \sum_\sigma n_\sigma^f + U n_\uparrow^f n_\downarrow^f \rightarrow \text{atomic}
 \end{aligned} \tag{1.4}$$

in which ϵ_k is the kinetic energy of conduction electrons, V is the hybridization between the impurity site and the conduction band, ϵ_f is the crystal fields of f -site and U is the on-site Coulomb interaction between electrons on the f -site.

Apparently the properties of the Anderson impurity model are determined by the competition between the valence fluctuation term and the atomic interaction term.

- **The non – interacting limit** In the non-interacting limit $U = 0$, if we integrate out the conduction electrons, the resulting f -electron Green's function is

$$G(\omega) = \frac{1}{\omega - (\epsilon_f - \mu) - \sum_k \frac{V^2(k)}{\omega - (\epsilon_k - \mu)}} \tag{1.5}$$

so that we can define a hybridization function $\Gamma(\omega) = \pi \sum_k V^2(k) \delta(\epsilon_k - \mu) \approx \pi V^2 \rho$, where we assume that $V(k) \approx V$ and ρ is the density of states at the Fermi surface. The spectra of f -electrons are broadened by $\Gamma(\omega)$ as the hybridization between conduction electrons and impurities, and are no longer a δ function at ϵ_f .

- **The atomic limit** In the atomic limit there is no valence fluctuation of electrons. The Hamiltonian is $H = \epsilon_f \sum_{\sigma} n_{\sigma}^f + U n_{\uparrow}^f n_{\downarrow}^f$. There are four possible configurations for this atom as shown in the Table 1.1,

Table 1.1: Electron occupation configuration of Anderson impurity model in the atomic limit as a function of on-site energy ϵ_f and Hubbard interaction U .

f^0	f^1	f^1	f^2
$ >$	$ \uparrow>$	$ \downarrow>$	$ \uparrow\downarrow>$
0	ϵ_f	ϵ_f	$U + 2\epsilon_f$

Clearly in order to have magnetic ground states, we must fulfill the requirement that $0 > \epsilon_f > -U$ or equivalently $\frac{U}{2} > \epsilon_f + \frac{U}{2} > -\frac{U}{2}$. The energy necessary to have excitations with respect to the magnetic ground states are

$$f^1 \rightarrow f^0, \Delta_E = -\epsilon_f > 0$$

$$f^1 \rightarrow f^2, \Delta_E = U + \epsilon_f > 0$$

As long as the thermal fluctuation $k_B T < \Delta_E$, the model is guaranteed to have a singly occupied state in the magnetic ground state whose spin forms the *local moment*.

The atomic limit results hint us there are three energy scales related to the Anderson model: 0, ϵ_f and $2\epsilon_f + U$, which are connected with $|>$, $|\uparrow>$ or $|\downarrow>$, $|\uparrow\downarrow>$ spin configurations respectively. At high temperature three energetic states are visited with the same probability. Suppose $2\epsilon_f + U > 0 > \epsilon_f$, then as the temperature is decreased to $\sim 2\epsilon_f + U$, the valence fluctuation $e^- + f^1 \rightleftharpoons f^2$ is going to be frozen. And at temperatures lower than this energy scale, the doubly occupied states are eliminated. As the temperature is further decreased, the valence fluctuations $f^1 \rightleftharpoons e^- + f^0$ are going to be frozen and the local moment states are formed. Later we will show below this energy scale the system is described by the Kondo model. As the temperature is further decreased to $\sim T_K$, a resonant quantum spin fluctuation $e_{\uparrow}^- + f_{\downarrow}^1 \rightleftharpoons e_{\downarrow}^- + f_{\uparrow}^1$ is formed. This is the Kondo resonance we discussed in the previous section. Below the Kondo temperature, the resonant spin tunneling of f -electron will form a spin singlet with the conduction electrons and in turn the local moment on f -band is screened.

1.3 Schrieffer–Wolff transformation

In the large U region, the charge fluctuation of the Anderson model can be eliminated by a unitary or canonical transformation. This work was done by Schrieffer and Wolff [8] and Coqblin and Schrieffer [2]. Considering two possible spin-exchange processes,

$$\begin{aligned} e_{\uparrow}^- + f_{\downarrow}^1 &\rightleftharpoons f^2 \rightleftharpoons e_{\downarrow}^- + f_{\uparrow}^1 & \Delta_{E1} &\sim U + \epsilon_f \\ h_{\uparrow}^+ + f_{\downarrow}^1 &\rightleftharpoons f^0 \rightleftharpoons h_{\downarrow}^+ + f_{\uparrow}^1 & \Delta_{E2} &\sim -\epsilon_f \end{aligned}$$

The first one is electron like and the second one is hole like. This is a second order process. Using the second order perturbation theory, the energy of singlet formation is

$$J \approx -2V^2 \left[\frac{1}{\Delta_{E1}} + \frac{1}{\Delta_{E2}} \right] \quad (1.6)$$

in which V is the hybridization at the Fermi surface $V \sim V(E_F)$. In the symmetry Anderson model where $\epsilon_f = -\frac{U}{2}$, we have

$$J \approx -\frac{8V^2}{U}$$

and

$$T_K \approx D e^{-\frac{U}{8V^2 \rho(\epsilon_F)}} \quad (1.7)$$

So in the large U region, the Anderson impurity model can be equivalently written as

$$H = \sum_{k,\sigma} \epsilon_k c_{k,\sigma}^\dagger c_{k,\sigma} + \frac{J}{N} \sum_{k,k'} c_{k,a}^\dagger \sigma_{ab} c_{k',b} \cdot S^f$$

after the Schrieffer–Wolff transformation. This is exactly the Kondo model we have seen in section 2.1. So here we proved that the Anderson impurity model can be transformed to the Kondo model at the large U region. The transformation can lead to an anti-ferromagnetic interaction between the local moment and the spins of conduction electrons, which is incurred by the exchange between the localized electron and the conduction electrons. This exchange is in both the electron channel and the hole channel.

From the discussion in section 2.1, we know that below temperature T_K the resonant singlet formation can screen the local moment on the f -band. For a more detailed derivation of the Schrieffer–Wolff transformation, please look at their reference papers.

Both the Kondo impurity model [3, 4] and the Anderson impurity model [5, 6] have exact Bethe Ansatz solutions. Although before the derivation of those exact solutions, some quantitative results have been acquired by the renormalization group theory, these results were proved to be important in understanding more details of the Kondo physics and in checking the theoretical prediction and approximations.

1.4 Periodic Anderson model

Principally, the Kondo scattering theory and the Anderson impurity only work well for metallic systems with dilute magnetic impurities. As the number of impurities in systems are increased or even as the concentration of impurities is one, the Anderson impurity model needs to be extended to its lattice version so as to correctly describe the systems. Consequently the periodic Anderson model (PAM) is introduced in which on every lattice site there is one impurity spin. The Hamiltonian of PAM reads

$$\begin{aligned}
H = & - \sum_{\langle i,j \rangle, \sigma} t_{i,j} \left(c_{i,\sigma}^\dagger c_{j,\sigma} + h.c. \right) + \sum_{i,\sigma} V_i \left(c_{i,\sigma}^\dagger f_{i,\sigma} + h.c. \right) \\
& + U \sum_i n_{i,\uparrow} n_{i,\downarrow}
\end{aligned} \tag{1.8}$$

Using the Schrieffer–Wolff transformation, accordingly the Kondo lattice model (KLM) is

$$H = - \sum_{\langle i,j \rangle, \sigma} t_{i,j} \left(c_{i,\sigma}^\dagger c_{j,\sigma} + h.c. \right) + \sum_i J_i s_i \cdot S_i^f \tag{1.9}$$

- **RKKY interaction** The PAM is not simply a multiple impurity version of the Anderson model. The most significant difference between the impurity Anderson model and the PAM is the existence of Ruderman-Kittel-Kasuya-Yosida (RKKY) interaction [7, 9, 10] in PAM. The impurities on neighboring sites can interact with each other through the conduction electrons, which is called the RKKY interaction. In metal, the magnetic impurity induces ‘Friedel’ oscillations of spin density wave in the surrounding valence electrons. Such spin polarization of valence electrons has the form

$$\langle \vec{\sigma}(x) \rangle = -2J \sum_{k,k'} \left(\frac{f(\epsilon_k) - f(\epsilon_{k'})}{\epsilon_{k'} - \epsilon_k} \right) e^{i(k-k') \cdot (x-x_0)} \langle \vec{S}(x_0) \rangle$$

in which $f(\epsilon_k)$ is the Fermion occupancy function at ϵ_k . Supposing there is another magnetic impurity at x , the interaction between the oscillating ‘Friedel’ spin and this second local moment is

$$H = \vec{J} \vec{S}(x) \cdot \vec{\sigma}(x) = J_{RKKY} \vec{S}(x) \cdot \vec{S}(x_0)$$

Naturally the RKKY coupling is

$$J_{RKKY} = -2J^2 \sum_{k,k'} \left(\frac{f(\epsilon_k) - f(\epsilon_{k'})}{\epsilon_{k'} - \epsilon_k} \right) e^{i(k-k') \cdot (x-x_0)}$$

This form of RKKY coupling can be simplified to

$$J_{RKKY} \approx -\rho J^2 \frac{\cos 2k_F r}{k_F r}$$

Clearly, *i*) such RKKY interaction is a long range interaction, and *ii*) the sign and amplitude of coupling J_{RKKY} is a function of the distance between the interacting impurities. So the RKKY interaction between impurities of different distance can be either FM or AFM. In a dilute magnetic system, the RKKY will lead to magnetic frustration, which results in a ground state called spin glass. In PAM, when the RKKY interaction is strong, usually the system will have an AFM order and the Fermi liquid theory is no longer valid.

The typical energy scale of RKKY interaction is

$$T_{RKKY} \approx \rho(\epsilon_F)J^2 \quad (1.10)$$

- **Doniach Phase diagram** The competition between the Kondo screening and the oscillating RKKY interaction leads to the famous Doniach phase diagram as shown in fig. 1.4 [11]. The Kondo screening prefers to form the Kondo singlet between the magnetic local moment and the conduction electrons and leads to a non-magnetic state which can be described by the Fermi liquid theory. But the long range RKKY interaction will form ferromagnetic (FM) or anti-ferromagnetic (AFM) order among the magnetic impurities. Suppose for a system there is only the Kondo screening effect, the dominant energy scale is T_K ; if in such a system there is only RKKY interaction, the energy scale to have magnetic ordering is T_{RKKY} (sometimes being call Neel temperature T_N or Curie temperature T_C as well). From formula 1.7 and 1.10 above, we can see that starting from zero and with ρJ increasing, T_{RKKY} is increasing and $T_K < T_{RKKY}$, the system is magnetic ordered and the real Neel temperature is increasing as well; but as T_K becomes larger the local moment begins to be screened, the Neel temperature T_N decreases after the maximum value; at the large ρJ side, since $T_K > T_{RKKY}$ there is no magnetic impurity due to the Kondo screening, and the system is described by the Fermi liquid theory. Although there is experimental evidence to support the Neel temperature line and the Fermi liquid temperature line meeting each other at zero temperature at some critical value $(\rho J)_c$, such a quantum phase transition scenario is still in controversy.

1.5 Heavy fermions

The term “heavy fermions” is used to describe materials with conduction electrons whose mass is much heavier ($\sim 10^2 - 10^3$ times) than the mass of free electrons. Specifically in condensed matter physics this term refers to the compounds containing elements with $4f$ or $5f$ electrons (those compounds with lanthanide or actinide elements). Usually because of strong correlations between the f electrons, the effective mass of the heavy fermion compounds is strongly renormalized to a large value; in turn the specific heat coefficient is much larger than the free electrons as well. It is widely accepted that such heavy fermion materials can be described by the **Kondo lattice model**. In heavy fermion compounds, the f electrons below the Fermi surface will form the magnetic local moment. So it is natural to expect the impurity Kondo model works for diluted heavy fermion compounds at the relative high and

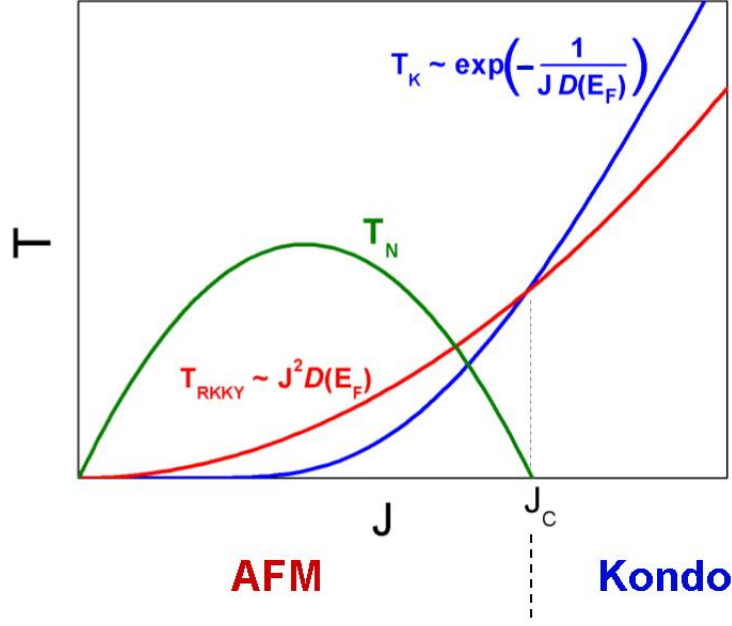


Figure 1.4: Doniach phase diagram.

intermediate temperature, where the correlation between magnetic impurities is not strong. But as the concentration of magnetic impurities is increased, the impurity Kondo model no longer works and we should use the Kondo lattice model. These predictions are confirmed by experimental results, like the measurement of the resistivity of compound $La_{1-x}Ce_xCu_6$ shown in figure 1.5. At $0 < x \leq 1$, the correlation between magnetic impurities are not important, and the resistivity shows a minimum as the temperature is decreased. But at large concentration, like $x = 1$, the resistivity as a function of temperature shows a maximum together with a minimum. This is because at large concentration as the temperature is decreased, the interactions between magnetic ions are no longer unimportant and finally order the magnetic ions. So the scattering of conduction electrons becomes coherent, in contrast with the in-coherent scattering mechanism of the Kondo impurity model, and will lead to a sudden decrement of the resistivity when the temperature is lower than T_{coh} .

- **Doping and pressure effect** As we have seen from equation 1.7 the Kondo temperature is exponentially increasing with the increased hybridization, the doping of ions and in turn the overlapping between the conduction electron and localized electron orbitals will tremendously change the T_K . For example, in material $Ce_{1-x}La_xAl_2$, T_K decreases an order of magnitude as x is increased; while for $Ce_{1-x}Y_xAl_2$, T_K increases as x is increased since the ions of Y have smaller orbitals. This hints that the Kondo temperature is also sensitive to external pressure and maybe the lattice oscillation effect as well. This is the Ce volume collapse problem we will discuss in chapter 3. Cerium, together with some lanthanide and actinide materials, will experience a volume collapse at a certain critical pressure. One popular theory to explain the Ce

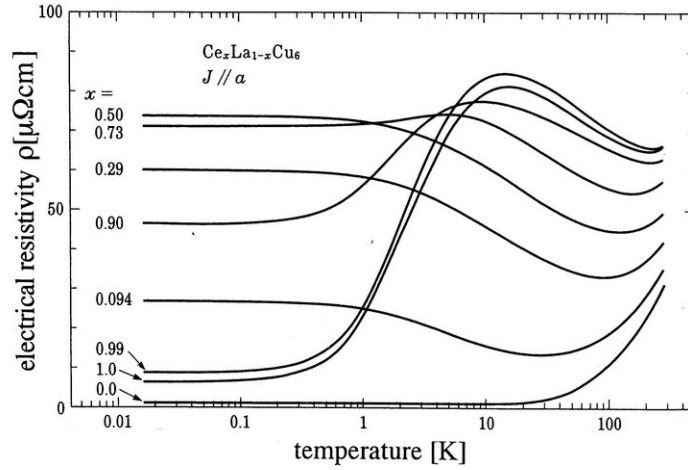


Figure 1.5: Resistivity vs. Temperature curves of $La_{1-x}Ce_xCu_6$ (from Sumiyama et al. (1986)) at different doping. There are both resistance minimum and maximum at large doping like $x = 0.99$ or 1.0 , while there is only a resistance minimum at small doping.

volume collapse problem is the so called “Kondo volume collapse” scenario proposed by Allen and Martin [51]. According to this theory, as the external pressure on Ce is increased, the hybridization between conduction and localized bands is increased as well, which will lead to a large increment of the Kondo temperature. So the Ce volume collapse is the consequence of a Kondo transition due to pressure increment. The “Kondo volume collapse” theory only includes the electronic degree of freedom, but as we will see later, the lattice oscillation degree of freedom can be important in this first order phase transition.

- Superconductivity and quantum phase transition** One of the most fascinating discoveries about the heavy fermion compounds is the existence of non-conventional superconductivity [12]. In conventional superconductivity, the magnetic moment will destroy the pairing mechanism of electrons and suppress the introduction of superconductivity. So for a long time, people didn’t believe there could be any superconductivity in the heavy fermion compounds. It is until much later that people realized that magnetic moment not only coexists with superconductivity, but also provides the pairing mechanism for such non-conventional superconductivity. The reason why the heavy fermion superconductivity is so important is due to its close relationship with the high temperature cuprate superconductivity. After people realize that the magnetic spin fluctuation can provide the pairing mechanism for the anisotropic d-wave pairs in heavy fermion superconductivity [13, 15, 14], this idea inspired the following theories to explain the high temperature cuprate superconductivity discovered in 1986 [16]. Now the heavy fermion compounds are even more interesting because of the discovery of quantum critical points driven by doping, magnetic fields or pressure. For example a general phase diagram of heavy fermions is shown in fig. 1.6. As you can see by tuning

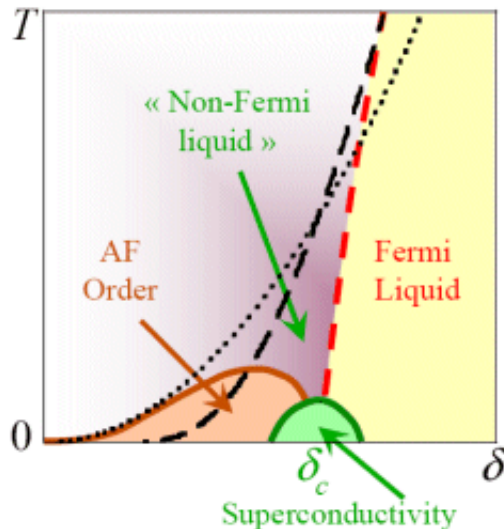


Figure 1.6: Heavy fermion general phase diagram. δ in figure represents the tuning parameter, which can be pressure, external magnetic fields or doping.

the parameter δ , a heavy fermion system can experience a quantum phase transition from one phase (AFM) to another phase (Fermi liquid) through a quantum critical point (QCP) at $T = 0$. In some compounds, such QCP is lying under the superconducting dome [17]. Even at well above this dome, the properties of the system are dominated by the so-called “non-Fermi liquid” behavior [18, 19]. I will not cover more contents on this topic. For readers who are interested in more details on this topic please read references [18, 19, 20, 21, 22].

1.6 Introduction of my works

Rare earth elements, like cerium, will experience a volume collapse when there is an increasing pressure acting on them. There has been a long effort to understand the mechanism behind this unusual iso-structural first order phase transition. Although different models have been proposed and they can give some qualitatively correct results, there is no conclusive theory which is widely accepted. Plus some recent experimental evidence proves lattice oscillation plays an important role in this phase transition, which totally overturns the old theory that this phase transition is mainly driven by spin and electronic factors. Motivated by those recent attentions to the role of phonons in the $\alpha - \gamma$ transition in Ce, the dynamical mean-field calculations are conducted for the periodic Anderson model in which the conduction band is coupled to phonons. This calculation yields a rich and unexpected phase diagram which is of intrinsic interest. Above a critical value of the electron-phonon interaction, a first-order transition with two coexisting phases develops in the temperature-hybridization plane, which terminates at a second-order critical point. The coexisting phases display the familiar Kondo screened and local-moment character, yet they also exhibit pronounced polaronic and

bipolaronic properties, respectively.

This work is collaborated with Peter Reis, Ka-Ming Tam, Mark Jarrell, Juana Moreno, Fakher Assaad, and A. K. McMahan and is published in Phys. Rev. B 87, 121102(R) (2013). In this work, an infinite-dimensional hypercubic lattice with Gaussian density of states $D(\epsilon) = \frac{1}{\sqrt{\pi}W} e^{-\left(\frac{\epsilon}{W}\right)^2}$ is used for the DMFT iteration. I am in charge of the coding the CTQMC+DMFT program and running the program in this project.

Chapter 2

The numerical algorithm

2.1 Model Hamiltonian

The model Hamiltonian of is,

$$\begin{aligned}
H &= H_0 + H_U + H_{e-ph}, \\
H_0 &= \sum_{k,\sigma} (\epsilon_k - \mu) \left(c_{k,\sigma}^\dagger c_{k,\sigma} + h.c. \right) + V \sum_i (c_{i,\sigma}^\dagger f_{i,\sigma} + h.c.) + (\epsilon_f - \mu) \sum_i n_i^f, \\
H_U &= U \sum_i \left(n_{\uparrow}^f - \frac{1}{2} \right) \left(n_{\downarrow}^f - \frac{1}{2} \right), \\
H_{e-ph} &= g_c \sum_i n_i^c X_i + g \sum_i n_i^f X_i + \sum_i \left(\frac{P_i^2}{2M} + \frac{k}{2} X_i^2 \right)
\end{aligned} \tag{2.1}$$

In the formula above $\sigma = \pm 1$ is the spin of electrons; μ is the chemical potential of system; $n^c = n_{\uparrow}^c + n_{\downarrow}^c$, $n^f = n_{\uparrow}^f + n_{\downarrow}^f$ represent electronic density on c and f bands respectively; $X = a + a^\dagger$, and a , a^\dagger are creation and annihilation operators of phonons.

Now we have three degrees of freedom: c-electron, f-electron and phonons. So the partition function of our Hamiltonian can be written into Grassmann Variables as follows,

$$\begin{aligned}
Z_{tot}[\bar{a}, a; \bar{c}, c; \bar{f}, f] &= \int D[\bar{a}, a] \int D[\bar{c}, c; \bar{f}, f] e^{-S_{tot}[\bar{a}, a; \bar{c}, c; \bar{f}, f]} \\
&= \int D[\bar{a}, a] \int D[\bar{c}, c; \bar{f}, f] e^{-S_e[\bar{c}, c; \bar{f}, f]} e^{-S_{e-ph}[\bar{a}, a; \bar{c}, c; \bar{f}, f]}
\end{aligned} \tag{2.2}$$

S_e is the pure electron action:

$$\begin{aligned}
S_e[\bar{c}, c; \bar{f}, f] &= \int_0^\beta d\tau \left\{ \sum_{k,\sigma} \bar{c}_{k,\sigma} [\partial\tau + (\epsilon_k - \mu)] c_{k,\sigma} + \sum_{i,\sigma} \bar{f}_{i,\sigma} [\partial\tau + (\epsilon_f - \mu)] f_{i,\sigma} + \right. \\
&\quad \left. V \sum_{i,\sigma} (\bar{c}_{i,\sigma} f_{i,\sigma} + h.c.) \right\} + U \sum_i \left(\hat{n}_{\uparrow}^f - \frac{1}{2} \right) \left(\hat{n}_{\downarrow}^f - \frac{1}{2} \right)
\end{aligned} \tag{2.3}$$

and S_{e-ph} is the action with both electron and phonon degrees of freedom

$$S_{e-ph}[\bar{a}, a; \bar{c}, c; \bar{f}, f] = \int_0^\beta d\tau \left\{ \sum_i \bar{a}_i \partial\tau a_i + g_c \sum_{i,\sigma} \hat{n}_i^c \hat{X}_i + g_f \sum_{i,\sigma} \hat{n}_i^f \hat{X}_i + \sum_n (\bar{a}_n a_n + \frac{1}{2}) \omega_0 \right\} \tag{2.4}$$

$\{\bar{a}, a\}$, $\{\bar{c}, c\}$ and $\{\bar{f}, f\}$ are Grassmann Variable representations of phonon, c-electron, f-electron creation and annihilation operators respectively. Noticed the highest order term of phonon is $\{c^2, c^{\dagger 2}, cc^\dagger\}$, so we can do a Hubbard–Stratonovich transformation[60] and integrate out phonon degree of freedom. After transformation, the electron-phonon action part will become,

$$Z_{e-ph} = \prod_m (-i\Omega_m + \omega_0)^{-2} e^{-\frac{1}{2}\omega_0\beta} \int D[\bar{c}, c; \bar{f}, f] \times e^{\sum_i \int_0^\beta d\tau \int_0^\beta d\tau' [\hat{n}_i^c(\tau)] D^0(\tau - \tau') [\hat{n}_i^c(\tau')] e^{\sum_i \int_0^\beta d\tau \int_0^\beta d\tau' [\hat{n}_i^f(\tau)] D^0(\tau - \tau') [\hat{n}_i^f(\tau')]} \quad (2.5)$$

in which $D^0(\tau - \tau')$ is the phonon retarded Green's function between electron densities,

$$D^0(\tau - \tau') = \frac{g^2}{2k} \frac{\omega_0}{2(1 - e^{-\beta\omega_0})} [e^{-|\tau - \tau'|\omega_0} + e^{-(\beta - |\tau - \tau'|)\omega_0}]$$

Finally we come to an effective Hamiltonian of our model,

$$\begin{aligned} H &= H_0 + H_U + H_{e-ph}, \\ H_0 &= \sum_{k,\sigma} (\epsilon_k - \mu) \left(c_{k,\sigma}^\dagger c_{k,\sigma} + h.c. \right) + V \sum_i (c_{i,\sigma}^\dagger f_{i,\sigma} + h.c.) + (\epsilon_f - \mu) \sum_i n_i^f, \\ H_U &= U \sum_i \left(n_\uparrow^f - \frac{1}{2} \right) \left(n_\downarrow^f - \frac{1}{2} \right), \\ H_{e-ph} &= \frac{g_c^2}{2k} \sum_i \int_0^\beta d\tau [\hat{n}_i^c(\tau)] D^0(\tau - \tau') [\hat{n}_i^c(\tau')] + \frac{g_f^2}{2k} \sum_i \int_0^\beta d\tau [\hat{n}_i^f(\tau)] D^0(\tau - \tau') [\hat{n}_i^f(\tau')] \end{aligned} \quad (2.6)$$

For a more detailed derivation, please look at A.6.

2.2 DMFT

In the past decades, DMFT[82] has been widely used in different area and tremendous new discovery has been achieved based on this theory. The basic idea of DMFT is since the actually system is usually too large to be solved numerically, we try to deal with the spatial correlation of system in a mean field level, but the time-dependent excitation on one site by all its neighbor sites will be preserved precisely. Follow this idea, we can treat a site in the lattice as an impurity embedded in a surrounding environment, as shown in cartoon 2.1. Explicitly, we assume $\Sigma(k, \omega) = \Sigma(\omega)$. This approximation will become exact in the limit $N \rightarrow \infty$, where N is the dimension of the lattice.

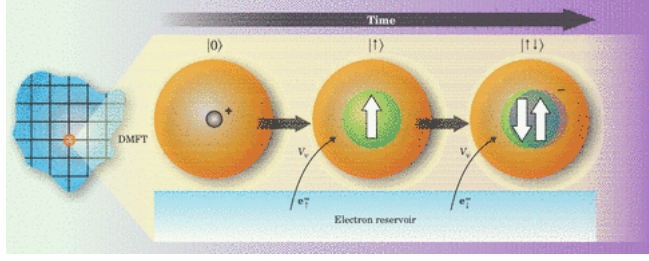


Figure 2.1: DMFT Cartoon

Through a self-consistent iteration like fig. 2.2, we will solving the DMFT equation. The impurity solver of the DMFT iteration can be either the theoretical or numerical method. In our case we use CTQMC as the impurity solver.

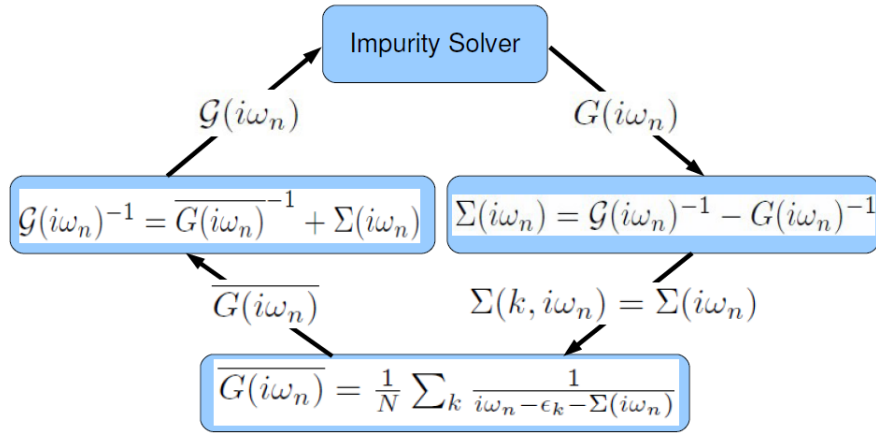


Figure 2.2: DMFT self-consistent iteration

2.3 CTQMC

In 2005, Rubtsov et al.[29] proposed a Continuous Time Quantum Monte Carlo method, which is based on weak coupling perturbation expansion of the partition function. Compared with discrete time Quantum Monte Carlo method, this method is free of Trotter-Suzuki error[61]. Besides, this method is very easily to be adapted to simulate different models, like our PAM+phonon model.

In the CTQMC algorithm, the partition function of the effective Hamiltonian is

$$\frac{Z}{Z_0} = \sum_{n=0}^{\infty} \frac{(-1)^n}{n!} \int_0^{\beta} d\tau_1 \sum_{V_1(\tau_1)} \omega[V_1(\tau_1)] \cdots \int_0^{\beta} d\tau_n \sum_{V_n(\tau_n)} \omega[V_n(\tau_n)] \langle T \hat{H}[V_1(\tau_1)] \cdots \hat{H}[V_n(\tau_n)] \rangle_0 \quad (2.7)$$

in which

$$V(\tau) = \{\tau', \sigma, \sigma', s, b\},$$

$$\sum_{V(\tau)} = \sum_{\sigma, \sigma', s, b} \int_0^\beta d\tau'$$

$$\omega[V(\tau)] = \delta_{b,0} \frac{U}{2} - \delta_{b,1} \frac{g_c^2}{2k} P(\tau - \tau') - \delta_{b,2} \frac{g_f^2}{2k} P(\tau - \tau')$$

$$\begin{aligned} H[V(\tau)] &= \delta_{b,0} \delta_{\sigma,\uparrow} \delta_{\sigma',\downarrow} \delta(\tau - \tau') [n_\uparrow^f(\tau) - \alpha_+(s)] [n_\downarrow^f(\tau') - \alpha_-(s)] \\ &+ \delta_{b,1} [n_\sigma^c(\tau) - \alpha_+(s)] [n_{\sigma'}^c(\tau') - \alpha_+(s)] + \delta_{b,2} [n_\sigma^f(\tau) - \alpha_+(s)] [n_{\sigma'}^f(\tau') - \alpha_+(s)] \\ \alpha_\sigma(s) &= \frac{1}{2} + \Delta s \sigma \end{aligned}$$

In the equation above b represents three different interaction $\{0, 1, 2\}$. They are Hubbard, $c - c$ retarded electronic interaction and $f - f$ retarded electronic interaction respectively. Δ is a tuning parameter to quench the possible minus-sign problem[62].

We can present these interactions diagrammatically in a real-imaginary time space, using color to denote up/down spins like Fig. 2.3.

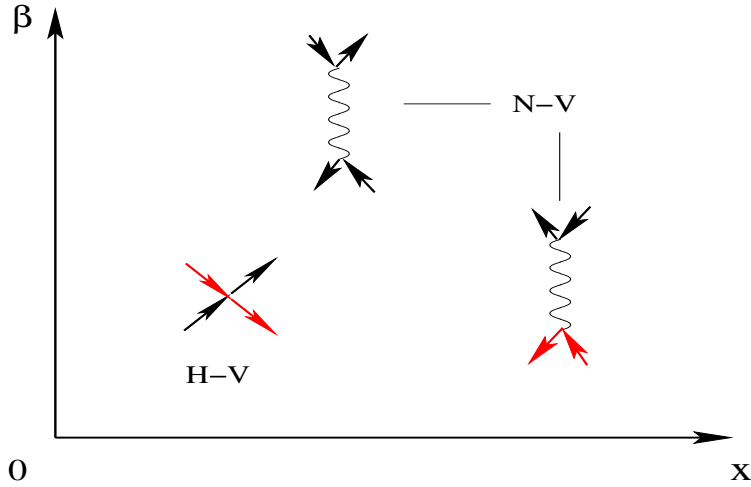


Figure 2.3: The vertex configuration of CTQMC for our model is shown diagrammatically. In this figure Hubbard Vertex(H-V) represents instant Hubbard interaction. The two Green's functions of H-V must have opposite spins. Non-local Vertex(N-V) represent retarded interaction between electronic densities of c or f bands. The two Green's functions of N-V can have either the same or opposite spins.

And the determinant of a configuration in equation 2.7 is calculated as following

$$\langle T[n^f(\tau_1) - \alpha_1][n^c(\tau_2) - \alpha_2] \cdots [n^c(\tau_i) - \alpha_i] \cdots [n^f(\tau_n) - \alpha_n] \rangle_{\sigma,0} = \quad (2.8)$$

$$\det \begin{vmatrix} g_{ff}^0(\tau_1, \tau_1) - \alpha_1 & g_{fc}^0(\tau_1, \tau_2) & \cdots & g_{fc}^0(\tau_1, \tau_i) & \cdots & g_{ff}^0(\tau_1, \tau_n) \\ g_{cf}^0(\tau_2, \tau_1) & g_{cc}^0(\tau_2, \tau_2) - \alpha_2 & \cdots & g_{cc}^0(\tau_2, \tau_i) & \cdots & g_{cf}^0(\tau_2, \tau_n) \\ \vdots & \vdots & \vdots & \vdots & \vdots & \vdots \\ \vdots & \vdots & \vdots & \vdots & \vdots & \vdots \\ \vdots & \vdots & \vdots & \vdots & \vdots & \vdots \\ g_{cf}^0(\tau_i, \tau_1) & g_{cc}^0(\tau_i, \tau_2) & \cdots & g_{cc}^0(\tau_i, \tau_i) - \alpha_i & \cdots & g_{cf}^0(\tau_i, \tau_n) \\ \vdots & \vdots & \vdots & \vdots & \vdots & \vdots \\ \vdots & \vdots & \vdots & \vdots & \vdots & \vdots \\ \vdots & \vdots & \vdots & \vdots & \vdots & \vdots \\ g_{ff}^0(\tau_n, \tau_1) & g_{fc}^0(\tau_n, \tau_2) & \cdots & g_{fc}^0(\tau_n, \tau_i) & \cdots & g_{ff}^0(\tau_n, \tau_n) - \alpha_n \end{vmatrix}$$

in equation 2.8 g^0 is the bare Green's function from the non-interaction part of the Hamiltonian.

A more detailed derivation of the weak coupling expansion CTQMC algorithm is given at Appendix A.

Chapter 3

The Ce volume collapse¹

3.1 Experimental background

Due to the complicated electronic structure and strong interaction between electrons, lanthanides, actinides (Fig. 3.1) and their chemical compounds show very rich phase transitions as a function of temperature or pressure. Among all these phase transitions, the most interesting one is the volume change driven by pressure [34, 35]. In Fig. 3.2, the room temperature Pressure-Volume curves of some lanthanide elements are shown. We can see for neodymium, promethium and samarium, the volume change is generally very small, like a few percent or even smaller. But we can also see there is remarkable volume collapse for cerium (at 0.9 GPa, 15% volume change, isostructural $fcc \rightarrow fcc$), praseodymium (at 20 GPa, 9% volume change, $d - fcc \rightarrow complex$) and gadolinium (at 59 GPa, 11% volume change, $d - fcc \rightarrow complex$). The “cmplx” in Figure 3.2 means a number of low symmetry, complex structures.

This volume change of lanthanide and actinide elements is believed to be connected to their electronic structure: $Ce(6s^2 4f^1 5d^1)$, $Pr(6s^2 4f^3)$, $Nd(6s^2 4f^4)$, $Pm(6s^2 4f^5)$, $Sm(6s^2 4f^6)$, and $Gd(6s^2 4f^7 5d^1)$. In these elements, on spd orbital there are broad itinerant electron bands, which make the material being metallic on both sides of the volume change. The f orbital electrons in the phase of the larger volume side are more localized while in the phase of the smaller volume side are more itinerant [37, 38]. Of all the rare earth materials, the electronic structure of Ce is the simplest one [36]. It has only one $4f^1$ electron and its volume change is isostructural. Therefore a lot of research interest is concentrated on Ce.

3.1.1 Phase diagram of Ce


Fig. 3.3 shows the full Pressure-Temperature phase diagram of Ce. Although the phase diagram is really complicated, what we are interested in is the $\gamma \rightarrow \alpha$ phase transition which is enclosed in the red rectangle. This volume collapse starts at about 200K. When the pressure on the material is increased, Ce will experience a volume decrease from γ phase (large volume) to α phase (small volume). This phase transition line persists as temperature increases, until ends at a critical point $P_c = 1.5 \pm 0.1 GPa$ and $T_c = 480 \pm 10 K$ [39].

Fig. 3.4 [39] is an isothermal scan of Pressure-Volume diagram of Ce at different temperature. From this diagram we can also see the volume change decrease as temperature increase and finally there is a critical point at T_c and P_c mentioned above.

3.1.2 Experiments

The magnetic susceptibility and specific heat [40] of Cerium has been measured at both sides of $\gamma \rightarrow \alpha$ phase transition. In γ phase people find a Curie-Weiss like behavior of magnetic

¹This chapter previously appeared as [“Periodic Anderson model with electron-phonon correlated conduction band”, Peng Zhang, Peter Reis, Ka-Ming Tam, Mark Jarrell, Juana Moreno, Fakher Assaad, Andy McMahan, Phys. Rev. B **87**, 121102 (2013)]. It is reprinted by permission of APS.

 **PERIODIC TABLE**

Representative Elements s-block		Transition Elements d-block										Representative Elements p-block						Noble gases 18
1												13 14 15 16 17						18
1	H																He	
2	Li	Be											B	C	N	O	F	Ne
3	Na	Mg	3	4	5	6	7	8	9	10	11	12	Al	Si	P	S	Cl	Ar
4	K	Ca	Sc	Ti	V	Cr	Mn	Fe	Co	Ni	Cu	Zn	Ga	Ge	As	Se	Br	Kr
5	Rb	Sr	Y	Zr	Nb	Mo	Tc	Ru	Rh	Pd	Ag	Cd	In	Sn	Sb	Te	I	Xe
6	Cs	Ba		Hf	Ta	W	Re	Os	Ir	Pt	Au	Hg	Tl	Pb	Bi	Po	At	Rn
7	Fr	Ra		Rf	Db	Sg	Bh	Hs	Mt									

Inner Transition Elements
f-block

La	Ce	Pr	Nd	Pm	Sm	Eu	Gd	Tb	Dy	Ho	Er	Tm	Yb	Lu
Ac	Th	Pa	U	Np	Pu	Am	Cm	Bk	Cf	Es	Fm	Md	No	Lr

Figure 3.1: Lanthanide and actinide elements in Periodic Table

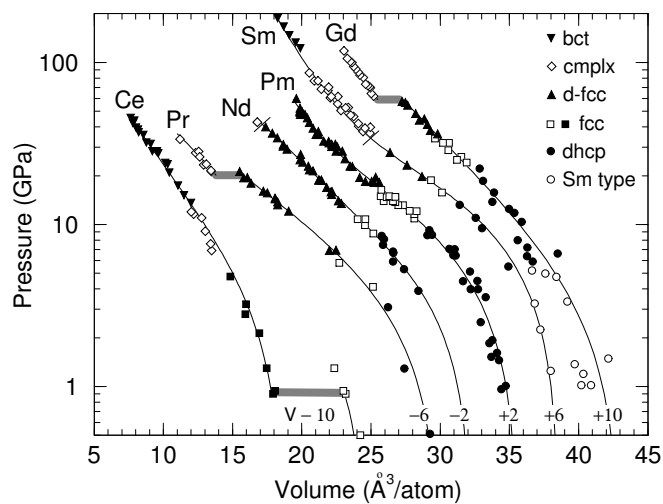


Figure 3.2: P-V diagram of some lanthanide elements at room temperature

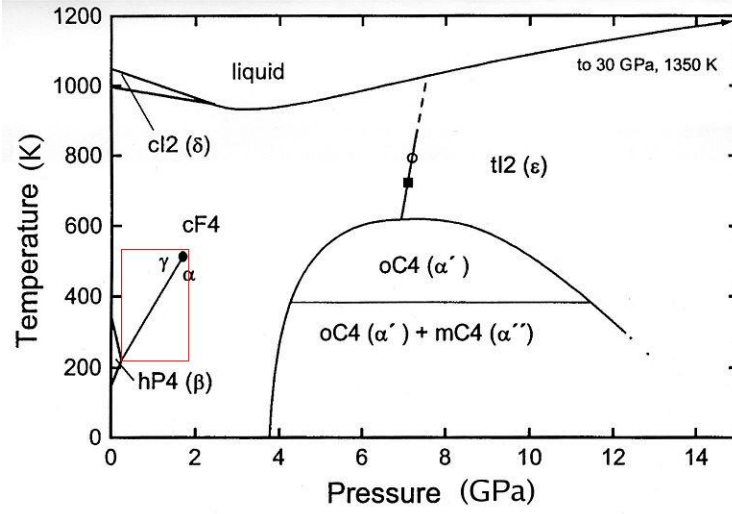


Figure 3.3: P-T full phase diagram of Ce.

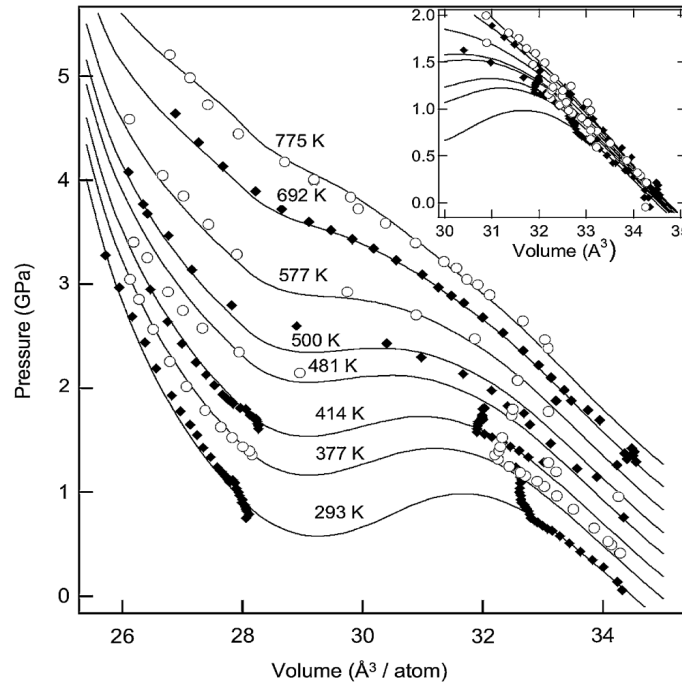


Figure 3.4: Isothermal scan of Pressure-Volume diagram of Ce at different temperatures

susceptibility and quite large specific heat compared with in α phase a Pauli like temperature independent magnetic susceptibility and the specific heat behaves like typical non-localized $4f$ electrons. These two observation suggested in γ phase and the larger volume side there is a local moment while in α phase this local moment is quenched.

3.2 Theories

3.2.1 Scenarios proposed for Ce volume collapse

Ever since in 1927 when Ce volume collapse was first reported by P.W. Bridgeman [41], the intriguing property of $\gamma \rightarrow \alpha$ volume collapse has lead to extensive work in order to understand the mechanism behind this physics.

- **Promotional model** The first attempt is the so-called promotional model proposed by L. Pauling and W.H. Zachariasen [42] in 1949. This theory claims that the $\gamma \rightarrow \alpha$ volume collapse is driven by squeezing the localized $4f$ electron in γ phase to the conduction band after the transition to the α phase. In Ce, the $4f$ level is localized in the inner orbital with much smaller radius compared with the $5d$ and $6s$ valence levels that located in the outer orbitals. If the $4f$ electron is pushed to the valence levels, the less screened nucleus will lead to a collapse of $5d$ and $6s$ orbitals, finally forming a much smaller Ce atom.

In order to push the $4f$ electron to the valence levels, the $4f$ electron must locate around the Fermi level, otherwise the energy provided by volume collapse transition is not enough to promote the $4f$ electron. The calculation of Coqblin and Blandin [43] indicates that the localized $4f$ electrons in the γ phase is at $\sim 0.1\text{ev}$ below the Fermi level and 0.1 to 0.15 ev above the Fermi level in the α phase.

This model was soon challenged by the work of Gustafson etc. [44, 45]. Their positron annihilation and angular correlation measurements of photon annihilation experiments show there is no significant change of conduction and f electrons in the $\gamma \rightarrow \alpha$ phase transition. The conclusion is also supported by x -ray absorption experiments and the Compton scattering experiments [46, 47]. Furthermore, the photo-emission experiments show that the $4f$ level in the γ phase lies about 2ev below the Fermi level, which is order of magnitude larger than the predication based on the promotional model.

- **Mott transition** Based on these further experimental evidences, in 1974 Johansson [48] proposed that the $\gamma \rightarrow \alpha$ phase transition is a Mott transition. In this model, as the volume of Ce is decreased because of external pressure, the electron hopping between neighbor sites increased, so that the localized magnetic $4f$ band in γ phase transfer to a still narrow but relatively broader $4f$ band in α phase. This is a Mott transition. In the α phase, there will be no local moment, and the system is in a paramagnetic Fermi liquid state. The smaller volume of α phase is due to the electron-binding in the metal. Based on this idea, a number of calculations have been done and some P-T phase diagrams can be get explicitly [49, 50].

Although the Mott transition scenario agree with some experiments, most experimental results point to the fact that valence electrons almost stay the same in both phases. A nature conjecture of Johansson's Mott transition theory would be the total delocalization of $4f$ electrons in α phase. But photo-emission experiments [52, 53] indicates the $4f$ electron exist for both α and γ phase. Differing from Johansson's prediction that the $4f$ band should extend across the Fermi level, the $4f$ band actually locate at an energy $\sim 2\text{ev}-3\text{ev}$ below the Fermi level. Plus a neutron scattering experiment by A.P. Murani et. al. [54] which measure the magnetic form factor and phonon density of states [72] independently shows magnetism exists on both side of phase transition.

- **Kondo volume collapse** Another popular theory about volume collapse is the so-called Kondo Volume Collapse suggested by J.W. Allen and R.M. Martin [51] in 1982. Viewed the success and problems of the Mott transition model, and based on the evidence of photo-emission and neutron scattering experiments above, it is natural to connect the volume collapse of Ce with the Kondo transition. According to the Kondo volume collapse scenario, in both the α and γ phase, a localized $4f$ electron moment always exists under the Fermi level. In the γ phase it is a "bare" local moment but in the α phase this moment is under the screen of conduction electron cloud. Starting from large volume, or γ phase side, as the pressure on Ce increased, and the volume decreased, the distance between Ce atoms will decrease, which in turn will enhance hybridization between the itinerant band and localized $4f$ band, plus the hybridization between the $4f$ band itself on neighboring sites. When the pressure reaches certain critical value at a certain temperature, the hybridization between the itinerant band and localized band will form a spin singlet. This non-bonding to bonding transition from γ to α phase is a possible explanation for the large volume change and loss of magnetic susceptibility. Although in the original paper of Allen and Martin they used an impurity Anderson model, their theory was extend to lattice version, the periodic Anderson model, to describe the volume collapse of Ce more properly.

Now consider the entropy change of this KVC model. In the γ phase, or low pressure, large volume, local moment side, the local moment will give out a electronic entropy $k_B * \ln(2J+1)$, here J is the moment from Hund's rule. And in the α phase, or the high pressure, small volume side, where the local moment is screened by conduction electrons, the non-degenerate ground state has the entropy of $k_B * \ln(1) = 0$. This fits perfectly in the experimental observation [52, 55]. And this theory fits the fact that the quasiparticle peak is only found in α phase.

3.3 Phonon crisis

For a long time it was widely believed either by the experimentalist or the theorist that the volume collapse is mainly driven by electronic and spin fluctuation degrees of freedom. If there is a lattice oscillation factor, its contribution is really small compared with the former two factors. In 2004, I. K. Jeong et al. [56] found lattice oscillation accounts for about half of the entropy change, $\Delta S_{vib}^{\gamma \rightarrow \alpha} \approx 0.75 \pm 0.15 k_B$, in the transition from γ to α phase, relative

to the total entropy change $\Delta S_{tot}^{\gamma \rightarrow \alpha} = 1.5k_B$. In their experiment, they did a high pressure, high resolution neutron scattering and synchrotron x -ray scattering measurement of Cerium across the $\gamma \rightarrow \alpha$. Their measurement of bulk modulus also pointed out phonon degrees of freedom do play a very important role in the $\gamma \rightarrow \alpha$ phase transition. Their discovery is confirmed by other x -ray diffraction experiment [39, 57], the ultrasonic experiment [73, 58].

Now the perfect prediction of KVC model come to a crisis since only electronic degree of freedom is included in this model. In paper [39] they find a profound change of the lattice Grueneisen parameter across the $\gamma \rightarrow \alpha$ phase transition, which reflect very different lattice oscillation modes in these two phases. Actually, it is more natural to conjecture if we believe the non-screening to screening Kondo physics truly drives the Ce volume collapse, then the electronic structure of material and the inter-atomic force and in turn the lattice oscillation should also changed. Data in paper [57] shows strong change of phonon dispersion between the $\gamma \rightarrow \alpha$ phase transition, which suggests a large change of electron-phonon interaction in two phases. And their *ab initio* fitting of data indicates in γ phase the $4f$ electron is localized while in α phase the $4f$ electron is partly in the conduction band.

Despite the increasing attention in the Ce literature has shifted to an appreciation that a significant fraction of the total entropy change across the transition may be due to phonons [72, 56, 73, 58, 74, 39, 57] over the past decade, studies focusing on the effect of phonons on the PAM are very limited [75, 76, 77, 78, 79]. Prior studies either are constrained to ground-state calculation or do not explore possible phase transitions in detail. To this end, we are motivated here to consider the PAM with Holstein phonons [80, 81]. As will be presented in section 3.5, since the coupling of phonons to the f electrons can lead to loss of local moments via electron condensation, we have chosen to couple the phonons to the conduction electrons. We find that the electron-phonon interaction above a critical strength induces a first order transition in the temperature-hybridization plane for the PAM-Holstein model. Strikingly the electron-phonon interaction also creates polaronic behavior in the Kondo screened phase and bipolaronic behavior in the local moment phase.

3.4 Numerical methods

The phonon crisis of cerium volume collapse calls for compromising of phonon degree of freedom together with electronic and spin fluctuation. From the experiment above, we already know KVC theory is the most successful model known for this problem. So we decided to use the PAM in the KVC theory as our starting point and include phonon factor to it. The problem is no one knows what is the proper way to coupling phonon to PAM.

For simplicity, we decided to choose the electron-phonon coupling with a Holstein phonon. There are three possible ways to couple this Holstein phonon to PAM,

- Couple phonon to the c band, $n^c X$, n^c is the density of c-band electrons and X is lattice displacement;
- Couple phonon to the f band, $n^f X$, n^f is the density of f-band electrons;
- Couple phonon to the hybridization term, $(c^\dagger f + h.c.)X$, c^\dagger is the creation operator of c-band electron and f is the annihilation operator of f-band electron.

In the paper of S. Capponi and F.F. Assaad [59], they show in the anti-adiabatic limit of phonon frequency coupling phonon to hybridization term will only enhance the Kondo screening, unless the PAM is in a mixed valence regime where charge fluctuation on the f -band is large. We know from previous experiment the f -electron is almost always localized on both sides of the volume collapse transition, which means the PAM model describing Ce volume collapse should have a $\langle n_f \rangle = 1$. So here we suppose phonon coupling to hybridization term will only renormalize the Kondo screening and not include this term in our Hamiltonian.

We have tested the electron-phonon interaction on both the c and f electrons. We measured some physical quantities, for example the double occupancy of f -band $D_f = \langle n_{\uparrow}^f n_{\downarrow}^f \rangle$, singlet correlated between c - f bands $\langle s^c s^f \rangle$, hybridization between the c and f bands $\Gamma = \langle c^\dagger f + f^\dagger c \rangle$, the time-integrate charge susceptibility on c band $\chi_c = \int_0^\beta d\tau \langle (n_{\uparrow}^c(\tau) + n_{\downarrow}^c(\tau))(n_{\uparrow}^c(0) + n_{\downarrow}^c(0)) \rangle$ and the time-integrate charge susceptibility on f band $\chi_f = \int_0^\beta d\tau \langle (n_{\uparrow}^f(\tau) + n_{\downarrow}^f(\tau))(n_{\uparrow}^f(0) + n_{\downarrow}^f(0)) \rangle$. We find in most cases coupling phonon to the f band of PAM will not change the physics as much as coupling to the c band. This might be a natural conclusion since in the anti-adiabatic limit of phonon $\omega_0 \gg 1$, the retarded interaction mediated by phonons turns into an instant attractive interaction. The coupling of phonons to the f electrons can lead to loss of local moments via electron condensation on the f band.

But coupling Holstein phonons to the c band leads to very interesting physics. At the large hybridization region, the conduction band electron will be scattered by local moment on f band. The hopping of the electrons between the c and f bands will finally create a singlet bond between electrons on these two orbitals. Now suppose we couple phonon to the c band, which mediate a retarded attractive interaction between c electrons. This phonon mediated attractive interaction will also prefer to form a bond between the c electrons, which will push the system to the local moment direction and lead to Kondo breakdown. So here phonon can possibly play the role like a tuning parameter for a first order phase transition from local moment \leftrightarrow Kondo singlet (the counter part in Ce volume collapse is the $\gamma \rightarrow \alpha$ phase transition). The very likely physics has been found experimentally by J.C. Lashley [63] where their tuning parameter is doping and magnetic field instead of lattice oscillation.

The Hamiltonian of the PAM-Holstein model is:

$$H = H_0 + H_U + H_{e-ph}, \quad (3.1)$$

$$H_0 = -t \sum_{\langle i,j \rangle, \sigma} \left(c_{i,\sigma}^\dagger c_{j,\sigma} + c_{j,\sigma}^\dagger c_{i,\sigma} \right) + \epsilon_f \sum_{i,\sigma} f_{i,\sigma}^\dagger f_{i,\sigma} \\ + V \sum_{i,\sigma} \left(c_{i,\sigma}^\dagger f_{i,\sigma} + f_{i,\sigma}^\dagger c_{i,\sigma} \right) + \sum_i \left(\frac{P_i^2}{2m} + \frac{1}{2} k X_i^2 \right)$$

$$H_U = U \sum_i n_{i,\uparrow}^f n_{i,\downarrow}^f$$

$$H_{\text{e-ph}} = g \sum_{i,\sigma} n_{i,\sigma}^c X_i,$$

where $c_{i,\sigma}$, $c_{i,\sigma}^\dagger$ ($f_{i,\sigma}$, $f_{i,\sigma}^\dagger$) are the creation and annihilation operators of the conduction (f level) at site i and spin σ ; $n_{i,\sigma}^c = c_{i,\sigma}^\dagger c_{i,\sigma}$ and $n_{i,\sigma}^f = f_{i,\sigma}^\dagger f_{i,\sigma}$ represent the occupation of the c and f electrons, respectively; t is the nearest-neighbor hopping; ϵ_f is the on-site energy of the f level; V is the hybridization between conduction and localized electrons; the on-site Hubbard interaction is U ; g is the electron-phonon coupling; X_i is the lattice displacement at site i , and P_i is its conjugate momentum.

Due to the absence of experimental evidence for long range ordering in Ce volume collapse in the primary range of interest at room temperature and above, together with the smooth Fermi surface we choose, dynamical mean field theory (DMFT) [82] is employed in our simulation. We use a hypercubic lattice in infinite dimensions with Gaussian density of states $D(\epsilon) = \frac{1}{\sqrt{\pi}W} e^{-(\frac{\epsilon}{W})^2}$. The bandwidth W is set to 1 as the unit of energy. In Ce the Fermi energy is about 6000 K and the Debye frequency is 110-160K [72, 57], therefore we set the phonon frequency $\omega_0 = 0.01$ at 1% of bandwidth. The Hubbard interaction is $U = 4.0$. The total electronic density is fixed at $n = 1.8$ by tuning the chemical potential, and we adjust ϵ_f so that $n_f = 1$ at $T = 0.1$ to ensure that a local moment is present at high temperatures. Therefore all data we show are for $n_f \sim 1.0$ and $n_c \sim 0.8$. The continuous time quantum Monte Carlo [29], generalized for electron-phonon coupling [30], is employed as the impurity solver.

3.5 Results

3.5.1 Effect of electron-phonon on c-band

Fig. 3.5 displays the local hybridization factor $\Gamma = \langle c_0^\dagger f_0 + h.c. \rangle$ (here zero denotes the impurity site) as a function of V for $\lambda = g^2/2k = 1.0$ and different values of inverse temperature β . As the temperature decreases, the slope of the Γ vs. V curve becomes progressively larger, which indicates that the system is approaching a critical point. Interestingly, the curves approximately cross at a critical hybridization $V_c \sim 0.96$.

The inset of Fig. 3.5 shows Γ vs. V at $\lambda = g^2/2k = 0.49$. Notice that for this value of coupling the slope does not become steeper as the temperature decreases, and the line crossing disappears. This indicates that the corresponding susceptibility reaches a plateau as a function of temperature. We believe $\lambda = g^2/2k = 0.49$ is the lower bound for the critical value of the electron-phonon coupling. For any electron-phonon coupling smaller than 0.49, including PAM, the slope changing feature and consequently the critical behavior are lost.

This conclusion is supported by the results of a scanning of λ at different value as shown in Fig. 3.6, 3.7, 3.8 and 3.9. For all results with electron-phonon coupling $\lambda < 0.49$, the Γ vs. V curves converge to its lowest temperature line; while for $\lambda > 0.5$ results, you can see that different iso-thermal scan of Γ vs. V curves cross at approximately $V_c \approx \lambda$.

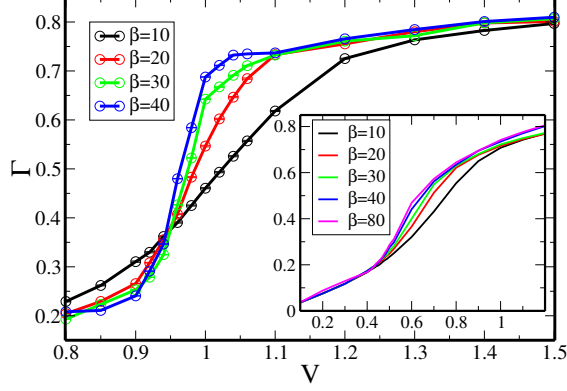


Figure 3.5: (color online) Isothermal scan of the hybridization factor $\Gamma = \langle c_0^\dagger f_0 + h.c. \rangle$ as a function of V at $g^2/2k = 1.0$. Γ increases monotonically with V . As the temperature decreases, Γ vs. V becomes steeper with a diverging slope near $V_c \sim 0.96$. Inset: Isothermal scan of the hybridization factor Γ as a function of V at $g^2/2k = 0.49$. Notice that the critical behavior has disappeared.

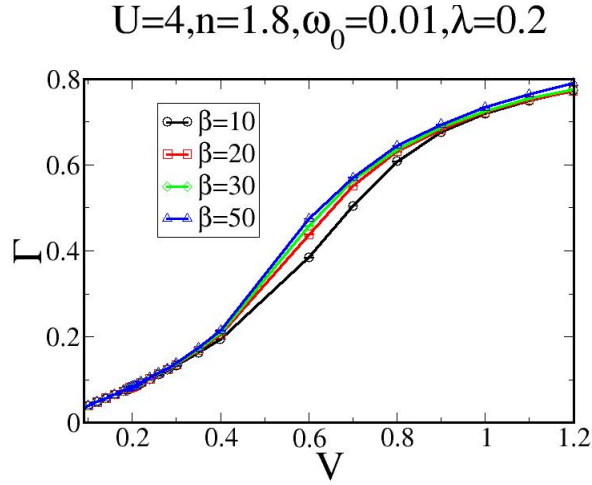


Figure 3.6: The iso-thermal scan of Γ vs. V at different temperatures. The electron-phonon coupling is $\lambda = g^2/2k = 0.2$. Other parameters are $n = n_c + n_f = 1.8$, $\omega_0 = 0.01$ and $U = 4.0$.

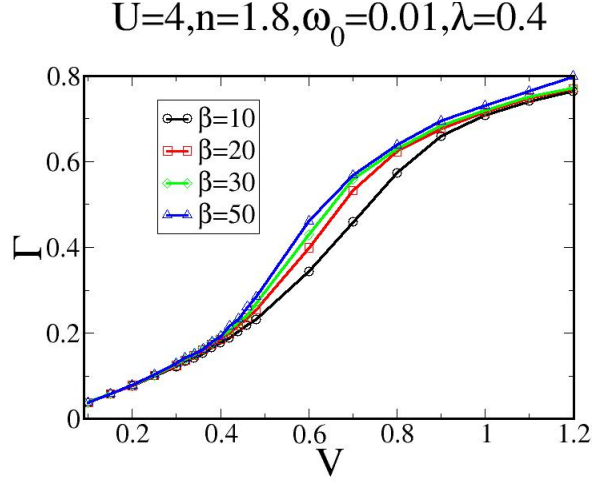


Figure 3.7: The iso-thermal scan of Γ vs. V at different temperatures. The electron-phonon coupling is $\lambda = g^2/2k = 0.4$. Other parameters are $n = n_c + n_f = 1.8$, $\omega_0 = 0.01$ and $U = 4.0$.

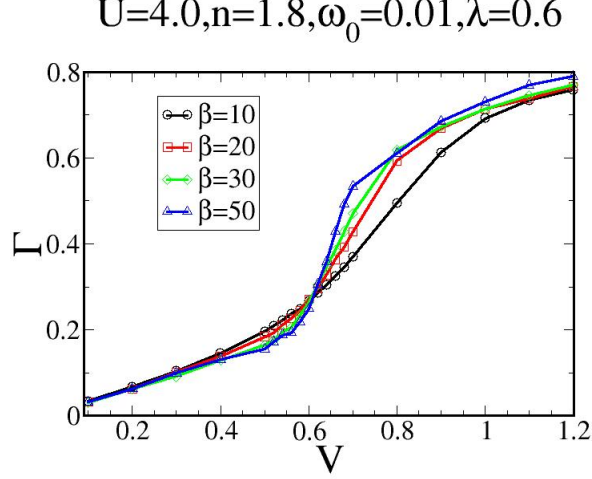


Figure 3.8: The iso-thermal scan of Γ vs. V at different temperatures. a) At electron-phonon coupling $\lambda = g^2/2k = 0.6$; b) At electron-phonon coupling $\lambda = g^2/2k = 0.8$. Other parameters are $n = n_c + n_f = 1.8$, $\omega_0 = 0.01$ and $U = 4.0$.

$$U=4, n=1.8, \omega_0=0.01, \lambda=0.8$$

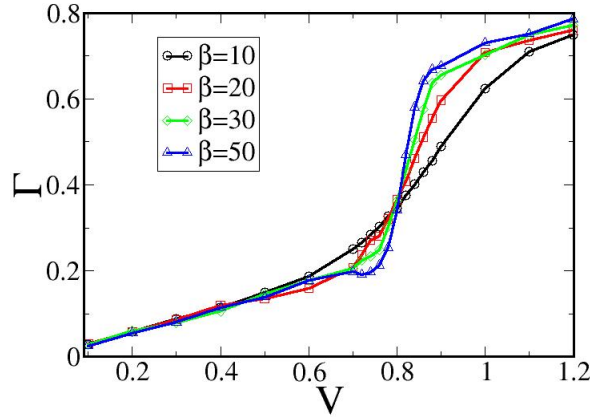


Figure 3.9: The iso-thermal scan of Γ vs. V at different temperatures. The electron-phonon coupling is $\lambda = g^2/2k = 0.8$. Other parameters are $n = n_c + n_f = 1.8$, $\omega_0 = 0.01$ and $U = 4.0$.

When the temperature is further decreased to $T = 0.0167$ ($\beta = 60$), Γ vs. V displays a hysteresis loop as shown in Fig. 3.10. The red line is obtained by starting at the large V side ($V = 1.2$), and using the output self-energy to initiate the simulation for the next smaller V . On the other hand, we obtain the black line by starting at $V = 0.8$ and using the output self-energy as the input for the next larger value of V . The coexistence of two solutions for the same value of V at $T = 0.0167$ is a direct evidence of a first order phase transition. The absence of such a hysteresis at higher temperatures indicates that the first order transition ends at a second order terminus (V_c, T_c).

For the same parameters, $V = 0.96$, $g^2/2k = 1.0$, $\omega_0 = 0.01$, and $U = 4.0$, we also perform a series of isothermal scans on the chemical potential to study the relationship between the total electron density $n = n_c + n_f$ and the chemical potential μ . As long as the temperature is not below $T = 0.0167$, the compressibility $\frac{dn}{d\mu}$ shows no tendency to diverge. This indicates that the phase transition here is not compressibility driven.

In Fig. 3.11 we show the temperature times the local f -orbital spin susceptibility, $T \cdot \chi_s^{ff}$, versus temperature. As T approaches zero, $T \cdot \chi_s^{ff}$ is roughly constant for $V = 0.8$, while it goes to zero for $V = 1.2$. This indicates that at $V = 0.8$ the f electrons display a robust local moment and paramagnetic local susceptibility with $1/T$ dependence, while at $V = 1.2$ the f local moments are quenched. The inset of Fig. 3.11 shows the f -orbital density of states (DOS) at $T = 0.01$. Notice that at $V = 0.8$ there is a gap across the Fermi level, while at $V = 1.2$ a Kondo resonance peak appears. The screening of the local moment in the large V region is a consequence of the singlet formation between c and f electrons.

The main panel of Fig. 3.12 shows the occupancy distribution histogram of the c electrons, $P(n_c)$, at $T = 0.0167$. $P(n_c)$ has been used to illustrate bipolaron formation [30]. At $V = 0.8$ the c -orbital electrons are in a bipolaronic state, which is characterized by the

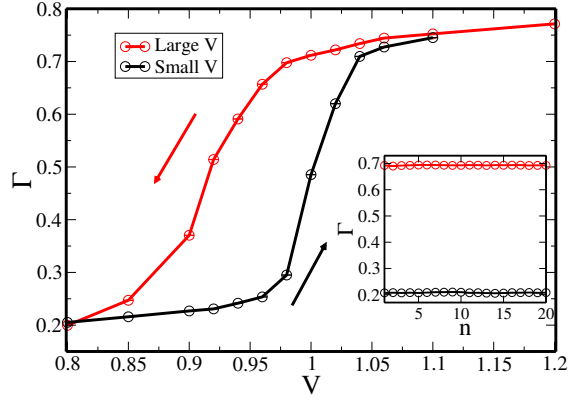


Figure 3.10: (color online) Hysteresis of Γ vs. V for $T = 0.0167$, $g^2/2k = 1.0$. The black line represents the small V branch of the hysteresis for which the self-energy of the previous simulation is used to initiate the calculation for the next larger value of V . While the red line represents the large V branch where starting with $V = 1.2$ we use the output of the previous simulation to initiate the computation at the next lower value of V . Inset: Γ as a function of the DMFT iteration number n for $V = 0.96$, $T = 0.0167$. The black (red) symbols represent the small (large) V branches.

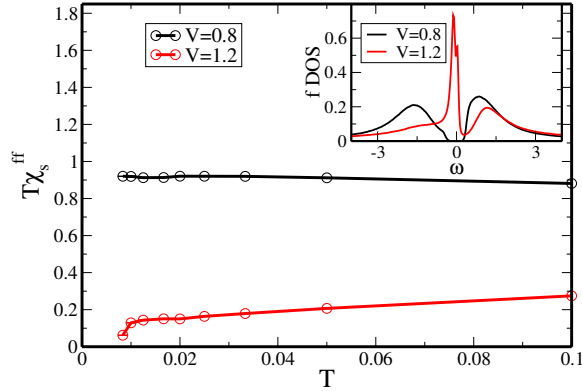


Figure 3.11: (color online) Temperature times the local f -orbital spin susceptibility, $T \cdot \chi_s^{ff}$, as a function of temperature for $g^2/2k = 1.0$. For $V = 0.8$ (black line), $T \cdot \chi_s^{ff}$ approaches a constant value as $T \rightarrow 0$ indicating an unscreened moment. For $V = 1.2$ (red line), $T \cdot \chi_s^{ff}$ converges to zero indicating the local moment is screened. Inset: The f -electron DOS at $T = 0.01$. The Kondo peak found for $V = 1.2$ (red line), but absent for $V = 0.8$ (black line) is consistent with the screened and unscreened scenarios in the main panel.

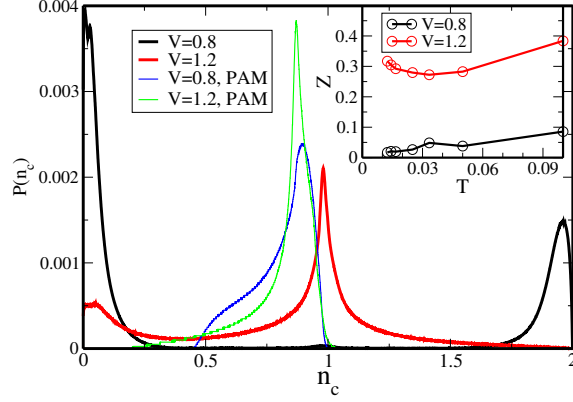


Figure 3.12: (color online) Occupancy distribution histogram of c -orbital $P(n_c)$ for $V = 0.8$ (black line) and 1.2 (red line), $T = 0.0167$ and $g^2/2k = 1.0$. For comparison, $P(n_c)$ of the PAM without electron-phonon coupling is plotted as well: $V = 0.8$ (blue line) and $V = 1.2$ (green line). Inset: the quasiparticle Z factor as a function of temperature for $V = 0.8$ (black line) and 1.2 (red line).

oscillation between zero and double occupancy, while for $V = 1.2$ the c electrons are in a polaronic state, where the occupancy oscillates between zero and one. For the PAM, without electron-phonon coupling, the structure of $P(n_c)$ is totally different. Here there is only one peak at roughly the c -electron filling $n_c = 0.8$, and $P(n_c)$ quickly decays to zero for n_c away from this filling. In the inset, the quasi-particle fraction Z is plotted as a function of temperature. The quasi-particle fraction is calculated for the lower quasiparticle band at the Fermi level using a generalization of the single band formulation [83]. The main component of this approach is to make the replacement $\frac{d\text{Re}\Sigma(\omega)}{d\omega}|_{\omega=0} \approx \frac{\text{Im}\Sigma(i\pi T)}{\pi T}$, which becomes exact at zero temperature. As $T \rightarrow 0$, Z goes to zero for $V = 0.8$, indicating non-Fermi-liquid behavior, while it converges to a finite value for $V = 1.2$, the signature of Fermi-liquid formation.

Here we need to emphasize that such Kondo singlet to local moment phase transition is found in a large parameter region. For example adjusting the total filling to $n = 1.6$ as shown in Fig. 3.13. The Γ vs. V isothermal scan lines are crossing with each other at around $V_c = 0.96$.

Or changing the Hubbard interaction to $U = 3.8$ as shown in Fig. 3.14. The Γ vs. V isothermal scan lines are crossing with each other at around $V_c = 0.96$.

Or increasing the phonon frequency to $\omega_0 = 0.02$ and 0.05 as shown in Fig. 3.15 and 3.16. The Γ vs. V isothermal scan lines are crossing with each other at around $V_c = 0.96$.

As long as keeping $g^2/2k$ fixed at 1.0 , for all these different parameters we can find that the isothermal Γ vs. V curves still cross and their slopes diverge at a critical value of the hybridization, V_c , as the temperature is decreased. Such discovery indicates that this first order phase transition exists in a wide parameter region. Look through the Figures 3.5, 3.6 and 3.8, we can also find that the critical hybridization V_c , where the Γ vs. V curves overlapped, is a functional of the electron phonon coupling $g^2/2k$. This phenomenon hints

$$U=4.0, n=1.6, \omega_0=0.01, \lambda=1.0$$

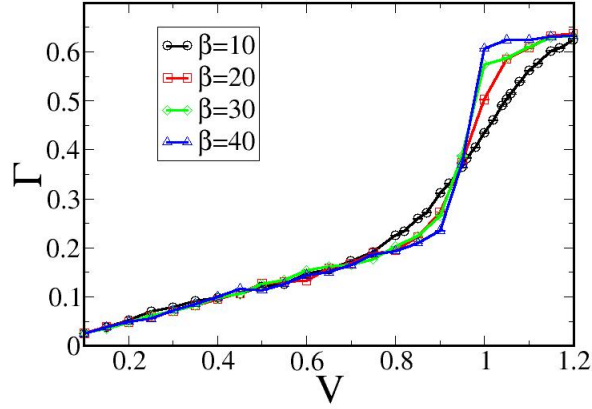


Figure 3.13: The iso-thermal scan of Γ vs. V at different temperatures. Other parameters are $\lambda = g^2/2k = 1.0$, $n = n_c + n_f = 1.6$, $\omega_0 = 0.01$ and $U = 4.0$.

$$U=3.8, n=1.8, \omega_0=0.01, \lambda=1.0$$

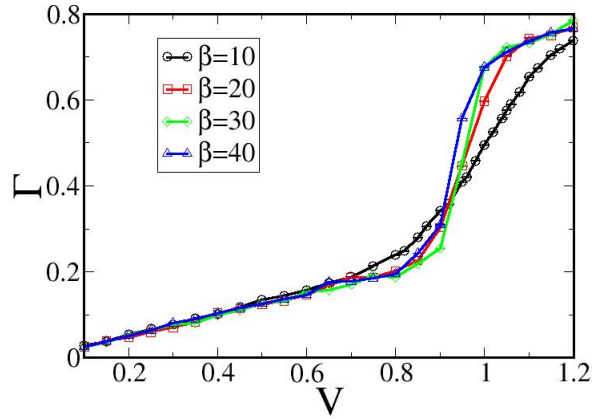


Figure 3.14: The iso-thermal scan of Γ vs. V at different temperatures. Other parameters are $\lambda = g^2/2k = 1.0$, $n = n_c + n_f = 1.8$, $\omega_0 = 0.01$ and $U = 3.8$.

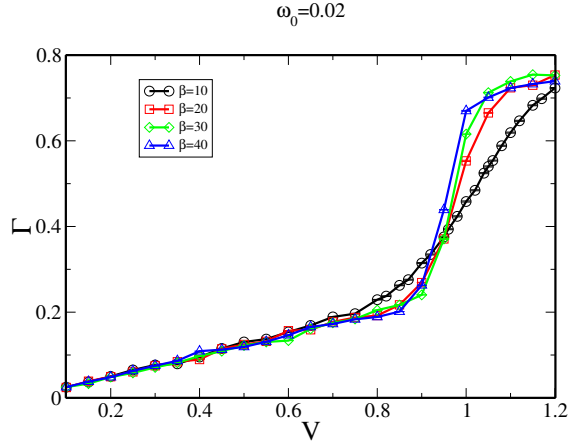


Figure 3.15: The iso-thermal scan of Γ vs. V at different temperatures. The bare phonon frequency is $\omega_0 = 0.02$. Other parameters are $\lambda = g^2/2k = 1.0$, $n = n_c + n_f = 1.8$ and $U = 4.0$.

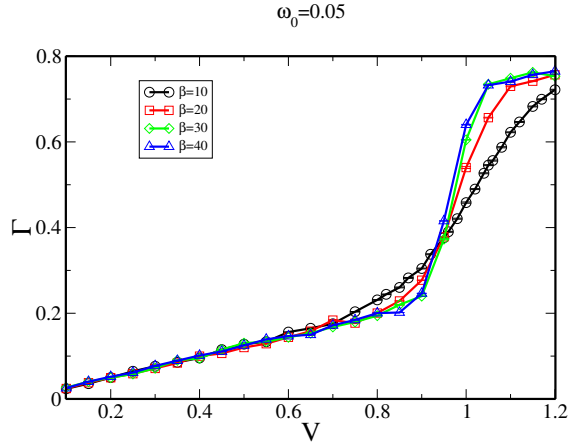


Figure 3.16: The iso-thermal scan of Γ vs. V at different temperatures. The bare phonon frequency is $\omega_0 = 0.05$. Other parameters are $\lambda = g^2/2k = 1.0$, $n = n_c + n_f = 1.8$ and $U = 4.0$.

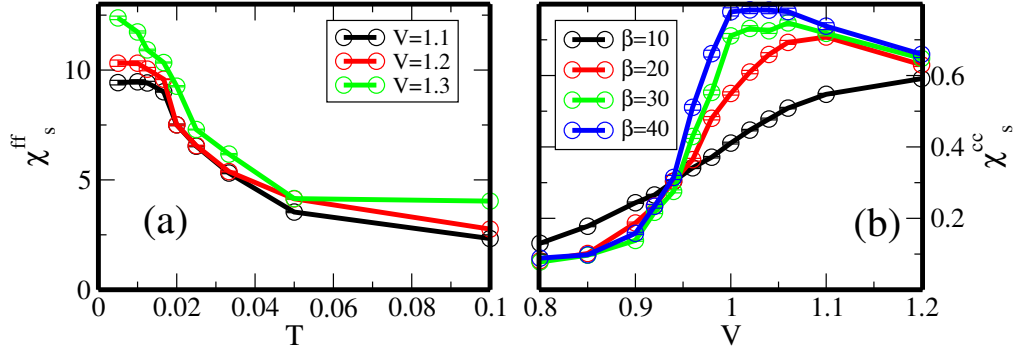


Figure 3.17: (color online) Panel (a) shows the f -orbital time integrated local spin-spin correlation, χ_s^{ff} , as a function of temperature for $V = 1.1, 1.2$ and 1.3 . Panel (b) shows the c -orbital time integrated local spin-spin correlation function, χ_s^{cc} , as a function of V for different temperatures.

us that we may push the first-order phase transition we found here to a quantum phase transition and the second-order critical point to a quantum critical point by tuning the electron-phonon coupling.

In Fig. 3.17(a) the time integrated local f -orbital spin-spin-correlation function, χ_s^{ff} , is plotted as a function of temperature for $V = 1.1, 1.2$, and 1.3 . We identify the Kondo scale T_K as the energy where χ_s^{ff} falls to around half of its low-temperature value. We find that T_K changes very little as V increases, so the line V vs. T_K should have a large slope. Fig. 3.17(b) shows the time integrated local c -orbital spin-spin-correlation function, χ_s^{cc} vs. V , at different temperatures, where large values reflect the c electron spin degeneracy in the polaronic state in contrast to the small susceptibility for the spinless bipolarons. For $V < 0.96$ the curves almost overlap for all $T < 0.1$. In fact, the corresponding c -electron occupancy histograms (not shown) show an obvious bipolaronic double peak feature even at relatively high temperatures like $T = 0.1$. If we define T^* as the energy where bipolaron formation begins, then the line T^* vs. V must be nearly horizontal.

We have also calculated the renormalized phonon frequency. At $T = 0.025$ it is roughly constant for hybridization $V > 0.96$; however, it drops precipitously for $V < 0.96$, decreasing by half when $V = 0.8$. This behavior softens with increasing temperature; e.g., a more gradual decrease begins for $V < 1.2$ at $T = 0.1$. This indicates an important temperature dependence of the phonons properties. Indeed, the analysis in [39] for Ce found that the temperature dependence of the phonons was a critical factor for obtaining a significant phonon contribution to the entropy change across the γ - α transition [72, 56, 73, 58, 74, 39, 57].

3.5.2 Phase diagram

Fig. 3.18 is a schematic summary of our findings. Two phases, local-moment+bipolaron and Kondo singlet+polaron, are separated by a first order transition line, which terminates at a second order critical point (V_c, T_c) . The positive slope of the V vs. T first order transition line is a consequence of a Clausius-Clapeyron-like relation where hybridization V is the

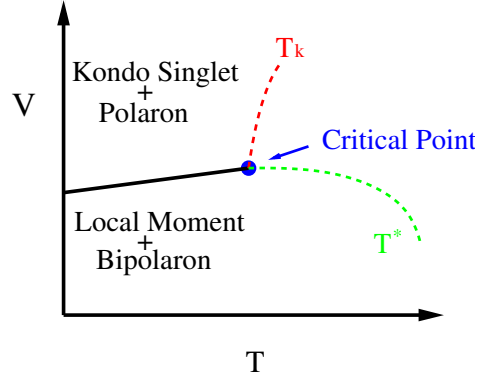


Figure 3.18: (color online) Schematic V vs. T phase diagram. The solid black line represents the first order phase transition which separates the local moment-bipolaron phase for small hybridization V from the Kondo singlet-polaron phase for large V . This first order transition line terminates at a second order critical point. The red dashed line coming out of the critical point represents the Kondo scale T_K and the green dashed line the bipolaron energy scale T^* .

analog of pressure. There is no broken symmetry between these two phases, as we can move adiabatically from one to another by wandering around the critical point. Both phases are destroyed by increasing the temperature. In order to have such a first order phase transition, the electron-phonon coupling on the c band must be larger than a certain critical value. The fact that the critical temperature is a function of electron-phonon coupling implies that the critical point touches zero temperature at some g_c , where the first order phase transition becomes a quantum phase transition tuned by V .

The DMFT calculations for the Hubbard-Holstein Hamiltonian [84, 85, 86] allow us to comment on the difference between the Mott-Hubbard+phonon model and our PAM+phonon model. Both models predict a bipolaronic insulating phase at some finite g , although with different slopes as a function of increasing hybridization (f - f or f -valence). The fundamental topological difference is that for the Hubbard-Holstein model, the γ phase (insulating) has a first order transformation to the bipolaronic insulating phase with increasing g , while for the PAM-Holstein model, the γ phase (local moment) can always be evolved continuously to the bipolaronic insulator phase.

3.6 Conclusion and future directions

When the conduction band of the PAM is coupled to phonons, one obtains a rich and unexpected phase diagram. Above a critical strength of the electron-phonon coupling a first order transition with two coexisting phases develops in the temperature-hybridization plane. This transition terminates at a second order critical point. These coexisting phases correspond to the familiar Kondo screened and local moment regions of the PAM, yet, they additionally

exhibit pronounced polaronic and bipolaronic behavior, respectively. While the PAM and its impurity variant have been paradigms for the α - γ transition in Ce, additional electronic bands not considered here might be needed in a generalization of the present PAM-Holstein model to more completely explain the volume collapse. Nonetheless, the present results suggest that electron-phonon effects become more important in Ce at weaker hybridization (lower pressure), that there is profound temperature dependence to the phonons in the γ as distinct from the α phase, and that the polaronic effects seen here are consistent with the superconductivity observed [87] in Ce at much lower temperatures [$T < O(1 \text{ K})$] at pressures above 2 GPa. That the effects seen here are more striking in the γ phase is no accident, as only for this phase are the characteristic phonon energies (Debye temperature) [57] comparable to the critical energy scale of hybridization between $4f$ and valence electrons (Kondo temperature) [68, 67].

Bibliography

- [1] Jun Kondo, Resistance Minimum in Dilute Magnetic Alloys, Progress of Theoretical Physics 32, 37 (1964).
- [2] Coqblin, B., and J. R. Schrieffer, Exchange Interaction in Alloys with Cerium Impurities, Phys. Rev. 185, 847 (1969).
- [3] N. Andrei, Diagonalization of the Kondo Hamiltonian, Phys. Rev. Lett. 45, 379 (1980).
- [4] P. B. Wiegmann, Quantum Inverse Scattering Method and Correlation Functions, Sov. Phys. JETP Lett. 31, 392 (1980).
- [5] P. B. Wiegmann, Towards the solution of Anderson model, Phys. Lett. 80A, 163 (1980).
- [6] N. Kawakami, & A. Okiji, Exact expression of the ground-state energy for the symmetric anderson model, Phys. Lett. A 86, 483 (1981).
- [7] Ruderman, M. A., and C. Kittel, Indirect Exchange Coupling of Nuclear Magnetic Moments by Conduction Electrons, Phys. Rev. 96, 99 (1954).
- [8] Schrieffer, J. R., and P. Wolff, Relation between the Anderson and Kondo Hamiltonians, Phys. Rev. 149, 491 (1966).
- [9] Kasuya, T., A Theory of Metallic Ferro- and Antiferromagnetism on Zener's Model, Prog. Theo. Phys. 16, 45 (1956).
- [10] Yosida, K., Magnetic Properties of Cu-Mn Alloys, Phys. Rev. 106, 893 (1957).
- [11] S. Doniach, The Kondo lattice and weak antiferromagnetism, Physica B 91, 231 (1977).
- [12] Steglich, F., J. Aarts, C. D. Bredl, W. Leike, D. E. M. W. Franz, and H. Schaefer, Superconductivity in the Presence of Strong Pauli Paramagnetism: $CeCu_2Si_2$, Phys. Rev. Lett 43, 1892 (1979).
- [13] Monod, M. T. B., C. Bourbonnais, and V. Emery, Possible superconductivity in nearly antiferromagnetic itinerant fermion systems, Phys. Rev. B. 34, 7716 (1986).
- [14] Scalapino, D. J., E. Loh, and J. E. Hirsch, d-wave pairing near a spin-density-wave instability, Phys. Rev. B 34, 8190 (1986).

- [15] Miyake, K., S. S. Rink, and C. M. Varma, Spin-fluctuation-mediated even-parity pairing in heavy-fermion superconductors, *Phys. Rev. B* **34**, 6554 (1986).
- [16] J. G. Bednorz, K. A. Mueller, Possible high T_c superconductivity in the Ba-La-Cu-O system, *Zeitschrift für Physik B* **64** (2): 189–193 (1986).
- [17] J. Flouquet, et al., Magnetism and superconductivity of heavy fermion matter, *Comptes Rendus Physique*, **7**, 22 (2006); P. Thalmeier et al., *Frontiers in Superconducting Materials* (Springer, Berlin, 2005) Chap. 3; C. Pfleiderer, Superconducting phases of f-electron compounds, arXiv : 0905.2625v1.
- [18] G.R. Stewart, Non-Fermi-liquid behavior in d- and f-electron metals, *Rev. Mod. Phys.* **73**, 797 (2001).
- [19] Stewart, G., Addendum: Non-Fermi-liquid behavior in d- and f-electron metals, *Rev. Mod. Phys.* **78**, 743 (2006).
- [20] Coleman, P., C. Pépin, Q. Si, and R. Ramazashvili, How do Fermi liquids get heavy and die?, *J. Phys. Cond. Matt.* **13**, 273 (2001).
- [21] Varma, C., Z. Nussinov, and W. van Saarloos, Singular or non-Fermi liquids, *Phys. Rep.* **361**, 267 (2002).
- [22] von Löhneysen, H., A. Rosch, M. Vojta, and P. Wolfe, Fermi-liquid instabilities at magnetic quantum phase transitions, *Rev. Mod. Phys.* **79**, 1015 (2007).
- [23] T. M. Rice and K. Ueda, *Phys. Rev. B* **34**, 6420 (1986).
- [24] S. Burdin, A. Georges, and D. R. Grempel, Coherence Scale of the Kondo Lattice, *Phys. Rev. Lett.* **85**, 1048 (2000).
- [25] T. Pruschke, R. Bulla, and M. Jarrell, Low-energy scale of the periodic Anderson model, *Phys. Rev. B* **61**, 12799 (2000).
- [26] F. F. Assaad, Coherence scale of the two-dimensional Kondo lattice model, *Phys. Rev. B* **70**, 020402(R) (2004).
- [27] A. Migdal, Interaction between electrons and lattice vibrations in a normal metal, *JETP* **34**, 996 (1958).
- [28] K. Mitsumoto and Y. Ōno, Phonon softening and double-well potential formation due to electron–phonon interaction in heavy-fermion systems, *Physica C* **426**, 330 (2005).
- [29] A. N. Rubtsov, V. V. Savkin, and A. I. Lichtenstein, Continuous-time quantum Monte Carlo method for fermions, *Phys. Rev. B* **72**, 035122 (2005).

- [30] F. F. Assaad and T. C. Lang, Diagrammatic determinantal quantum Monte Carlo methods: Projective schemes and applications to the Hubbard-Holstein model, *Phys. Rev. B* **76**, 035116 (2007).
- [31] F. F. Assaad, Spin, charge, and single-particle spectral functions of the one-dimensional quarter filled Holstein model, *Phys. Rev. B* **78**, 155124 (2008).
- [32] K. S. D. Beach, Identifying the maximum entropy method as a special limit of stochastic analytic continuation, arXiv:cond-mat/0403055 (unpublished).
- [33] K. S. D. Beach and F. F. Assaad, Coherence and metamagnetism in the two-dimensional Kondo lattice model, *Phys. Rev. B* **77**, 205123 (2008).
- [34] Benedict, U., Pressure-induced phase transitions in 5f and 4f metals and compounds, *J. Alloys Comp.* 193 (1993) 88.
- [35] Holzapfel, W. B., Structural systematics of 4f and 5f elements under pressure, *J. Alloys Comp.* 223, 170 (1995).
- [36] A. K. McMahan et al., Volume-Collapse Transitions in the Rare Earth Metals, *J. Comput.-Aided Mater. Des.* 5, 131 (1998).
- [37] J. M. Lawrence, P. M. Riseborough, and R. D. Parks, Valence fluctuation phenomena, *Rep. Prog. Phys.* 44, 1 (1981).
- [38] D. Koskenmaki and K. Gschneider, Handbook on the Physics and Chemistry of Rare Earths, edited by K. A. Gschneider and L. Eyring (North-Holland, Amsterdam, 1978).
- [39] M. J. Lipp, etc., Thermal Signatures of the Kondo Volume Collapse in Cerium, *Phys. Rev. Lett.* 101, 165703 (2008).
- [40] D. C. Koskimaki and K. A. Gschneidner, Jr., Heat capacity and magnetic susceptibility of single-phase α -cerium, *Phys. Rev. B* 11, 4463 (1975).
- [41] P.W. Bridgman, The compressibility and pressure coefficient of resistance of ten elements, *Proc. Am. Acad. Arts Sci.* 62, 207 (1927).
- [42] W. H. Zachariasen, quoted by A.W. Lawson and T.-Y. Tang, Concerning the High Pressure Allotropic Modification of Cerium, *Phys. Rev.* 76, 301 (1949); L. Pauling, quoted by A. F. Schuch and J. H. Strudivant, The Structure of Cerium at the Temperature of Liquid Air, *J. Chem. Phys.* 18, 145 (1950).
- [43] B. Coqblin and A. Blandin, Stabilité des Moments Magnétiques Localisés dans les Métaux, *Adv. In Phys.* 17, 281 (1968).
- [44] D. R. Gustafson, J. D. McNutt, and L. O. Roellig, Positron Annihilation in γ - and α -Cerium, *Phys. Rev.* 183, 435 (1969).

- [45] R. F. Gempel, D. R. Gustafson, and J. D. Willenborg, Investigation of the Electronic Structure of α' -Cerium by Angular-Correlation Studies of Positron-Annihilation Radiation, *Phys. Rev. B* 5, 2082 (1972).
- [46] B. Lengeler, G. Materlik, and J. E. Müller, L-edge x-ray absorption spectra of γ - and α -cerium, *Phys. Rev. B* 28, 2276 (1983).
- [47] U. Kornstädt, R. Lässer, and B. Lengeler, Investigation of the $\gamma - \alpha$ phase transition in cerium by Compton scattering, *Phys. Rev. B* 21, 1898 (1980).
- [48] B. Johansson, The $\alpha - \gamma$ transition in cerium is a Mott transition, *Philos. Mag.* 30, 469 (1974).
- [49] B. Johansson, I. A. Abrikosov, M. Alden, A.V. Ruban, and H. L. Skriver, Calculated Phase Diagram for the $\alpha - \gamma$ Transition in Ce, *Phys. Rev. Lett.* 74, 2335 (1995).
- [50] A. Svane, Electronic structure of cerium in the self-interaction-corrected local-spin-density approximation, *Phys. Rev. B* 53, 4275 (1996); J. Laegsgaard and A. Svane, Theory of the $\alpha - \gamma$ phase transition in Ce, *Phys. Rev. B* 59, 3450 (1999).
- [51] J. W. Allen and R. M. Martin, Kondo Volume Collapse and the $\alpha - \gamma$ Transition in Cerium, *Phys. Rev. Lett.* 49, 1106 (1982).
- [52] J. W. Allen et al., Resonant Photoemission Studies of Mixed-Valence, Reduced-Moment, and Antiferromagnetic Cerium Compounds, *Phys. Rev. Lett.* 46, 1100 (1981).
- [53] M. Croft, J. H. Weaver, D. J. Peterman, and A. Franciosi, Fundamental Parameters and Mechanisms in the Ce Problem: Photoemission Results on CeAl₂ and CeAl₂ Alloys, *Phys. Rev. Lett.* 46, 1104 (1981).
- [54] A. P. Murani, S. J. Levett, and J. W. Taylor, Magnetic Form Factor of α -Ce: Towards Understanding the Magnetism of Cerium, *Phys. Rev. Lett.* 95, 256403 (2005).
- [55] Bruce J. Baer et. al., Phase diagram and equation of state of praseodymium at high pressures and temperatures, *Phys. Rev. B* 67, 134115 (2003).
- [56] I.-K. Jeong et al., Role of the Lattice in the $\alpha - \gamma$ Phase Transition of Ce: A High-Pressure Neutron and X-Ray Diffraction Study, *Phys. Rev. Lett.* 92, 105702 (2004).
- [57] M. Krisch et al., Phonons of the anomalous element cerium, *PNAS* 108 (23) 9342 (2011).

- [58] Antonangeli D, et al., Kinetics of the isostructural $\alpha - \gamma$ transition in cerium investigated by ultrasonics, High Press Res. 30, 151 (2010).
- [59] S. Capponi and F. F. Assaad, Spin and charge dynamics of the ferromagnetic and antiferromagnetic two-dimensional half-filled Kondo lattice model, Phys. Rev. B 63, 155114 (2001).
- [60] Alexander Altland and Ben Simons, Condensed Matter Field Theory. Chapter 4.
- [61] Naomichi Hatano and Masuo Suzuki, Finding Exponential Product Formulas of Higher Orders.
- [62] Matthias Troyer, Uwe-Jens Wiese, Computational Complexity and Fundamental Limitations to Fermionic Quantum Monte Carlo Simulations, Phys. Rev. Lett. 94, 170201(2005).
- [63] J. C. Lashley et al., Tricritical Phenomena at the $\alpha - \gamma$ Transition in Ce_{0.9-x}La_xTh_{0.1} Alloys, PRL 97, 235701 (2006)
- [64] A.C. Hewson, *The Kondo Problem to Heavy Fermions*, Cambridge University Press, New York, N.Y., (1993).
- [65] M. Jarrell, H. Akhlaghpour, and T. Pruschke, Periodic Anderson model in infinite dimensions, Phys. Rev. Lett. **70**, 1670 (1993).
- [66] Zsolt Gulácsi and Dieter Vollhardt, Exact Insulating and Conducting Ground States of a Periodic Anderson Model in Three Dimensions, Phys. Rev. Lett. **91**, 186401 (2003).
- [67] M. Lavagna, C. Lacroix and M. Cyrot, Volume collapse in the Kondo lattice, Phys. Lett. **90A**, 210 (1982).
- [68] J. W. Allen and L. Z. Liu, $\alpha - \gamma$ transition in Ce. II. A detailed analysis of the Kondo volume-collapse model, Phys. Rev. B **46**, 5047 (1992).
- [69] K. Held, C. Huscroft, R. T. Scalettar, and A. K. McMahan, Similarities between the Hubbard and Periodic Anderson Models at Finite Temperatures, Phys. Rev. Lett. **85**, 373 (2000).
- [70] C. Huscroft, A.K. McMahan, and R.T. Scalettar, Magnetic and Thermodynamic Properties of the Three-Dimensional Periodic Anderson Hamiltonian, Phys. Rev. Lett. **82**, 2342 (1999).
- [71] L. de' Medici, A. Georges, G. Kotliar, and S. Biermann, Mott Transition and Kondo Screening in f-Electron Metals, Phys. Rev. Lett. **95**, 066402 (2005).

- [72] M. E. Manley et al., No role for phonon entropy in the fcc→fcc volume collapse transition in Ce_{0.9}Th_{0.1} at ambient pressure, Phys. Rev. B **67**, 014103 (2003).
- [73] F. Decremps, D. Antonangeli, B. Amadon and G. Schmerber, Role of the lattice in the two-step evolution of gamma-cerium under pressure, Phys. Rev. B **80**, 132103 (2009).
- [74] B. Johansson, A.V. Ruban, I.A. Abrikosov, Comment on “Thermal Signatures of the Kondo Volume Collapse in Cerium”, Phys. Rev. Lett. **102**, 189601 (2009).
- [75] K. Mitsumoto, Y. Ōno, Phonon softening and double-well potential formation due to electron–phonon interaction in heavy-fermion systems, Physica C **426**, 330 (2005).
- [76] Takashi Hotta, Enhanced Kondo Effect in an Electron System Dynamically Coupled with Local Optical Phonon, J. Phys. Soc. Jpn. **76**, 084702 (2007).
- [77] R. Nourafkan, and N. Nafari, Phase diagram of the Holstein-Kondo lattice model at half filling, Phys. Rev. B. **79**, 075122 (2009).
- [78] M. Raczkowski, P. Zhang, F. F. Assaad, T. Pruschke, M. Jarrell, Phonons and the coherence scale of models of heavy fermions, Phys. Rev. B **81**, 054444 (2010).
- [79] O. Bodensiek, *et al.*, Low-energy properties of the Kondo lattice model, J. Phys.: Condens. Matter **23**, 094212 (2011).
- [80] T. Holstein, Studies of polaron motion: Part I. The molecular-crystal model , Ann. Phys. (N.Y.) **8**, 325; Studies of polaron motion: Part II. The “small” polaron , **8**, 343 (1959).
- [81] J. K. Freericks, M. Jarrell, and D. J. Scalapino, Holstein model in infinite dimensions, Phys. Rev. B **48**, 6302 (1993).
- [82] A. Georges et al., Dynamical mean-field theory of strongly correlated fermion systems and the limit of infinite dimensions, Rev. Mod. Phys. **68**, 13 (1996).
- [83] D.W. Hess and J.W. Serene, Self consistent numerical calculations for nested fermi liquids, J. Phys. Chem. Solids **52**, 1385 (1991).
- [84] A. Deppeler and A.J. Millis, Electron-phonon interactions in correlated systems: Adiabatic expansion of the dynamical mean-field theory, Phys. Rev. B **65**, 100301 (2002); Dynamical mean-field theory of electron-phonon interactions in correlated systems: Application to isotope effects on electronic properties, **65**, 224301 (2002); Philipp Werner and A.J. Millis, Efficient Dynamical Mean Field Simulation of the Holstein-Hubbard Model, Phys. Rev. Lett. **99**, 146404 (2007).

- [85] W. Koller, D. Meyer, Y. Ōno, and A.C. Hewson, First- and second-order phase transitions in the Holstein-Hubbard model, *Europhys. Lett.* **66**, 559 (2004); W. Koller, A.C. Hewson, and D. M. Edwards, Polaronic Quasiparticles in a Strongly Correlated Electron Band, *Phys. Rev. Lett.* **95**, 256401 (2005).
- [86] M. Capone, G. Sangiovanni, C. Castellani, C. Di Castro, and M. Grilli, Phase Separation Close to the Density-Driven Mott Transition in the Hubbard-Holstein Model, *Phys. Rev. Lett.* **92**, 106401 (2004); M. Capone, P. Carta, S. Ciuchi, Dynamical mean field theory of polarons and bipolarons in the half-filled Holstein model, *Phys. Rev. B* **74**, 045106 (2006).
- [87] See, e.g., I. Loa, *et al.*, Lattice Dynamics and Superconductivity in Cerium at High Pressure, *Phys. Rev. Lett.* **108**, 045502 (2012).
- [88] R. R. dos Santos. Introduction to quantum Monte Carlo simulations for fermionic systems. *Brazilian Journal of Physics*, 33:36 – 54, 03 2003.
- [89] H.-B. Shüttler and D.J. Scalapino, Monte Carlo Studies of the Dynamics of Quantum Many-Body Systems, *Phys. Rev. Lett.* **55**, 1204 (1985); Monte Carlo studies of the dynamical response of quantum many-body systems, *Phys. Rev. B* **34**, 4744 (1986).
- [90] H.J. Vidberg and J.W. Serene, Solving the Eliashberg equations by means of N -point Padé approximants, *J. Low Temp. Phys.* **29**, 179 (1977).
- [91] Mark Jarrell and J. E. Gubernatis, Bayesian inference and the analytic continuation of imaginary-time quantum Monte Carlo data, *Physics Reports* **269**, 133-195 (1996).
- [92] J. Skilling and R.K. Bryan, Maximum entropy image reconstruction: general algorithm, *Mon. Not. R. astr. Soc.* **211**, 111 (1984).
- [93] S.F. Gull and G.J. Daniels, Image reconstruction from incomplete and noisy data, *Nature*, **272**, 686 (1978).
- [94] S.F. Gull, in *Maximum Entropy and Bayesian Methods*, edited by J. Skilling (Kluwer, Dordrecht, 1989), p. 53.
- [95] R.K. Bryan, Maximum entropy analysis of oversampled data problems, *Eur. Biophys. J.* **18**, 165 (1990).
- [96] A. W. Sandvik, Stochastic method for analytic continuation of quantum Monte Carlo data, *Phys. Rev. B* **57**, 10287 (1998).

Appendix A

Weak coupling expansion CTQMC

A.1 Partition function

The partition function of a general Hamiltonian is

$$Z = \text{Tr} T e^{-S} \quad (\text{A.1})$$

where S is the action

$$S = \int \int t_r^{r'} c_{r'}^\dagger c^r dr dr' + \int \int \int \int w_{r_1 r_2}^{r'_1 r'_2} c_{r_1}^\dagger c^{r_1} c_{r_2}^\dagger c^{r_2} dr_1 dr'_1 dr_2 dr'_2 \quad (\text{A.2})$$

Here T is the time-ordering and $r = \{\tau, \sigma, i\}$ denotes the combination of imaginary time τ , spin σ , and space coordination i . The integration

$$\int dr = \sum_i \sum_\sigma \int_0^\beta d\tau$$

The action can be separated into the non-interacting part S_0 and the interacting part W ,

$$\begin{aligned} S &= S_0 + W \\ S_0 &= \int \int t_r^{r'} c_{r'}^\dagger c^r dr dr' \\ W &= \int \int \int \int w_{r_1 r_2}^{r'_1 r'_2} c_{r_1}^\dagger c^{r_1} c_{r_2}^\dagger c^{r_2} dr_1 dr'_1 dr_2 dr'_2 \end{aligned} \quad (\text{A.3})$$

Then in the interaction representation, the perturbation expansion of partition function Z with respect to the non-interaction part S_0 lead to

$$\begin{aligned} Z &= \sum_{k=1}^{\infty} Z_k \\ &= \sum_{k=1}^{\infty} \int dr_1 \int dr'_1 \cdots \int dr_{2k} \int dr'_{2k} \Omega_k(r_1, r'_1, \cdots, r_{2k}, r'_{2k}) \end{aligned} \quad (\text{A.4})$$

where

$$\Omega_k = Z_0 \frac{(-1)^k}{k!} w_{r_1 r_2}^{r'_1 r'_2} \cdots w_{r_{2k-1} r_{2k}}^{r'_{2k-1} r'_{2k}} D_{r'_1 r'_2 \cdots r'_{2k}}^{r_1 r_2 \cdots r_{2k}}$$

$$Z_0 = TrTe^{-s_0}$$

$$D_{r'_1 r'_2 \dots r'_{2k}}^{r_1 r_2 \dots r_{2k}} = \langle T c_{r_1}^\dagger c^{r_1} \dots c_{r_{2k}}^\dagger c^{r_{2k}} \rangle = \det \|g_{r_j}^{0r_i}\|,$$

$$i, j = 1, \dots, 2k$$

Finally the partition function is written as

$$Z = \int D[k] \Omega_k$$

where $D[k]$ is the summation over all k and the integration over all possible r at every k .

A.2 Detailed balance

Considering a Markov chain in the K space, where each point on the Markov chain is a order k state in the perturbation expansion series of the partition function. So by randomly walking in the K space, all possible orders of perturbation expansion are visited. Regarding the weight Ω_k as the probability of order k should be visited in the chain, a Monte Carlo simulation can be employed to sample the partition function. In order to fulfill the detailed balance,

$$P_{k \rightarrow k'} D[k] \Omega_k = P_{k' \rightarrow k} D[k'] \Omega_{k'} \quad (\text{A.5})$$

We have

$$\frac{P_{k \rightarrow k'}}{P_{k' \rightarrow k}} = \frac{R_k p_{k \rightarrow k'}^{acc}}{R_{k'} p_{k' \rightarrow k}^{acc}} = \frac{D[k'] \Omega_{k'}}{D[k] \Omega_k} \quad (\text{A.6})$$

where R_k and $R_{k'}$ are the prior probabilities for propose such movements.

Considering the $k \leftrightarrow k+1$ movement,

(1) Add a Hubbard vertex. We have some freedom to choose the prior probability to add a vertex, here we can choose $P_{add} = 0.5$, consequently $P_{rem} = 1 - P_{add} = 0.5$; later we will discuss the choice auxiliary fields $S = \pm 1$, which gives out $P_s = 0.5$; the probability of inserting the vertex at some imaginary time τ in region $[0, \beta]$ is $P_+ = \frac{d\tau}{\beta}$. So we have

$$R_k = P_{add} \cdot P_s \cdot P_+ \quad (\text{A.7})$$

(2) Remove a Hubbard vertex. Among the $k+1$ vertex we need to choose one and remove it, the prior probability is $P_- = \frac{1}{k+1}$. So we have

$$R_{k+1} = P_{rem} \cdot P_- \quad (\text{A.8})$$

Insert eq. A.7, A.8 into eq. A.6, we arrive at

$$\frac{p_{k \rightarrow k+1}^{acc}}{p_{k+1 \rightarrow k}^{acc}} = \frac{P_{rem} \cdot P_- \cdot D[k+1] \Omega_{k+1}}{P_{add} \cdot P_s \cdot P_+ \cdot D[k] \Omega_k} \quad (\text{A.9})$$

here remember in configuration $D[k+1]$ there will be one extra $d\tau$ compared with $D[k]$, which will cancel with the $d\tau$ of P_+ in the denominator.

Using the Matropolis algorithm, the acceptance probability to add or remove a vertex is

$$\min[1, \frac{p_{k \rightarrow k \pm 1}^{acc}}{p_{k \pm 1 \rightarrow k}^{acc}}]$$

A.3 Determinant ratios and fast update

In order to calculate the acceptance probability in eq. A.9, we need to calculate the ratio

$$\frac{\Omega_{k+1}}{\Omega_k} = (-1) w_{r'_{2k+1} r'_{2k+2}}^{r'_{2k+1} r'_{2k+2}} \frac{D_{r'_1 r'_2 \dots r'_{2k+2}}^{r_1 r_2 \dots r_{2k+2}}}{D_{r'_1 r'_2 \dots r'_{2k}}^{r_1 r_2 \dots r_{2k}}} \quad (\text{A.10})$$

$$\begin{aligned} D_{r'_1 r'_2 \dots r'_{2k}}^{r_1 r_2 \dots r_{2k}} &= \det G_k \\ &= \det \begin{bmatrix} g_{1,1}^0 & \dots & g_{1,i}^0 & \dots & g_{1,k}^0 \\ \vdots & \ddots & \vdots & & \vdots \\ g_{i,1}^0 & \dots & g_{i,i}^0 & \dots & g_{i,k}^0 \\ \vdots & & \vdots & \ddots & \vdots \\ g_{k,1}^0 & \dots & g_{k,i}^0 & \dots & g_{k,k}^0 \end{bmatrix} \end{aligned} \quad (\text{A.11})$$

Here G_k is a k by k matrix whose elements are bare green's function $g_{r_j}^{0r_i}$ between vertex i and j and we define $M_k = G_k^{-1}$

A.3.1 the update in Markov chain between the k^{th} order and the $(k+1)^{th}$ order

It will be too expensive to calculate the determinant and elements of G_k or M_k every time. Noticed every update $k \leftrightarrow k+1$ we only change one row and one column of G_k or M_k , we can derive a fast update strategy instead of calculate the determinant of G . The direct determinant and matrix update calculation scales like k^3 while the fast update scales like k^2 .

$$\frac{\det G_{k+1}}{\det G_k} = \frac{\det M_k}{\det M_{k+1}} = \det[1 + \Delta M_k] = \lambda \quad (\text{A.12})$$

in which

$$\begin{aligned}\Delta &= G_{k+1} - G_k \\ &= \begin{bmatrix} 0 & \cdots & 0 & g_{1,k+1}^0 \\ \vdots & \ddots & \vdots & \vdots \\ 0 & \cdots & 0 & g_{k,k+1}^0 \\ g_{k+1,1}^0 & \cdots & g_{k+1,1}^0 & g_{k+1,k+1}^0 - 1 \end{bmatrix}\end{aligned}\quad (\text{A.13})$$

In order to accomplish the calculation, the k^{th} order matrix is expanded to the $(k+1)^{th}$ order matrix by adding one row $g_{k+1,i}^0 = 0$, one column $g_{i,k+1}^0 = 0$, and one element $g_{k+1,k+1}^0 = 1$.

It can be easily got that

$$1 + \Delta M_k = \begin{bmatrix} 1 & \cdots & 0 & g_{1,k+1}^0 \\ \vdots & \ddots & \vdots & \vdots \\ 0 & \cdots & 1 & g_{k,k+1}^0 \\ g_{k+1,l}^0 M_{l,1} & \cdots & g_{k+1,l}^0 M_{l,k} & g_{k+1,k+1}^0 \end{bmatrix}$$

This matrix can be written as a 2×2 block matrix

$$1 + \Delta M_k = \begin{bmatrix} I & Q \\ R & S \end{bmatrix}$$

in which I is a $k \times k$ unit matrix, Q is a $1 \times k$ vector, R is a $k \times 1$ vector, and $S = g_{k+1,k+1}^0$.

Using the supermatrix algorithm, we have the relation

$$(1 + \Delta M_k)^{-1} = \begin{bmatrix} \tilde{P} & \tilde{Q} \\ \tilde{R} & \tilde{S} \end{bmatrix}\quad (\text{A.14})$$

in which

$$\tilde{S} = (S - [R][IQ])^{-1} = \lambda^{-1}$$

$$\tilde{Q} = -[IQ]\tilde{S} = -\lambda^{-1}g_{i,k+1}^0$$

$$\tilde{R} = -\tilde{S}[RI] = -\lambda^{-1}g_{k+1,l}^0 M_{l,i}$$

$$\tilde{P} = I + [IQ]\tilde{S}[RI] = \delta_{i,j} + \lambda^{-1}g_{i,k+1}^0g_{k+1,l}^0M_{l,j}$$

Insert eq. A.14 into relation

$$M_{k+1} = M_k(1 + \Delta M_k)^{-1}$$

we can have the $(k+1) \times (k+1)$ matrix M_{k+1}

$$M_{k+1} = \begin{bmatrix} \dots & -\lambda^{-1}M_{1,l}g_{l,k+1}^0 \\ \vdots & M'_{i,j} & \vdots & \vdots \\ \dots & \dots & -\lambda^{-1}g_{k+1,l}^0M_{l,k} & -\lambda^{-1}M_{k,l}g_{l,k+1}^0 \\ -\lambda^{-1}g_{k+1,l}^0M_{l,1} & \dots & \lambda^{-1} \end{bmatrix} \quad (\text{A.15})$$

in which

$$M'_{i,j} = M_{i,j}^k + \lambda^{-1}M_{i,l}g_{l,k+1}^0g_{k+1,s}^0M_{s,j} \quad (\text{A.16})$$

And we can easily have the ratio of two Green's function matrix

$$\begin{aligned} \frac{\det G_{k+1}}{\det G_k} &= \det[1 + \Delta M_k] = \lambda \\ &= \frac{g_{k+1,k+1}^0 - g_{k+1,l}^0M_{l,s}^kg_{s,k+1}^0}{1} \\ &= \frac{1}{M_{k+1,k+1}^{k+1}} \end{aligned} \quad (\text{A.17})$$

For the movement $k+1 \rightarrow k$, suppose we remove the vertex n . Accordingly we remove the n^{th} row and column in the matrix G^k and M^k . It can be easily seen that by doing an inverse process of adding a vertex, we can easily have

$$\frac{\det G_{k-1}}{\det G_k} = \frac{\det M_k}{\det M_{k-1}} = M_{n,n}^k \quad (\text{A.18})$$

and

$$M_{i,j}^{k-1} = M_{i,j}^k - \frac{M_{i,n}^k M_{n,j}^k}{M_{nn}^k} \quad (\text{A.19})$$

Here notice that n plays like the $k+1$ row and column as adding a vertex. $M_{i,n}^k$ is like the $k+1$ column, $M_{n,j}^k$ is like the $k+1$ row, and M_{nn}^k is λ^{-1} . The index i, j, l, s above all in range $[1, \dots, k]$.

A.3.2 the update between the k^{th} order and the $(k+2)^{th}$ order

Following the above calculation about the hopping between k and $k+1$, we have

$$\begin{aligned}
\frac{\det G_{k+2}}{\det G_k} &= \frac{\det M_k}{\det M_{k+2}} \\
&= \det[1 + \Delta M_k] \\
&= \lambda
\end{aligned} \tag{A.20}$$

in which

$$\begin{aligned}
\Delta &= G_{k+2} - G_k \\
&= \begin{bmatrix} 0 & \cdots & 0 & g_{1,k+1}^0 & g_{1,k+2}^0 \\ \vdots & \ddots & \vdots & \vdots & \vdots \\ 0 & \cdots & 0 & g_{k,k+1}^0 & g_{k,k+2}^0 \\ g_{k+1,1}^0 & \cdots & g_{k+1,k}^0 & g_{k+1,k+1}^0 & g_{k+1,k+2}^0 \\ g_{k+2,1}^0 & \cdots & g_{k+2,k}^0 & g_{k+2,k+1}^0 & g_{k+2,k+2}^0 \end{bmatrix}
\end{aligned}$$

so

$$\begin{aligned}
1 + \Delta M_k &= \begin{bmatrix} 1 & \cdots & 0 & g_{1,k+1}^0 & g_{1,k+2}^0 \\ \vdots & \ddots & \vdots & \vdots & \vdots \\ 0 & \cdots & 1 & g_{k,k+1}^0 & g_{k,k+2}^0 \\ g_{k+1,1}^0 M_{l,1} & \cdots & g_{k+1,l}^0 M_{l,k} & g_{k+1,k+1}^0 & g_{k+1,k+2}^0 \\ g_{k+2,1}^0 M_{l,1} & \cdots & g_{k+2,l}^0 M_{l,k} & g_{k+2,k+1}^0 & g_{k+2,k+2}^0 \end{bmatrix} \\
&= \begin{bmatrix} I & Q \\ R & S \end{bmatrix}
\end{aligned}$$

if we define

$$(1 + \Delta M_k)^{-1} = \begin{bmatrix} \tilde{P} & \tilde{Q} \\ \tilde{R} & \tilde{S} \end{bmatrix}$$

in which

$$\begin{aligned}
\tilde{S}_{q,q'} &= (S - [R][IQ])^{-1} \\
&= \begin{bmatrix} g_{k+1,k+1}^0 - g_{k+1,l}^0 M_{l,s} g_{s,k+1}^0 & g_{k+1,k+2}^0 - g_{k+1,l}^0 M_{l,s} g_{s,k+2}^0 \\ g_{k+2,k+1}^0 - g_{k+2,l}^0 M_{l,s} g_{s,k+1}^0 & g_{k+2,k+2}^0 - g_{k+2,l}^0 M_{l,s} g_{s,k+2}^0 \end{bmatrix}^{-1} \\
&= \lambda_{q,q'}^{-1}
\end{aligned}$$

$$\widetilde{Q_{i,q'}} = -[IQ]\widetilde{S} = -g_{i,q}^0 \lambda_{q,q'}^{-1}$$

$$\widetilde{R_{q,i}} = -\widetilde{S}[RI] = -\lambda_{q,q'}^{-1} g_{q,l}^0 M_{l,i}$$

$$\widetilde{P_{i,j}} = I + [IQ]\widetilde{S}[RI] = \delta_{i,j} + g_{i,q}^0 \lambda_{q,q'}^{-1} g_{q',l}^0 M_{l,j}$$

So

$$\begin{aligned} M_{k+2} &= M_k(1 + \Delta M_k)^{-1} \\ &= \begin{bmatrix} & \cdots & & -M_{1,l} g_{l,q}^0 \lambda_{q,k+1}^{-1} & -M_{1,l} g_{l,q}^0 \lambda_{q,k+2}^{-1} \\ \vdots & M'_{i,j} & \vdots & \vdots & \vdots \\ & \cdots & & -M_{k,l} g_{l,q}^0 \lambda_{q,k+1}^{-1} & -M_{k,l} g_{l,q}^0 \lambda_{q,k+2}^{-1} \\ -\lambda_{k+1,q}^{-1} g_{q,l}^0 M_{l,1} & \cdots & -\lambda_{k+1,q}^{-1} g_{q,l}^0 M_{l,k} & \lambda_{k+1,k+1}^{-1} & \lambda_{k+1,k+2}^{-1} \\ -\lambda_{k+2,q}^{-1} g_{q,l}^0 M_{l,1} & \cdots & -\lambda_{k+2,q}^{-1} g_{q,l}^0 M_{l,k} & \lambda_{k+2,k+1}^{-1} & \lambda_{k+2,k+2}^{-1} \end{bmatrix} \end{aligned}$$

in which

$$M'_{i,j} = M_{i,j}^k + M_{i,l} g_{l,q}^0 \lambda_{q,q'}^{-1} g_{q',s}^0 M_{s,j} \quad (\text{A.21})$$

$$\frac{\det G_{k+2}}{\det G_k} = \det[1 + \Delta M_k] = \det \lambda_{q,q'} \quad (\text{A.22})$$

The index i, j, l, s above all in range $[1, \dots, k]$ and q, q' in range $[k+1, k+2]$.
And it is easy to get the formularism of $k \rightarrow k-2$ update

$$\frac{\det G_{k-2}}{\det G_k} = \frac{\det M_k}{\det M_{k-2}} = \det \lambda_{q,q'} \quad (\text{A.23})$$

$$M_{i,j}^{k-2} = M_{i,j}^k - M_{i,q}^k \lambda_{q,q'}^{-1} M_{q',j}^k \quad (\text{A.24})$$

Notice in this vertex removing case

$$\lambda_{q,q'} = M_{q,q'}$$

in which q and q' are the two vertex index which are going to be removed.

A.4 Observables

A.4.1 Average order

The average order of perturbation series is

$$\begin{aligned}
\langle k \rangle &= \frac{Z_0}{Z} \sum_{k=0}^{\infty} \frac{(-1)^k}{k!} \int dr_1 \int dr'_1 \cdots \int dr_{2k} \int dr'_{2k} w_{r_1 r'_2}^{r'_1 r'_2} \cdots w_{r_{2k-1} r'_{2k}}^{r'_{2k-1} r'_{2k}} \langle T \cdot k \cdot c_{r_1'}^\dagger c^{r_1} \cdots c_{r_{2k}'}^\dagger c^{r_{2k}} \rangle \\
&= \frac{Z_0}{Z} \sum_{k=0}^{\infty} \frac{(-1)^{k-1}}{(k-1)!} \int dr_1 \int dr'_1 \cdots \int dr_{2k-2} \int dr'_{2k-2} w_{r_1 r'_2}^{r'_1 r'_2} \cdots w_{r_{2k-3} r'_{2k-2}}^{r'_{2k-3} r'_{2k-2}} \langle T c_{r_1'}^\dagger c^{r_1} \cdots c_{r_{2k-2}'}^\dagger c^{r_{2k-2}} \cdot [- \int H(\tau)] \rangle \\
&= - \langle \int_0^\beta d\tau H(\tau) \rangle
\end{aligned} \tag{A.25}$$

The average order is a finite value. Actually the distribution of perturbation order is a Gaussian like [29].

A.4.2 Single particle Green's function

The single particle Green's function in Rubtsov's definition is

$$\begin{aligned}
G(r, r') &= \langle T c_r^\dagger c^{r'} \rangle \\
&= \frac{Z_0}{Z} \sum_{k=0}^{\infty} \frac{(-1)^k}{k!} \int dr_1 \int dr'_1 \cdots \int dr_{2k} \int dr'_{2k} w_{r_1 r'_2}^{r'_1 r'_2} \cdots w_{r_{2k-1} r'_{2k}}^{r'_{2k-1} r'_{2k}} \langle T c_r^\dagger c^{r'} c_{r_1'}^\dagger c^{r_1} \cdots c_{r_{2k}'}^\dagger c^{r_{2k}} \rangle \\
&= \frac{Z_0}{Z} \sum_{k=0}^{\infty} \frac{(-1)^k}{k!} \int dr_1 \int dr'_1 \cdots \int dr_{2k} \int dr'_{2k} w_{r_1 r'_2}^{r'_1 r'_2} \cdots w_{r_{2k-1} r'_{2k}}^{r'_{2k-1} r'_{2k}} \frac{\langle T c_r^\dagger c^{r'} c_{r_1'}^\dagger c^{r_1} \cdots c_{r_{2k}'}^\dagger c^{r_{2k}} \rangle}{\langle T c_{r_1'}^\dagger c^{r_1} \cdots c_{r_{2k}'}^\dagger c^{r_{2k}} \rangle} \\
&\times \langle T c_{r_1'}^\dagger c^{r_1} \cdots c_{r_{2k}'}^\dagger c^{r_{2k}} \rangle
\end{aligned}$$

and following the algorithm of add one vertex in the fast update formula

$$\frac{\langle T c_r^\dagger c^{r'} c_{r_1'}^\dagger c^{r_1} \cdots c_{r_{2k}'}^\dagger c^{r_{2k}} \rangle}{\langle T c_{r_1'}^\dagger c^{r_1} \cdots c_{r_{2k}'}^\dagger c^{r_{2k}} \rangle} = \frac{\det D^{k+1}}{\det D^k} = g_{r, r'}^0 - g_{r, r_i}^0 M_{i, j} g_{r_j, r'}^0$$

one can get the single-particle Green's function

$$G(r, r') = g_{r, r'}^0 - g_{r, r_i}^0 M_{i, j} g_{r_j, r'}^0 \tag{A.26}$$

after Fourier transform the Green's function in Matsubara frequency is

$$g(\omega) = g^0(\omega) - g^0(\omega) \left[\frac{1}{\beta} \sum_{i, j} M_{i, j} e^{i\omega(\tau_i - \tau_j)} \right] g^0(\omega) \tag{A.27}$$

A.4.3 Two-particle Green's function

Pair susceptibility

The pair susceptibility is defined as

$$\begin{aligned}
\chi_{i,j}^p(\tau, \tau') &= - \langle \Delta_i(\tau) \Delta_j^\dagger(\tau') \rangle \\
&= - \langle T c_{i,\uparrow}(\tau) c_{i,\downarrow}(\tau) c_{j,\downarrow}^\dagger(\tau') c_{j,\uparrow}^\dagger(\tau') \rangle \\
&= \frac{Z_0}{Z} \sum_{k=0}^{\infty} \frac{(-U)^k}{k!} \int dr_1 \cdots \int dr_k \langle T c_{j,\uparrow}^\dagger(\tau') c_{i,\uparrow}(\tau) n_\uparrow(\tau_1) \cdots n_\uparrow(\tau_k) \rangle \\
&\times \langle T c_{j,\downarrow}^\dagger(\tau') c_{i,\downarrow}(\tau) n_\downarrow(\tau_1) \cdots n_\downarrow(\tau_k) \rangle \\
&= \langle g_{j,i}^\uparrow(\tau', \tau) \rangle \langle g_{j,i}^\downarrow(\tau', \tau) \rangle
\end{aligned} \tag{A.28}$$

Transverse spin susceptibility

$$\begin{aligned}
\chi_{i,j}^{s,+ -}(\tau, \tau') &= - \langle T c_{i,\uparrow}^\dagger(\tau) c_{i,\downarrow}(\tau) c_{j,\downarrow}^\dagger(\tau') c_{j,\uparrow}(\tau') \rangle \\
&= \langle g_{i,j}^\uparrow(\tau, \tau') \rangle \langle g_{j,i}^\downarrow(\tau', \tau) \rangle
\end{aligned} \tag{A.29}$$

The longitudinal spin susceptibility

$$\begin{aligned}
\chi_{i,j}^{s,z}(\tau, \tau') &= - \langle T (n_i^\uparrow(\tau) - n_i^\downarrow(\tau)) (n_j^\uparrow(\tau') - n_j^\downarrow(\tau')) \rangle \\
&= \sum_{\sigma} [- \langle T n_i^\sigma(\tau) n_j^\sigma(\tau') \rangle + \langle T n_i^\sigma(\tau) n_j^{-\sigma}(\tau') \rangle] \\
&= \sum_{\sigma} [- \langle g_{i,i}^\sigma(\tau, \tau) \rangle \langle g_{j,j}^\sigma(\tau', \tau') \rangle + \langle g_{i,j}^\sigma(\tau, \tau') \rangle \langle g_{j,i}^\sigma(\tau', \tau) \rangle \\
&+ \langle g_{i,i}^\sigma(\tau, \tau) \rangle \langle g_{j,j}^{-\sigma}(\tau', \tau') \rangle]
\end{aligned} \tag{A.30}$$

If the SU(2) symmetry of spins is preserved, we have

$$\langle g_{i,i}^\sigma(\tau, \tau) \rangle \langle g_{j,j}^\sigma(\tau', \tau') \rangle = \langle g_{i,i}^\sigma(\tau, \tau) \rangle \langle g_{j,j}^{-\sigma}(\tau', \tau') \rangle$$

and

$$\chi_{i,j}^{s,z}(\tau, \tau') = \sum_{\sigma} \langle g_{i,j}^\sigma(\tau, \tau') \rangle \langle g_{j,i}^\sigma(\tau', \tau) \rangle = 2 \chi_{i,j}^{s,+ -}(\tau, \tau') \tag{A.31}$$

Charge susceptibility

$$\begin{aligned}
\chi_{i,j}^c(\tau, \tau') &= - \langle T(n_i^\uparrow(\tau) + n_i^\downarrow(\tau))(n_j^\uparrow(\tau') + n_j^\downarrow(\tau')) \rangle + \langle T(n_i^\uparrow(\tau) + n_i^\downarrow(\tau)) \rangle \langle T(n_j^\uparrow(\tau') + n_j^\downarrow(\tau')) \rangle \\
&= - \sum_{\sigma} [\langle T n_i^{\sigma}(\tau) n_j^{\sigma}(\tau') \rangle + \langle T n_i^{\sigma}(\tau) n_j^{-\sigma}(\tau') \rangle] \\
&\quad + \langle g_{i,i}^{\uparrow}(\tau, \tau) + g_{i,i}^{\downarrow}(\tau, \tau) \rangle \langle g_{j,j}^{\uparrow}(\tau', \tau') + g_{j,j}^{\downarrow}(\tau', \tau') \rangle \\
&= - \sum_{\sigma} [\langle g_{i,j}^{\sigma}(\tau, \tau') \rangle \langle g_{j,i}^{\sigma}(\tau', \tau) \rangle + \langle g_{i,i}^{\sigma}(\tau, \tau) \rangle \langle g_{j,j}^{\sigma}(\tau', \tau') \rangle \\
&\quad + \langle g_{i,i}^{\sigma}(\tau, \tau) \rangle \langle g_{j,j}^{-\sigma}(\tau', \tau') \rangle] + \langle g_{i,i}^{\uparrow}(\tau, \tau) + g_{i,i}^{\downarrow}(\tau, \tau) \rangle \langle g_{j,j}^{\uparrow}(\tau', \tau') + g_{j,j}^{\downarrow}(\tau', \tau') \rangle \quad (\text{A.32})
\end{aligned}$$

A.5 Auxiliary fields

A.5.1 Minus sign and the auxiliary fields for Hubbard interaction

In order to eliminate the notorious minus sign problem, or at least suppress it in some models, we need to introduce auxiliary fields. For example for the Hubbard model in the particle-hole symmetric form, the interacting part of Hamiltonian is

$$U \sum_i (n_{i\uparrow} - \frac{1}{2})(n_{i\downarrow} - \frac{1}{2})$$

After introduction of auxiliary field $s = \pm 1$, the interacting part can be written as

$$\frac{U}{2} \sum_i \sum_{s=\pm 1} (n_{i,\uparrow} - \alpha_+(s))(n_{i,\downarrow} - \alpha_-(s)) \quad (\text{A.33})$$

up to a constant. And

$$\begin{aligned}
\alpha_{\sigma}(s) &= \frac{1}{2} + \sigma s \delta \\
\delta &= \frac{1}{2} + 0^+
\end{aligned} \quad (\text{A.34})$$

where σ is electron spin.

It was proved that by increasing δ the minus sign problem will be reduced to certain degree, with the price of increment of the average order and consequently the CPU time.

A.5.2 Update by flipping the auxiliary fields

Flip one auxiliary field Denote the configurations with electron spin σ before and after flipping one auxiliary field by k and k' respectively

$$\frac{\det G'_{\sigma}}{\det G_{\sigma}} = \frac{\det M_{\sigma}}{\det M'_{\sigma}} = \det(1 + \Delta M_{\sigma})$$

$$\Delta_\sigma = G'_\sigma - G_\sigma = \begin{bmatrix} 0 & \cdots & 0 & \cdots & 0 \\ \vdots & \ddots & & & \vdots \\ 0 & \cdots & \alpha_\sigma(-s) - \alpha_\sigma(s) & \cdots & 0 \\ \vdots & & & \ddots & \vdots \\ 0 & \cdots & 0 & \cdots & 0 \end{bmatrix}$$

$$(1 + \Delta M)_\sigma = \begin{bmatrix} 1 & \cdots & 0 & \cdots & 0 \\ \vdots & \ddots & & & \vdots \\ M_{n1}b & \cdots & 1 + M_{nn}b & \cdots & M_{nk}b \\ \vdots & & & \ddots & \vdots \\ 0 & \cdots & 0 & \cdots & 1 \end{bmatrix}$$

in which

$$b = \alpha_\sigma(-s) - \alpha_\sigma(s) \quad (\text{A.35})$$

$$\det(1 + \Delta M)_\sigma = 1 + M_{nn}b = \lambda_\sigma \quad (\text{A.36})$$

After a exchange of $k \leftrightarrow n$, using the block matrix inversion tricks, and then another exchange of $n \leftrightarrow k$, we get

$$(1 + \Delta M)_\sigma^{-1} = \begin{bmatrix} 1 & \cdots & 0 & \cdots & 0 \\ \vdots & \ddots & & & \vdots \\ -\lambda^{-1}M_{n1}b & \cdots & \lambda^{-1} & \cdots & -\lambda^{-1}M_{nk}b \\ \vdots & & & \ddots & \vdots \\ 0 & \cdots & 0 & \cdots & 1 \end{bmatrix}$$

and

$$M'_{i,j} = M_{i,j}^\sigma - b\lambda_\sigma^{-1}M_{i,n}^\sigma M_{n,j}^\sigma \quad (\text{A.37})$$

Blocked update In certain case, the QMC simulation can be trapped in metastable states. The updating/flipping of block of auxiliary fields may help to recover, or at least partly find back, ergodicity. Just like flipping of one auxiliary field, suppose flipping a block of fields $[s_1, \dots, s_N]$ for a configuration matrix with electron spin σ ,

$$\Delta_{i,j} = G'_{i,j} - G_{i,j} = \sum_{l=1}^N (\alpha_\sigma(-s_{b_l}) - \alpha_\sigma(s_{b_l})) \delta_{b_l,i} \delta_{i,j}$$

It is easy to get the relation

$$\begin{aligned}
M_{i,j} &= M'_{i,k}(\delta_{k,j} + \Delta_{k,s}M_{s,j}) \\
&= M'_{i,k}(\delta_{k,j} + \sum_{l=1}^N(\alpha_\sigma(-s_{b_l}) - \alpha_\sigma(s_{b_l}))\delta_{b_l,k}\delta_{k,s}M_{s,j}) \\
&= M'_{i,j} + \sum_{l=1}^N(\alpha_\sigma(-s_{b_l}) - \alpha_\sigma(s_{b_l}))M'_{i,k}\delta_{b_l,k}M_{k,j} \\
M'_{i,j} &= M_{i,j} - \sum_{l=1}^N(\alpha_\sigma(-s_{b_l}) - \alpha_\sigma(s_{b_l}))M'_{i,b_l}M_{b_l,j}
\end{aligned}$$

Noticed the $\delta_{b_l,k}$ in above formula, we multiply δ_{j,b_m} on right hand side

$$\begin{aligned}
M'_{i,b_m} &= M_{i,b_m} - \sum_{l=1}^N(\alpha_\sigma(-s_{b_l}) - \alpha_\sigma(s_{b_l}))M'_{i,b_l}M_{b_l,b_m} \\
M_{i,b_m} &= (\delta_{b_m,b_l} + \sum_{l=1}^N(\alpha_\sigma(-s_{b_l}) - \alpha_\sigma(s_{b_l}))M_{b_m,b_l})M'_{i,b_l} \\
M'_{i,b_l} &= M_{i,b_m}B_{b_m,b_l}^{-1}
\end{aligned}$$

Inset into formula above, we have

$$M'_{i,j} = M_{i,j} - \sum_{l=1}^N(\alpha_\sigma(-s_{b_l}) - \alpha_\sigma(s_{b_l}))M_{i,b_m}B_{b_m,b_l}^{-1}M_{b_l,j} \quad (\text{A.38})$$

in which

$$B_{b_m,b_l} = \delta_{b_m,b_l} + \sum_{l=1}^N(\alpha_\sigma(-s_{b_l}) - \alpha_\sigma(s_{b_l}))M_{b_m,b_l} \quad (\text{A.39})$$

is a square matrix in reduce dimension N .

The ratio of accept blocked auxiliary fields update is

$$\begin{aligned}
\frac{\det G'_\sigma}{\det G_\sigma} &= \frac{\det M_\sigma}{\det M'_\sigma} \\
&= \det(1 + \Delta M_\sigma) \\
&= \det(\delta_{i,j} + \sum_{l=1}^N (\alpha_\sigma(-s_{b_l}) - \alpha_\sigma(s_{b_l})) \delta_{b_l,i} M_{i,j})
\end{aligned}$$

It can be easily seen that after rotation of index like previous section, you can find that by using blocked matrix algorithm, it equals to the determinant of reduced matrix B .

$$\frac{\det G'_\delta}{\det G_\delta} = \det(B^\sigma) \quad (\text{A.40})$$

A.6 Retard interaction

A.6.1 Electron-phonon interaction

If the electron-phonon interaction is introduced in the model

$$H = -\sum_{i,j,\sigma} t_{i,j} c_{i,\sigma}^\dagger c_{j,\sigma} + \sum_{i,\sigma} [g X_i (n_{i,\sigma} - 1) + \frac{P_i^2}{2M} + \frac{k X_{2i}}{2}] \quad (\text{A.41})$$

in which $X = \sqrt{\frac{1}{2m\omega_0}}(a + a^\dagger)$.

so the Hamiltonian can be written as

$$H = -\sum_{i,j,\sigma} t_{i,j} c_{i,\sigma}^\dagger c_{j,\sigma} + \sqrt{\frac{1}{2m\omega}} \sum_{i,\sigma} g (a_i + a_i^\dagger) (n_{i,\sigma} - 1) + (a_i^\dagger a_i + \frac{1}{2}) \omega_0$$

Written the partition function in Grassmann number

$$Z = \int [da^\dagger da] \int [dc^\dagger dc] e^{-(S_e + S_{ep})}$$

$$S_e = \int_0^\beta d\tau \sum_{i,j,\sigma} c_{i,\sigma}^\dagger(\tau) (\delta_{i,j} \frac{\partial}{\partial \tau} - t_{i,j}) c_{j,\sigma}(\tau)$$

$$S_{ep} = \sum_i [\int_0^\beta d\tau a_i^\dagger(\tau) (\frac{\partial}{\partial \tau} - \omega_0) a_i(\tau) + \sqrt{\frac{1}{2m\omega_0}} g (a_i(\tau) + a_i^\dagger(\tau)) (\sum_\sigma n_{i,\sigma}(\tau) - 1)]$$

here in S_{ep} we omit a constant term.

After Fourier transformation of S_{ep} into the Matsubara frequency space

$$S_{ep} = \sum_{i,m} a_{i,m}^\dagger (i\Omega_m - \omega_0) a_{i,m} + \sum_i \sum_m \sqrt{\frac{1}{2m\omega_0}} g(a_{i,m} + a_{i,m}^\dagger) \sum_n \left(\sum_\sigma n_{i,\sigma,n} - 1 \right)$$

Using the Hubbard-Stratonovich transform to integrate out a, a^\dagger , we have

$$\begin{aligned} S_{ep} &= \frac{g^2}{2m\omega_0} \sum_{i,m,n} \left(\sum_\sigma n_{i,\sigma,n} - 1 \right) \frac{1}{i\Omega_m - \omega_0} \left(\sum_{\sigma'} n_{i,\sigma',n} - 1 \right) \\ &= \frac{g^2}{2m\omega_0} \sum_{i,m,n} \left(\sum_\sigma n_{i,\sigma,n} - 1 \right) \frac{1}{2} \left(\frac{1}{i\Omega_m - \omega_0} + \frac{1}{i\Omega_m - \omega_0} \right) \left(\sum_{\sigma'} n_{i,\sigma',n} - 1 \right) \\ &= \frac{g^2}{2m\omega_0} \sum_{i,m,n} \left(\sum_\sigma n_{i,\sigma,n} - 1 \right) \frac{1}{2} \left(\frac{1}{i\Omega_m - \omega_0} + \frac{1}{-i\Omega_m - \omega_0} \right) \left(\sum_{\sigma'} n_{i,\sigma',n} - 1 \right) \\ &= \frac{g^2}{2m\omega_0} \sum_{i,m,n} \left(\sum_\sigma n_{i,\sigma,n} - 1 \right) \frac{\omega_0}{\Omega_m^2 + \omega_0^2} \left(\sum_{\sigma'} n_{i,\sigma',n} - 1 \right) \end{aligned}$$

Fourier transform back to imaginary time space, we have

$$S_{ep} = \int_0^\beta d\tau \int_0^\beta d\tau' \sum_{i,j} \left(\sum_\sigma n_{i,\sigma}(\tau) - 1 \right) D_{i,j}^0(\tau, \tau') \left(\sum_{\sigma'} n_{j,\sigma'}(\tau') - 1 \right) \quad (\text{A.42})$$

where

$$D_{i,j}^0(\tau, \tau') = \delta_{i,j} \frac{g^2}{2k} \frac{\omega_0}{2(1 - e^{-\beta\omega_0})} (e^{-|\tau-\tau'|\omega_0} + e^{-(\beta-|\tau-\tau'|)\omega_0}) = P(\tau - \tau') \delta_{i,j} \frac{g^2}{2k} \quad (\text{A.43})$$

The $\delta_{i,j}$ comes from the fact that there is no dispersion relation in the Einstein phonon ω_0 we choose.

A.6.2 Phonon vertex update algorithm

Following the derivation of updating algorithm of Hubbard vertex, we consider the $k \leftrightarrow k+1$ movement on Markov chain of adding/removing a phonon vertex

(1) Add a phonon vertex. Suppose the prior probability to add a vertex is $P_{add} = 0.5$, consequently $P_{rem} = 1 - P_{add} = 0.5$; the probability of adding a phonon vertex is P_{ph} ; the probability of choosing an auxiliary fields $S = \pm 1$ is $P_s = 0.5$, just like the Hubbard vertex; different from the Hubbard interaction, the electronic spins of phonon mediated retard interaction has four configurations $\{\uparrow\uparrow, \uparrow\downarrow, \downarrow\uparrow, \downarrow\downarrow\}$ $P_\sigma = \frac{1}{4}$, in contrast with the single spin configuration $\{\uparrow\downarrow\}$ of the Hubbard model; the probability of inserting the vertex at

some imaginary time τ in region $[0, \beta]$ is $P_+ = \frac{d\tau}{\beta}$ and the probability of set τ' in region $[0, \beta]$ is chosen to be $P(\tau - \tau')$, which is the phonon propagator above; so

$$R_k = P_{add} \cdot P_{ph} \cdot P_{\sigma} \cdot P_s \cdot P_+ \cdot P(\tau - \tau') \quad (\text{A.44})$$

(2) Remove a phonon vertex. Among the $k+1$ vertex we need to choose one and remove it, the prior probability is $P_- = \frac{1}{k+1}$; $R_{rem} = P_{rem} \cdot P_-$. There is no difference between removing a Hubbard vertex and a Phonon vertex. So we have

$$R_{k+1} = P_{rem} \cdot P_- \quad (\text{A.45})$$

After insert eq. A.44 and A.45 to eq. A.6 we got

$$\frac{p_{k \rightarrow k+1}^{acc}}{p_{k+1 \rightarrow k}^{acc}} = \frac{P_{rem} \cdot P_- \cdot D[k+1] \Omega_{k+1}}{P_{add} \cdot P_{ph} \cdot P_{\sigma} \cdot P_s \cdot P_+ \cdot P(\tau - \tau') \cdot D[k] \cdot \Omega_k} \quad (\text{A.46})$$

here we need to notice that in Ω_{k+1} there is an extra $P(\tau - \tau')$ term relative to the Ω_k due to the added phonon vertex, which finally cancels the $P(\tau - \tau')$ in the denominator.

Using the Metropolis algorithm, the acceptance probability to add or remove a phonon vertex is

$$\min[1, \frac{p_{k \rightarrow k \pm 1}^{acc}}{p_{k \pm 1 \rightarrow k}^{acc}}]$$

A.6.3 Choice of auxiliary fields for electron-phonon interaction

In order to remove or quench the minus sign problem, for model with electron-phonon interaction, we can rewrite S_{ep} above into following form

$$\begin{aligned} S_{ep} &= -\frac{g^2}{4k} \int_0^\beta d\tau \int_0^\beta d\tau' \sum_i \sum_{\sigma, \sigma'} \sum_{s=\pm 1} (n_{i,\sigma}(\tau) - \alpha_+(s)) P(\tau, \tau') (n_{i,\sigma'}(\tau') - \alpha_+(s)) \\ \alpha_+(s) &= \frac{1}{2} + s\delta \\ \delta &= \frac{1}{2} + 0^+ \end{aligned} \quad (\text{A.47})$$

up to a constant.

Noticed for phonon mediated retard interaction, we always choose $\alpha_+(s)$ for both up and down electronic spins. So the formula of flipping auxiliary fields, either single or blocked update, should be adjusted accordingly if both Hubbard interaction and electron-phonon interaction are included.

Appendix B

Green's function

B.1 One-particle Green's function

Our definition of the one-particle Green's function is

$$G(\tau, \tau') = - \langle T c(\tau) c^\dagger(\tau') \rangle \quad (\text{B.1})$$

After Fourier transform, it can be written in the space of Matsubara frequency

$$G(\omega, \omega') = \int_0^\beta d\tau \int_0^\beta d\tau' G(\tau, \tau') e^{i(\omega\tau - \omega'\tau')}$$

If the time transitional invariance is enforced $\tilde{\tau} = \tau - \tau'$, above equation becomes

$$\begin{aligned} G(\omega, \omega') &= \int_0^\beta d(\tau - \tau') G(\tau - \tau') e^{i\omega(\tau - \tau')} \int_0^\beta d\tau' e^{i(\omega - \omega')\tau'} \\ &= G(\omega) \beta \delta(\omega - \omega') \end{aligned}$$

Apply this Fourier transform to

$$\begin{aligned} g(\omega) \beta \delta(\omega - \omega') &= g^0(\omega) \beta \delta(\omega - \omega') - \int_0^\beta d\tau \int_0^\beta d\tau' g^0(\tau - \tau_i) \sum_{i,j} M_{i,j} g^0(\tau_j - \tau') e^{i(\omega\tau - \omega'\tau')} \\ &= g^0(\omega) \beta \delta(\omega - \omega') \\ &\quad - \int_0^\beta d\tau g^0(\tau - \tau_i) e^{i\omega(\tau - \tau_i)} \sum_{i,j} M_{i,j} e^{i(\omega\tau_i - \omega'\tau_j)} \int_0^\beta d\tau' g^0(\tau_j - \tau') e^{i\omega'(\tau_j - \tau')} \\ &= g^0(\omega) \beta \delta(\omega - \omega') - g^0(\omega) \sum_{i,j} M_{i,j} e^{i(\omega\tau_i - \omega'\tau_j)} g^0(\omega') \end{aligned}$$

So when the time transitional invariance is enforced,

$$g(\omega) = g^0(\omega) - g^0(\omega) \left[\frac{1}{\beta} \sum_{i,j} M_{i,j} e^{i\omega(\tau_i - \tau_j)} \right] g^0(\omega) \quad (\text{B.2})$$

which has energy scale of $\frac{1}{E}$.

Otherwise the energy is not conserved $\omega \neq \omega'$

$$g(\omega, \omega') = g^0(\omega)\delta(\omega - \omega')\beta - g^0(\omega) \left[\sum_{i,j} e^{i\omega\tau_i} M_{i,j} e^{-i\omega'\tau_j} \right] g^0(\omega') \quad (\text{B.3})$$

which has energy scale of $\frac{1}{E^2}$.

in which the δ function comes from the fact that the energy in bare Green's function is conserved.

B.2 Two-particle Green's function

B.2.1 Definition

The definition of two-particle Green's function is

$$\chi^{ph}(\tau_1, \tau_2, \tau_3, \tau_4) = \langle T c(\tau_1) c^\dagger(\tau_2) c(\tau_4) c^\dagger(\tau_3) \rangle - \langle T c(\tau_1) c^\dagger(\tau_2) \rangle \langle c(\tau_4) c^\dagger(\tau_3) \rangle \quad (\text{B.4})$$

for the particle-hole channel, and

$$\chi^{pp}(\tau_1, \tau_2, \tau_3, \tau_4) = \langle T c(\tau_1) c(\tau_2) c^\dagger(\tau_4) c^\dagger(\tau_3) \rangle \quad (\text{B.5})$$

for the particle-particle channel.

The Fourier transform of two-particle Green's function is

$$\chi(\omega_1, \omega_2, \omega_3, \omega_4) = \int_0^\beta d\tau_1 \int_0^\beta d\tau_2 \int_0^\beta d\tau_3 \int_0^\beta d\tau_4 \chi(\tau_1, \tau_2, \tau_3, \tau_4) e^{i(\omega_1\tau_1 - \omega_2\tau_2 + \omega_3\tau_3 - \omega_4\tau_4)}$$

Suppose the time transitional invariance is enforced

$$\begin{aligned} \chi(\omega_1, \omega_2, \omega_3, \omega_4) &= \int_0^\beta d\tau_1 \int_0^\beta d\tau_2 \int_0^\beta d\tau_3 \int_0^\beta d\tau_4 \chi(\tau_1, \tau_2, \tau_3, \tau_4) \\ &\times e^{i\omega_1(\tau_1 - \tau_4) - i\omega_2(\tau_2 - \tau_4) + i\omega_3(\tau_3 - \tau_4)} e^{i(\omega_1 - \omega_2 + \omega_3 - \omega_4)\tau_4} \\ &= \int_0^\beta d\tau'_1 \int_0^\beta d\tau'_2 \int_0^\beta d\tau'_3 \chi(\tau'_1, \tau'_2, \tau'_3, 0) e^{i\omega_1\tau'_1 - i\omega_2\tau'_2 + i\omega_3\tau'_3} \delta_{\omega_1 - \omega_2, \omega_4 - \omega_3} \\ &= \chi(\omega_1, \omega_2, \omega_3, \omega_4) \delta_{\omega_1 - \omega_2, \omega_4 - \omega_3} \end{aligned}$$

By introduction of bosonic frequency

$$\begin{aligned} \omega_1 - \omega_2 = \omega_4 - \omega_3 &= \nu \\ \omega_2 &= \omega \\ \omega_3 &= \omega' \end{aligned}$$

The two-particle Green's function can be written as

$$\chi(\omega_1, \omega_2, \omega_3, \omega_4) = \chi(\omega + \nu, \omega, \omega', \omega' + \nu) = \chi(\omega, \omega', \nu) \quad (\text{B.6})$$

in this ν, ω, ω' notation.

And easily can be seen from the Fourier transform that

$$\chi(\omega, \omega', \nu) = \chi^*(-\omega, -\omega', -\nu) \quad (\text{B.7})$$

which is in the energy scale of $\frac{1}{E^3}$.

The relationship between the two-particle Green's function in Matsubara frequency and imaginary time is

$$\begin{aligned} \chi(\tau) &= \chi(\tau, \tau, 0, 0) \\ &= \frac{1}{\beta^4} \sum_{\omega_1, \omega_2, \omega_3, \omega_4} \chi(\omega_1, \omega_2, \omega_3, \omega_4) e^{-i(\omega_1 - \omega_2)\tau} \\ &= \frac{1}{\beta^3} \sum_{\nu, \omega, \omega'} \chi(\omega, \omega', \nu) e^{-i\nu\tau} \\ &= \frac{1}{\beta} \sum_{\nu} \chi(\nu) \end{aligned} \quad (\text{B.8})$$

and inversely

$$\chi(\nu) = \int_0^\beta d\tau \chi(\tau) e^{i\nu\tau} = \frac{1}{\beta^2} \sum_{\omega, \omega'} \chi(\omega, \omega', \nu) \quad (\text{B.9})$$

B.2.2 Charge, spin, and pair susceptibilities

Particle-Hole channel The particle-hole channel of spin configuration $|\uparrow\uparrow; \uparrow\uparrow\rangle$ is defined as

$$\begin{aligned} \chi_{\uparrow\uparrow; \uparrow\uparrow}^{ph} &\equiv \langle T c_{1,\uparrow} c_{2,\uparrow}^\dagger c_{4,\uparrow} c_{3,\uparrow}^\dagger \rangle - \langle T c_{1,\uparrow} c_{2,\uparrow}^\dagger \rangle \langle c_{4,\uparrow} c_{3,\uparrow}^\dagger \rangle \\ &= - \langle g_{\uparrow\uparrow}^{1,3} g_{\uparrow\uparrow}^{4,2} \rangle_{QMC} + \langle g_{\uparrow\uparrow}^{1,2} g_{\uparrow\uparrow}^{4,3} \rangle_{QMC} - \langle g_{\uparrow\uparrow}^{1,2} \rangle_{QMC} \langle g_{\uparrow\uparrow}^{4,3} \rangle_{QMC} \end{aligned}$$

so we have

$$\begin{aligned}
\chi_{\uparrow\uparrow;\uparrow}^{ph}(Q)_{P,P'} &= -\langle g_{\uparrow}(P', P)g_{\uparrow}(P+Q, P'+Q) \rangle_{QMC} + \langle g_{\uparrow}(P+Q, P)g_{\uparrow}(P', P'+Q) \rangle_{QMC} \\
&\quad - \langle g_{\uparrow}(P+Q, P) \rangle_{QMC} \langle g_{\uparrow}(P', P'+Q) \rangle_{QMC} \quad (B.10) \\
&= -\frac{1}{2}(\langle g_{\uparrow}(P', P)g_{\uparrow}(P+Q, P'+Q) \rangle_{QMC} + \langle g_{\downarrow}(P', P)g_{\downarrow}(P+Q, P'+Q) \rangle_{QMC}) \\
&\quad + \frac{1}{2}(\langle g_{\uparrow}(P+Q, P)g_{\uparrow}(P', P'+Q) \rangle_{QMC} + \langle g_{\downarrow}(P+Q, P)g_{\downarrow}(P', P'+Q) \rangle_{QMC}) \\
&\quad - \frac{1}{4}(\langle g_{\uparrow}(P+Q, P) + g_{\downarrow}(P+Q, P) \rangle_{QMC} \langle g_{\uparrow}(P', P'+Q) + g_{\downarrow}(P', P'+Q) \rangle_{QMC})
\end{aligned}$$

The particle-hole channel of spin configuration $|\uparrow\uparrow; \downarrow\downarrow\rangle$ is defined as

$$\begin{aligned}
\chi_{\uparrow\uparrow;\downarrow\downarrow}^{ph} &\equiv \langle Tc_{1,\uparrow}c_{2,\uparrow}^{\dagger}c_{4,\downarrow}c_{3,\downarrow}^{\dagger} \rangle - \langle Tc_{1,\uparrow}c_{2,\uparrow}^{\dagger} \rangle \langle c_{4,\downarrow}c_{3,\downarrow}^{\dagger} \rangle \\
&= \langle g_{\uparrow\uparrow}^{1,2}g_{\downarrow\downarrow}^{4,3} \rangle_{QMC} - \langle g_{\uparrow\uparrow}^{1,2} \rangle_{QMC} \langle g_{\downarrow\downarrow}^{4,3} \rangle_{QMC}
\end{aligned}$$

so we have

$$\begin{aligned}
\chi_{\uparrow\uparrow;\downarrow\downarrow}^{ph}(Q)_{P,P'} &= \langle g_{\uparrow}(P+Q, P)g_{\downarrow}(P', P'+Q) \rangle_{QMC} - \langle g_{\uparrow}(P+Q, P) \rangle_{QMC} \langle g_{\downarrow}(P', P'+Q) \rangle_{QMC} \\
&= \frac{1}{2}(\langle g_{\uparrow}(P+Q, P)g_{\downarrow}(P', P'+Q) \rangle_{QMC} + \langle g_{\downarrow}(P+Q, P)g_{\uparrow}(P', P'+Q) \rangle_{QMC}) \quad (B.11) \\
&\quad - \frac{1}{4}(\langle g_{\uparrow}(P+Q, P) + g_{\downarrow}(P+Q, P) \rangle_{QMC} \langle g_{\uparrow}(P', P'+Q) + g_{\downarrow}(P', P'+Q) \rangle_{QMC})
\end{aligned}$$

Noticed here the SU(2) symmetry is enforced.

So the charge susceptibility can be written as

$$\begin{aligned}
\chi^c(Q)_{P,P'} &= 2 * \left(\chi_{\uparrow\uparrow;\uparrow}^{ph}(Q)_{P,P'} + \chi_{\uparrow\uparrow;\downarrow\downarrow}^{ph}(Q)_{P,P'} \right) \quad (B.12) \\
&= -(\langle g_{\uparrow}(P', P)g_{\uparrow}(P+Q, P'+Q) \rangle_{QMC} + \langle g_{\downarrow}(P', P)g_{\downarrow}(P+Q, P'+Q) \rangle_{QMC}) \\
&\quad + \langle (g_{\uparrow}(P+Q, P) + g_{\downarrow}(P+Q, P)) (g_{\uparrow}(P', P'+Q) + g_{\downarrow}(P', P'+Q)) \rangle_{QMC} \\
&\quad - \langle (g_{\uparrow}(P+Q, P) + g_{\downarrow}(P+Q, P)) \rangle_{QMC} \langle (g_{\uparrow}(P', P'+Q) + g_{\downarrow}(P', P'+Q)) \rangle_{QMC}
\end{aligned}$$

The spin susceptibility is

$$\begin{aligned}
\chi^s(Q)_{P,P'} &= 2 * \left(\chi_{\uparrow\uparrow;\uparrow}^{ph}(Q)_{P,P'} - \chi_{\uparrow\uparrow;\downarrow\downarrow}^{ph}(Q)_{P,P'} \right) \quad (B.13) \\
&= -(\langle g_{\uparrow}(P', P)g_{\uparrow}(P+Q, P'+Q) \rangle_{QMC} + \langle g_{\downarrow}(P', P)g_{\downarrow}(P+Q, P'+Q) \rangle_{QMC}) \\
&\quad + \langle (g_{\uparrow}(P+Q, P) - g_{\downarrow}(P+Q, P)) (g_{\uparrow}(P', P'+Q) - g_{\downarrow}(P', P'+Q)) \rangle_{QMC}
\end{aligned}$$

Particle-particle channel The particle-particle susceptibility of spin configuration $|\uparrow\downarrow; \uparrow\downarrow\rangle$ is defined as

$$\chi_{\uparrow\downarrow; \uparrow\downarrow}^{pp} = \langle T c_{1,\uparrow} c_{2,\downarrow} c_{4,\downarrow}^\dagger c_{3,\uparrow}^\dagger \rangle = \langle g_{\uparrow}^{1,3} g_{\downarrow}^{2,4} \rangle_{QMC}$$

so we have

$$\begin{aligned} \chi_{\uparrow\downarrow; \uparrow\downarrow}^{pp}(Q)_{p,p'} &= \langle g_{\uparrow}^{1,3}(-P, -P') g_{\downarrow}^{2,4}(P+Q, P'+Q) \rangle_{QMC} \\ &= \frac{1}{2} (\langle g_{\uparrow}(-P, -P') g_{\downarrow}(P+Q, P'+Q) \rangle_{QMC} + \langle g_{\downarrow}(-P, -P') g_{\uparrow}(P+Q, P'+Q) \rangle_{QMC}) \end{aligned} \quad (B.14)$$

and the particle-particle susceptibility of spin configuration $|\uparrow\downarrow; \downarrow\uparrow\rangle$ is defined as

$$\begin{aligned} \chi_{\uparrow\downarrow; \downarrow\uparrow}^{pp} &= \langle T c_{1,\uparrow} c_{2,\downarrow} c_{4,\uparrow}^\dagger c_{3,\downarrow}^\dagger \rangle = - \langle g_{\uparrow}^{1,4} g_{\downarrow}^{2,3} \rangle_{QMC} \\ &= - \langle g_{\uparrow}^{1,4}(-P, -P') g_{\downarrow}^{2,3}(P+Q, P'+Q) \rangle_{QMC} \\ &= - \langle g_{\uparrow}^{1,3}(-P, P'+Q) g_{\downarrow}^{2,4}(P+Q, -P') \rangle_{QMC} \\ &= - \chi_{\uparrow\downarrow; \uparrow\downarrow}^{pp}(Q)_{p, -p'-Q} \end{aligned} \quad (B.15)$$

Here the crossing symmetry is used by exchange 3 and 4 legs. So for the particle-particle channel only the $\{\uparrow\downarrow; \uparrow\downarrow\}$ component is necessary to be calculated.

B.2.3 Bethe-Salpeter equation and bulk susceptibility

In the DMFT or its cluster extension simulation, only impurity or cluster quantities are calculated. But in order to describe the phase transition, bulk quantities are required. Just like for the single-particle level, the self-energy is the bridge between impurity and bulk Green's function

$$g_{0,i}^{-1}(i\omega_n) - G_i^{-1}(i\omega_n) = \Sigma(i\omega_n) = g_{0,l}^{-1}(i\omega_n) - G_l^{-1}(i\omega_n) \quad (B.16)$$

This is the Dyson's equation, i means impurity and l means the lattice.

Similarly on the two particle level, the irreducible vertex plays like the self-energy. The impurity and bulk susceptibilities can be connected by the Bethe-Salpeter equation.

$$\chi_{0,i}^{-1}(Q)_{p,p'} - \chi_i^{-1}(Q)_{p,p'} = \Gamma(Q)_{p,p'} = \chi_{0,l}^{-1}(Q)_{p,p'} - \chi_l^{-1}(Q)_{p,p'} \quad (B.17)$$

One should notice the susceptibility χ is a matrix at Q whose elements are indexed by p and p' . So the solve of Bethe-Salpeter equation involves inversion of matrix, not like in the Dyson's equation only inversion of a scalar is enough.

Particle-Hole channel The Bethe-Salpter equation is written as

$$\chi^{ph}(Q)_{p,p'} = \chi_0^{ph}(Q)_{p,p'} - \frac{1}{(\beta N)^2} \sum_{p'',p'''} \chi^{ph}(Q)_{p,p''} \Gamma^{ph}(Q)_{p'',p'''} \chi_0^{ph}(Q)_{p''',p'} \quad (\text{B.18})$$

From the definition, the bare susceptibility is

$$\chi_0^{ph}(Q)_{p,p'} \equiv -\beta N * G(p)G(p+Q)\delta_{p,p'} \quad (\text{B.19})$$

For the Hubbard interaction $Un_{i,\uparrow}n_{i,\downarrow}$, consider the first order expansion of the two-particle in particle-hole channel,

Particle-Particle channel The Bethe-Salpter equation is written as

$$\chi^{pp}(Q)_{p,p'} = \chi_0^{pp}(Q)_{p,p'} - \frac{1}{(\beta N)^2} \sum_{p'',p'''} \chi^{pp}(Q)_{p,p''} \Gamma^{pp}(Q)_{p'',p'''} \chi_0^{pp}(Q)_{p''',p'} \quad (\text{B.20})$$

From the definition, the bare susceptibility is

$$\chi_0^{pp}(Q)_{p,p'} \equiv \beta N * G(-p)G(p+Q)\delta_{p,p'} \quad (\text{B.21})$$

Appendix C

Numerical tricks

C.1 Fourier transform

After a partial integration of the Fourier transform formula

$$\begin{aligned}
G(i\omega_n) &= \int_0^\beta d\tau G(\tau) e^{i\omega_n \tau} \\
&= \frac{G(0) + G(\beta)}{-i\omega_n} + \frac{G'(0) + G'(\beta)}{(-i\omega_n)^2} + \frac{G''(0) + G''(\beta)}{(-i\omega_n)^3} \\
&\quad + \dots \\
&\quad + \frac{1}{(-i\omega_n)^k} \int_0^\beta d\tau G^k(\tau) e^{i\omega_n \tau}
\end{aligned} \tag{C.1}$$

By comparing this formula with the high frequency expansion of the Green's function in Matsubara frequency

$$G(i\omega_n) = a_0 + \frac{a_1}{i\omega_n} + \frac{a_2}{(i\omega_n)^2} + \frac{a_3}{(i\omega_n)^3} + \dots \tag{C.2}$$

it is easy to have

$$\begin{aligned}
a_0 &= 0 \\
a_1 &= -(G(0) + G(\beta)) \\
a_2 &= G'(0) + G'(\beta) \\
a_3 &= -(G''(0) + G''(\beta))
\end{aligned} \tag{C.3}$$

C.2 Inverse Fourier transform

Since the leading order of single-particle Green's function behave like $\sim \frac{1}{i\omega_n}$, the inverse Fourier transform

$$G(\tau) = \frac{1}{\beta} \sum_n G(i\omega_n) e^{-i\omega_n \tau} \quad (\text{C.4})$$

will diverge as the summation is scale as order of ω_n . In order to solve the problem, we can choose to subtract a function $f(i\omega_n)$ whose inverse Fourier transform is known; after the inverse Fourier transform of difference, the known function $f(\tau)$ is added.

$$G(\tau) = \frac{1}{\beta} \sum_n [G(i\omega_n) - f(i\omega_n)] e^{-i\omega_n \tau} + f(\tau) \quad (\text{C.5})$$

There are two choices of the known function $f(i\omega_n)$

- The bare Green's function. The known Green's function can be choose as the bare Green's function $g^0(i\omega_n)$, when its imaginary time counter part $g^0(\tau)$ is exact or known;
- As we discussed above, we can choose

$$f(i\omega_n) = \frac{a_1}{i\omega_n} + \frac{a_2}{(i\omega_n)^2} + \frac{a_3}{(i\omega_n)^3} \quad (\text{C.6})$$

It is easily proved that

$$f(\tau) = \frac{-a_1}{2} + \frac{a_2}{4}(-\beta + 2\tau) + \frac{a_3}{4}(\beta\tau - \tau^2) \quad (\text{C.7})$$

C.3 High frequency tails of self-energy

In quantum Monte Carlo simulation, the precision in measurement of Green's function and self-energy is limited by statistic error. The Green's function and self-energy decay fast to zero at high frequency, which makes the high frequency tails are often overwhelmed by the rather large error bar. But as we know the high frequency asymptotic behavior of the Green's function and self-energy, and luckily the low frequency part can be measured at relatively higher precision, we can keep the low frequency part from the QMC measurement, and retrieve the precision at high frequency at least to the first few orders by attaching the high frequency tails.

Here we use the self-energy of the single-band Hubbard model as an example. The high frequency part of the self-energy can be generally expanded as

$$\Sigma^h(i\omega_n) = a_0 + \frac{a_1}{i\omega_n} + \frac{a_2}{(i\omega_n)^2} + \dots \quad (\text{C.8})$$

For Hubbard model, the first two terms

$$a_0 = U(n - \frac{1}{2}) \quad (\text{C.9})$$

in which n is the filling of electrons and the part-hole symmetry form of Hubbard interaction is used. So the zero-th order term is a real;

$$a_1 = U^2 n(1 - n) \quad (\text{C.10})$$

So the first-order term is imaginary.

C.4 Inhomogeneous frequency grid

As we have seen in figure above, at high frequency the tail of either Green's function or self-energy decays asymptotically to zero. And usually for the low temperature energy scale we are interested in, the low frequency part provides the most information. So a strategy can be adopted, where in the low frequency part all Matsubara frequency grids are kept exactly, but at the high frequency part, less frequency grids are preserved. The higher the frequency is, the less the frequency grids are kept. Every frequency grid is connected with a weight W_i . By apply the inhomogeneous frequency grid strategy, the numerical cost for measurement of Green's function in frequency can be decimated due to the small inhomogeneous frequency grid used.

In the simulation I used the Gaussian summation strategy proposed by Hartmut Monien. By properly choice of ω_i and W_i , we can have

$$\sum_{n=-\infty}^{\infty} f(n) \approx \sum_{i=1}^N W_i f(\omega_i) \quad (\text{C.11})$$

If in certain case homogeneous frequency grid is needed, the inhomogeneous frequency grid function can be interpolated to homogeneous one by spline. For the Fourier transform, we can directly conduct the transform for the inhomogeneous frequency grid by including the weight, or first conduct the interpolation and then the transform. For Hubbard model, compared with the Green's function with 500 homogeneous frequency grids, the Green's function with 50 inhomogeneous frequency grid will have an error as large as 10^4 after the Fourier transform.

Appendix D

Minus sign problem

Although QMC is one of the most widely used numerical tools in the research of condensed matter physics, its application is often limited by the notorious minus sign problem, especially at the large interaction and large system size region. The existence of minus sign problem prevents the explore of physics problem where strong interaction is of importance, like the cuprate high temperature superconductor.

Typically the minus sign problems is encountered when there is interacting fermions or frustrated spins. In QMC, a D -dimensional quantum system is mapped onto a $D + 1$ -dimensional classical system where the extra dimension is the imaginary time. By doing a path integral of the partition function, every possible configuration is visited stochastically with the probability according to their weight.

$$\begin{aligned} Z &= \int D[c, c^\dagger] e^{-S[c, c^\dagger]} \\ &= \int D[c, c^\dagger] W[c, c^\dagger] \end{aligned} \quad (\text{D.1})$$

In which $\int D[c, c^\dagger]$ is the integration on all fermionic degree of freedom; $S[c, c^\dagger]$ is the action and $W[c, c^\dagger]$ is the weight of certain fermionic configuration $[c, c^\dagger]$. Such kind of importance sampling is the key that QMC works, since the exponential complexity of problem is simplified to polynomial complexity. Accordingly the expectation value an observable is measured by average on all possible configurations $[c, c^\dagger]$ with respect to their weights $W[c, c^\dagger]$

$$\langle A \rangle = \frac{\int D[c, c^\dagger] A W[c, c^\dagger]}{\int D[c, c^\dagger] W[c, c^\dagger]} \quad (\text{D.2})$$

In the large interaction or large system size direction, the weight $W[c, c^\dagger]$ of such fermionic system can be negative, which may come from odd times of permutation of fermions. Now the weight cannot be interpreted as probability anymore. In order to get around this problem, the minus sign is absorbed into the observable but keep the absolute value of the weight

$$\begin{aligned} \langle A \rangle &= \frac{\int D[c, c^\dagger] \cdot A \cdot \frac{W[c, c^\dagger]}{|W[c, c^\dagger]|} \cdot |W[c, c^\dagger|}{\int D[c, c^\dagger] \cdot \frac{W[c, c^\dagger]}{|W[c, c^\dagger]|} \cdot |W[c, c^\dagger|} \\ &= \frac{\int D[c, c^\dagger] \cdot A \cdot s[c, c^\dagger] \cdot |W[c, c^\dagger|}{\int D[c, c^\dagger] \cdot s[c, c^\dagger] \cdot |W[c, c^\dagger|} \end{aligned} \quad (\text{D.3})$$

in which $s[c, c^\dagger] = \frac{W[c, c^\dagger]}{|W[c, c^\dagger]|}$ is the sign of certain configuration $[c, c^\dagger]$. The expectation value of the observable can further be written as

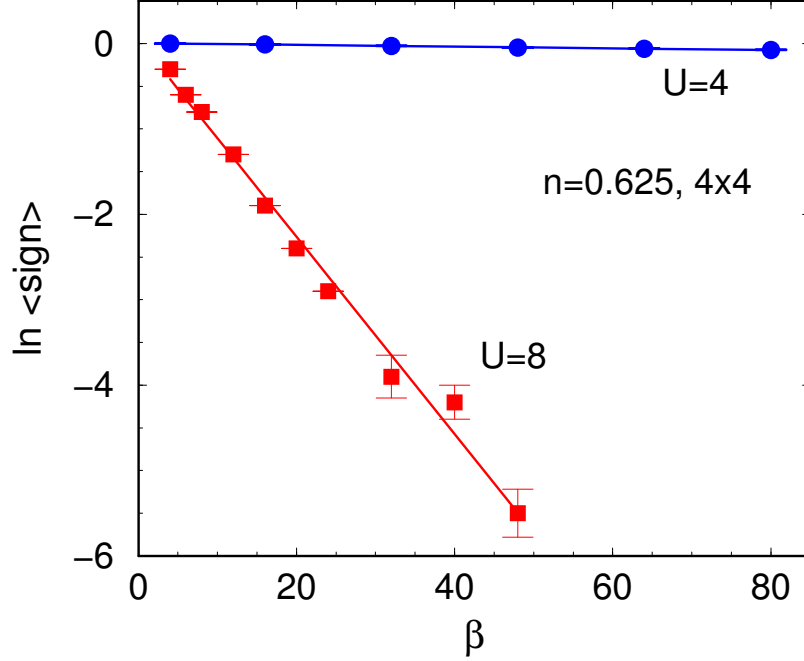


Figure D.1: (Color online) The minus sign as a function of system size (here the system size is only depend on the inversed temperature β) and interaction U . The average sign decreases exponentially as the temperature is decreased. At large interaction, the decreasing of average sign is much faster. The data is from Ref. [88].

$$\begin{aligned}
\langle A \rangle &= \frac{\int D[c, c^\dagger] \cdot A \cdot s[c, c^\dagger] \cdot |W[c, c^\dagger]| / \int D[c, c^\dagger] \cdot |W[c, c^\dagger]|}{\int D[c, c^\dagger] \cdot s[c, c^\dagger] \cdot |W[c, c^\dagger]| / \int D[c, c^\dagger] \cdot |W[c, c^\dagger]|} \\
&= \frac{\langle As \rangle}{\langle s \rangle}
\end{aligned} \tag{D.4}$$

Apparently this trick doesn't solve the minus sign problem. When there is minus sign, the sign $s[c, c^\dagger]$ will oscillate between ± 1 from one configuration to another, so the average sign $\langle s \rangle$ will be a value smaller than one. As the interaction or system size is large, the probability of positive sign will be close to the probability of negative sign. Consequently both the average sign $\langle s \rangle$ and the average observable $\langle As \rangle$ decrease exponentially to zero as a function of the increased system size and interaction as shown in Fig. D.1. Finally they are overwhelmed by the statistics error of QMC.

Appendix E

Analytic continuation

In the QMC simulation, the output Green's functions are generally either in imaginary time and Matsubara frequency. But the quantities from experiment measurement are mostly in real time and frequency. So it is necessary to convert the QMC outputs in imaginary time or frequency to quantities in real time or frequency. The formula to accomplish this transform is

$$G(i\omega_n) = \int d\omega \frac{A(\omega)}{i\omega_n - \omega} \quad (\text{E.1})$$

or equivalently

$$G(\tau) = \int d\omega \frac{A(\omega)e^{-\tau\omega}}{1 \pm e^{-\beta\omega}} \quad (\text{E.2})$$

where $A(\omega) = -\frac{1}{\pi} \text{Im}G(\omega)$ and on the right hand side of equation $+$ sign is for fermion and $-$ sign is for boson. Consider the vector and matrix representation of above formula

$$G(\tau_i) = K(\tau_i, \omega_j)A(\omega_j)$$

or

$$G(i\omega_n) = K(\omega_n, \omega_j)A(\omega_j)$$

where K is a two-dimensional matrix and G, A are vectors. The problem is turned into how to inverse the matrix K by given G . But we can see the inversion of K is rather hard. Even we write K as a square matrix, as ω gets large K will be a small value, which makes the determinant of K exponentially small. Furthermore, the statistical error of G will overwhelm the small value of K^{-1} , which makes infinite numbers of $A(\omega)$ all fit to one G .

E.1 Maximum Entropy Method

Historically, there are three attempts trying to attack this problem. The first is the so called least-squares fits proposed by Schuttler and Scalapino [89]. By minimizing the least-squares misfitting of the spectrum $A(\omega)$ and the QMC data G , the spectrum is approximated by a set of pixels. But as increasing the number of pixels in order to better resolve features of the spectrum, the output spectrum turns out to be unstable and noisy. The second try is the so called Pade method [90]. In this method, the Green's function G is fitted by the

ratio of two polynomials, which then be transformed to real frequency by a Wick rotation $i\omega_n \rightarrow \omega + 0^+$. This method works pretty nice when the Green's function is very precise, unfortunately the output from QMC has too large an error to be handled. As the most widely used analytic continuation method for QMC data, the Maximum Entropy Method (MEM) [91] is an attempt based on Bayesian statistics.

E.1.1 Bayesian statistics

According to Bayesian theorem, the probability to have two events a and b is

$$P(a, b) = P(a|b)P(b) = P(b|a)P(a) \quad (\text{E.3})$$

where $P(a|b)$ is the conditional probability of event a given event b. And we have normalization of probability

$$\int da P(a) = 1 \quad (\text{E.4})$$

and

$$P(a) = \int db P(a, b) \quad (\text{E.5})$$

Accordingly for our problem of analytic continuation of QMC data, the probability to find a spectrum A at given G is

$$P(A|G) = P(G|A)P(A)/P(G) \quad (\text{E.6})$$

Here we define $P(G|A)$ as the likelihood function and $P(A)$ as the prior probability of A . Naturally, we define the prior probability of G , $P(G)$ as a constant.

E.1.2 Prior Probability

In order to interpret the spectrum as probability density, we should construct spectra as positive-definite functions. For Fermions the spectra is always positive definite. But for Boson the situation is a little more complicated. As we know that $-\frac{1}{\pi}G^{boson}(\omega)$ is an odd function. So it is more convenient to define $A(\omega) = -\frac{1}{\pi\omega}ImG(\omega) \geq 0$ for Bosons. And the canonical transform becomes

$$G(\tau) = \int d\omega \frac{\omega [e^{-\tau\omega} + e^{-(\beta-\tau)\omega}]}{1 - e^{-\beta\omega}} A(\omega) \quad (\text{E.7})$$

The advantage of this convention is that it guarantee the symmetry of Bosonic Green's function that $G(\tau) = G(\beta - \tau)$ and of the spectrum $A(\omega) = A(-\omega)$. And noticed that $A(\omega)$ is not singular at $\omega = 0$.

For other more complicated spectra, like the spectrum of off-diagonal elements of Nambu's Green's function G_{12} , a positive constant c can be added to its spectrum $A_{12}(\omega) = -\frac{1}{\pi} \text{Im} G_{12}(\omega)$. The canonical transform becomes

$$\begin{aligned} \int d\omega K(\tau, \omega) A(\omega) &= \int d\omega K(\tau, \omega) [A_{12}(\omega) + c] \\ &= G_{12}(\tau) + c \int d\omega K(\tau, \omega) = G(\tau) \end{aligned} \quad (\text{E.8})$$

The symmetry of spectrum $A_{12}(\omega) = -A_{12}(-\omega)$ and the data $G_{12}(\tau) = -G_{12}(\beta - \tau)$ is enforced by the kernel

$$K(\tau, \omega) = \frac{e^{-\tau\omega} - e^{-(\beta-\tau)\omega}}{1 + e^{-\beta\omega}} \quad (\text{E.9})$$

The prior probability is defined as proportional to $e^{\alpha S}$ where S is the information entropy defined as

$$S = \int d\omega [A(\omega) - m(\omega) - A(\omega) \ln(A(\omega)/m(\omega))] \quad (\text{E.10})$$

where $m(\omega)$ is some positive-definite function and later we will define it as default model. α is an unknown parameter yet.

E.1.3 Likelihood function

Following the central limit theorem, the likelihood function is defined as

$$P(G|A) = e^{-\chi^2/2} \quad (\text{E.11})$$

in which

$$\chi^2 = \sum_{i=1}^L \left(\frac{G_i - \sum_j K_{i,j} A_j}{\sigma_i} \right)^2 \quad (\text{E.12})$$

where σ_i^2 are the diagonal elements of the covariance matrix

$$C_{i,j} = \frac{1}{N(N-1)} \sum_{l=1}^N (G_i^l - \langle G_i \rangle) (G_j^l - \langle G_j \rangle) \quad (\text{E.13})$$

where N is the number of bins from the QMC measurement; i and j are index of time slices.

In order to reduce the correlations between adjacent measurement, rebin might be needed to guarantee that the distribution of Green's function at certain time τ is Gaussian. If the skewness and kurtosis of QMC data at certain time τ_i is lower than certain given criteria, then the set of data at this time should be abandoned.

And the covariance matrix should be diagonalized to further decrease the correlation of QMC data.

$$U^{-1}CU = \sigma_i^2 \delta_{i,j} \quad (\text{E.14})$$

And both the kernel and QMC data should be rotated as well

$$K' = U^{-1}K \quad (\text{E.15})$$

and

$$G' = U^{-1}G \quad (\text{E.16})$$

Therefore the misfit function becomes

$$\chi^2 = \sum_{i=1}^L \left(\frac{G'_i - \sum_j K'_{i,j} A_j}{\sigma_i} \right)^2 \quad (\text{E.17})$$

It should be emphasized that the number of QMC bins should be at least two time larger than the number of time slices used in the likelihood function $N > 2 * L$, otherwise the diagonalization of covariance matrix cannot give out meaningful results.

Finally we have the probability function of spectrum

$$P(A|G, m, \alpha) \propto P(G|A, m, \alpha)P(A|m, \alpha) = \frac{e^{(\alpha S - \chi^2/2)}}{Z_S Z_L} \quad (\text{E.18})$$

where Z_L and Z_S are normalization factors.

$$Z_S = \int \frac{d^N A}{\prod_i \sqrt{A_i}} e^{\left\{ -\alpha \sum_i (A_i \ln A_i / m_i - A_i + m_i) \right\}} \quad (\text{E.19})$$

and

$$Z_L = \int d^L G e^{-\frac{1}{2} \sum_{i=1}^L \left(\frac{G'_i - \sum_j K'_{i,j} A_j}{\sigma_i} \right)^2} \quad (\text{E.20})$$

E.1.4 Choices of α

There is one external parameter α need to be fixed. Apparently when α is small, the contribution from entropy S is quenched, the trial spectra will be dominated by the statistic error from QMC measurement; while when α is large, the entropy term will be dominant and the input G becomes useless. Therefore a proper choice of α is very important for the spectrum result. There are three ways to fix the α .

- **Historic MEM** [92, 93] In the historic MEM method, the criteria to choose α is $\chi^2 = L$. The argument to have this criteria is that suppose the spectrum is already known, the different bins of data from QMC will lead to $\chi^2 = L$ misfit after average. But unfortunately such choice of α tends to under fit the data.
- **Classic MEM** [94] Another method to choose α is by maximizing it probability

$$\frac{\partial P(\alpha|G, m)}{\partial \alpha} = 0 \quad (\text{E.21})$$

in which

$$P(\alpha|G, m) = \int \frac{d^N A}{\prod_i \sqrt{A_i}} P(\alpha, A|G, m) \quad (\text{E.22})$$

and

$$P(\alpha, A|G, m) = P(A|G, m, \alpha)P(\alpha) \propto \frac{e^{(\alpha S - \chi^2/2)}}{Z_S Z_L} P(\alpha) \quad (\text{E.23})$$

It is argued [6] that the prior probability of α here is $P(\alpha) = \frac{1}{\alpha}$.

- **Bryan's method** [95] Typically, the probability distribution of α is broad and highly skewed, which means it is not proper to use the maximized probability

$$\frac{\partial P(\alpha|G, m)}{\partial \alpha} = 0 \quad (\text{E.24})$$

to represent the mean value of $P(\alpha|G, m)$. A natural choice is average all spectra according to their probability distribution

$$\bar{A} = \int d\alpha A(\alpha) P(\alpha|G, m) \quad (\text{E.25})$$

If the QMC data is good enough, which means they are very precise and not correlated, three methods should give out same spectrum principally. But if the QMC data are less precise and have some correlation, usually Bryan's method gives the best output.

E.1.5 Annealing Method

In practice, so as to acquire high quality spectrum from MEM, usually it is necessary to the annealing method. In the annealing method, after a series of QMC data are generated, we start the MEM at the highest temperature; every time the output spectrum of high temperature is used as the default model of MEM calculation of the next lower temperature. The central idea of this method is that at high temperature, the spectrum usually has less feature. So at the high temperature MEM, we can use a featureless model, for example a flat model or Gaussian model, or a model from perturbation theory, as the default model. And as the temperature is decreased, the low energy features are provided by the QMC data at low temperature.

E.1.6 Analytic continuation of $G(i\omega_n)$ and $\Sigma(i\omega_n)$

In the MEM of $G(i\omega_n)$, the kernel is

$$K(\omega_n, \omega) = \frac{1}{i\omega_n - \omega} \quad (\text{E.26})$$

and

$$G(i\omega_n) = \int d\omega \frac{A(\omega)}{i\omega_n - \omega} \quad (\text{E.27})$$

But when analytic continuation of self-energy $\Sigma(i\omega_n)$ is needed, in order to fulfill the Hilbert transform

$$f(z) = \int d\omega \frac{f(\omega)}{z - \omega} \quad (\text{E.28})$$

we need to subtract the real constraint term from the self-energy

$$\tilde{\Sigma}(i\omega_n) = \Sigma(i\omega_n) - \Sigma^0(i\omega_n) \quad (\text{E.29})$$

For example for the Hubbard model,

$$\tilde{\Sigma}(i\omega_n) = \Sigma(i\omega_n) - U(n - \frac{1}{2}) \quad (\text{E.30})$$

whose leading order is $O(\frac{U^2 n(1-n)}{i\omega_n})$, just like the Green's function. But the integral of spectrum for such form of self-energy is

$$\int d\omega A(\omega) = U^2 n(1-n) \quad (\text{E.31})$$

Otherwise in order to have a normalized spectrum, we can choose

$$\tilde{\Sigma}(i\omega_n) = \frac{\Sigma(i\omega_n) - U(n - \frac{1}{2})}{U^2 n(1-n)} \quad (\text{E.32})$$

which is order of $O(\frac{1}{i\omega_n})$. The spectra for self-energy is again normalized

$$\int d\omega A(\omega) = 1 \quad (\text{E.33})$$

E.2 Stochastic Analytic Continuation

It has been a long time that people suppose that averaging a set of solutions may give out the correct or approximating spectra. In 1998, Sandvik [96] propose that by averaging the possible spectra according to their Boltzman weight

$$\langle A(\omega) \rangle = \frac{1}{Z} \int dA A(\omega) e^{-\alpha H(A)} \quad (\text{E.34})$$

in which

$$H(A) = \int_0^\beta d\tau \left(\frac{G(\tau) - \int_{-\infty}^\infty d\omega K(\tau, \omega) A(\omega)}{\sigma(\tau)} \right)^2 \quad (\text{E.35})$$

You may noticed that $H(A)$ is exactly the misfit function in MEM. Here every spectra is treated in equal foot and their weight is only determined by their Boltzman weight as a functional of $H(A)$. α in this analytic continuation strategy is interpreted as the inversed

temperature. When $\alpha \rightarrow 0$ at the high temperature limit, $e^{-\alpha H} \rightarrow 1$, the input of Green's function has no effect on the spectra. All possible solutions are simply averaged with the same weight. While at the low temperature limit $\alpha \rightarrow \infty$, only the ground state solution, in another word only the spectra exactly fit to the QMC data have contribution.

By using classic Monte Carlo method, the possible solution is sampled at a series of temperature α^{-1} by treating the possible spectra as external fields. In order to accelerate such sampling, parallel tempering strategy is employed. The configuration of external fields (or the spectra) at different temperature will be swapped after certain number of updates.

The experience is MEM tends to round the sharp features in spectra and prefer smooth features. There is evidence indicates that stochastic analytic continuation (SAC) works better to capture the sharp features of real spectra.

The connection between SAC and MEM is unclear until K. Beach [32] proved that MEM is a special limit of SAC. So it is reasonable to believe that the Bryan's methods should works for SAC. The output of MEM can be used as input for the SAC and the final spectra can be acquired by an average of spectra at different α according to their probability distribution from MEM.

Appendix F

Publication List

1. *Phonons and the coherence scale of models of heavy fermions*, M. Raczkowski, P. Zhang, F. F. Assaad, T. Pruschke, M. Jarrell, Phys. Rev. B **81**, 054444 (2010), arXiv:arXiv:0910.2954.
2. *Periodic Anderson model with electron-phonon correlated conduction band*, Peng Zhang, Peter Reis, Ka-Ming Tam, Mark Jarrell, Juana Moreno, Fakher Assaad, Andy McMah, Phys. Rev. B **87**, 121102 (2013).

"The author has the right to use the article or a portion of the article in a thesis or dissertation without requesting permission from APS, provided the bibliographic citation and the APS copyright credit line are given on the appropriate pages."

Quoted from the website of the American Physical Society (APS).

Vita

Peng Zhang was born in July 1981 at Xingping, Shaanxi, P. R. China. He finished his Bachelor degree of Physics in June 2002 at the Zhejiang University and his Master degree of Physics in June 2006 at the Zhejiang University as well . In the spring of 2009 he transferred from the University of Cincinnati to the Louisiana State University. Currently he is a Ph.D candidate at the Physics department of Louisiana State University.